ATOMIC-SCALE IN SITU TEM INVESTIGATION OF DEFORMATION TWINNING IN HCP CRYSTALS

by

Yang He

B.S., University of Science and Technology Beijing, 2008

M.S., University of Science and Technology Beijing, 2011

Submitted to the Graduate Faculty of

Swanson School of Engineering in partial fulfillment

of the requirements for the degree of

Doctor of Philosophy

University of Pittsburgh

2018

UNIVERSITY OF PITTSBURGH

SWANSON SCHOOL OF ENGINEERING

This dissertation was presented

by

Yang He

It was defended on

March 29th, 2018

and approved by

Guofeng Wang, PhD, Associate Professor, Department of Mechanical Engineering and Materials Science

Tevis Jacobs, PhD, Assistant Professor, Department of Mechanical Engineering and Materials Science

Giannis Mpourmpakis, PhD, Assistant Professor, Department of Chemical & Petroleum Engineering

Dissertation Director: Scott X. Mao, PhD, Professor, Department of Mechanical Engineering and Materials Science

ATOMIC-SCALE IN SITU TEM INVESTIGATION OF DEFORMATION TWINNING IN HCP CRYSTALS

Yang He, PhD

University of Pittsburgh, 2018

Twinning plays critical role in the deformation of hexagonal close-packed (HCP) metals. Developing HCP alloys with improved properties requires a fundamental knowledge on the twinning mechanisms which, however, remain largely theoretical contentions. Here, by using state-of-the-art in situ transmission electron microscopy, the atomic mechanisms of twinning in HCP metals were unprecedentedly revealed.

Classically, the most prevalent {1 0 -1 2} twinning proceeds by shuffle-gliding of twinning dislocations (TDs). However, this mechanism has been challenged by extensive discrepancies in experiments. Here, it was found that the twinning nucleation and growth were primarily mediated by direct transformation of matrix prismatic planes into twin basal planes, which established the same lattice correspondence as an ideal {1 0 -1 2} twin. In detwinning, the twin boundaries retreated from incoherent basal│prismatic and prismatic│basal interfaces to coherent twin boundaries; thereafter, the classical TD mechanism dominated in the detwinning. The findings demonstrate that the twinning formation is not necessarily a shear-dominated process on the twinning plane. Moreover, a new mechanisms of HCP→FCC transformations was discovered, which proceeded by $\{1\ -1\ 0\ 0\}_{hcp}\rightarrow\{1\ 1\ 1\}_{fcc}$ transformation. The FCC phase assisted the {1 0 -1 2} twinning of the HCP matrix as it transformed back to HCP structure through $\{1\ 1\ 1\}_{fcc}\rightarrow(0\ 0\ 0\ 1)_{hcp}$ transformation.

It is generally believed that {1 1 -2 1} twinning is mediated by TDs. Here, direct evidences for the TD mechanism and theoretical twinning elements were unambiguously

revealed. In stark contrast to the general consensus, atomic shuffles happened along 1/6<1 -1 0 0> on alterative basal planes. Classically, {1 1 -2 2} twinning is a contraction twinning mode. Here, a {1 1 -2 2} tension twinning mode was discovered, wherein basal plane was K_2. The finding was further corroborated by the large twinning shear and dominant elementary TDs.

This dissertation resolves long-standing controversies in HCP twinning, reveals prolific new transformation mechanisms pertinent to twinning, and provides crucial information for the twinning-based design and processing of HCP alloys with desired mechanical properties.

TABLE OF CONTENTS

LIST OF TABLES

LIST OF FIGURES

PREFACE

I would like to express my gratitude to those who have helped me during my PhD period. First, I want to sincerely thank my advisor: Prof. Scott X. Mao, for his great support and professional instructions which elevated my work ethic and guided me through a fruitful journey of PhD research. His encouragement and enthusiasm for high standard research will continue to influence me in my future academic life.

Next, I want to sincerely acknowledge my collaborators: senior scientist Dr. Chongmin Wang at Pacific Northwest National Lab, for his great support on TEM and encouragements; Prof. Ting Zhu at Georgia Institute of Technology, for his professional instructions on scientific writing; Prof. Bin Li at University of Nevada, for his pioneer insights in twinning and unselfish contribution to my paper; Prof. Jun Li at Tsinghua University for his pioneer ideas in catalysis and unselfish instructions.

I also want to thank my friends: Dr. Jiangwei Wang, Dr. Li Zhong and Dr. Dingshun She at University of Pittsburgh, Dr. Meng Gu, Dr. Pengfei Yan, Dr. Langli Luo, Dr. Xin Zhang, and Dr. Yingge Du at Pacific Northwest National Lab, and Dr. Feifei Fan at University of Nevada for their unselfish assistance on my experiments, paper revision and everyday life.

Last, from the bottom of my heart, I want to thank my family (especially my grandpa who have passed away) for their unconditional love.

1.0 INTRODUCTION

HCP metals are a very useful class of metallic structural materials. For example, magnesium (Mg) alloys are among the lightest structural metals and can increase the fuel efficiency of spacecraft, aircraft and automobiles by significantly reducing their weights[1,2]. Unfortunately, strength of Mg alloys is generally lower than that of steel; and hence structural parts made of Mg alloys are bulky which limits their application in confined spaces. Additionally, the application of Mg alloys is also limited by their poor formability and brittle nature at low temperatures[3]. Better applications of light weight HCP metals rise high demand for developing alloys with higher strength and ductility. Conventional processing methods (e.g. cold-rolling) suffer from the so-called "strength-ductility trade-off", i.e. the material strength increases at the expense of losing ductility. Novel nanoscale microstructure design strategies have been developed to battle this trade-off, including grain refinement[4], high density twin structure[5,6], dual-phase high entropy alloy design[7], bimodal grain sizing[8], hierarchical nanotwin structure[9,10], increasing tendency of twinning in nanocrystalline metals[11]. These strategies strengthen the materials by introducing interfaces, such as grain boundaries, twin boundaries, and phase boundaries, to block the motion of dislocations. Particularly, the use of twin structures and deformation twinning shows remarkable efficacy, since twin boundary can serve as blockers to dislocations and, in the meantime, as pathways of dislocation motions[12].

Indeed, twinning plays a crucial role in the mechanical behaviors of crystalline materials under extreme loading conditions (e.g. low temperature and high strain rate)[5,10,12-15], especially nanocrystals and nanocrystalline materials[16]; and controlling twinning has been demonstrated effective in achieving exceptional mechanical properties in FCC and HCP metals[5,10,12-14,17]. Particularly, in HCP metals that are widely used as (or promising) structure materials in aerospace, automotive, nuclear, chemical and medical industries, twinning can be profusely activated[18,19] and critically influences the ductility[1], strength, work hardening[20], texture formation[21] and fracture[22], primarily because twinning can carry deformation along <***c***> axis of the HCP crystal wherein dislocation plasticity is limited[1,19,21]. For example, twinning can significantly harden HCP metals by rotating grains from soft direction to hard directions and causing dislocation transmutation during twinning growth[20,23,24]. As such, controlling twinning and evaluating the twinning-dislocation interaction are inevitable in developing HCP metals with superior mechanical performances.

As stated by Clapp[25], "*To become a successful modern witch doctor, the atomic mechanisms that dominated the transformation processes in materials are critical knowledge in predicting and controlling the transformations for optimum microstructures and hence properties.*". Designing and processing metals with desired microstructures and mechanical properties requires a fundamental knowledge on the atomic mechanisms of deformation. This principle has been well-demonstrated by the recent works on dislocation-based alloy design of HCP metals[1,2]. By contrast, twinning-based alloy design and processing have been impeded by the elusive knowledge on the atomic mechanisms of twinning nucleation and growth in HCP crystals, primarily due to lack of direct experimental evidences on the twinning processes in HCP crystals.

Thanks to the development of advanced in situ transmission electron microscopy (TEM), remarkable progresses have been made on the study of atomic deformation mechanisms in face-centered cubic (FCC), body-centered cubic (BCC) and diamond-cubic nanocrystals[26-30]. The utilization of nanosized crystals benefits the studies of transformations in several ways. First, the intrinsic electron-transparency of nanosized crystals enables the TEM study of deformation mechanisms at high (or even atomic) resolution. Second, due to the starvation of "conventional" dislocation sources (e.g. Frank-Reader source) and lack of ability to store dislocations[31,32], nanocrystals show a "smaller is stronger" trend[33-36]; and hence deformation modes, which normally require high activation stresses and rarely present in bulk metals, can become active in nanosized samples[27,28,35-40]. Third, it has been suggested that surface nucleation of twinning may become prevalent in HCP nanocrystals[41,42]. Unfortunately, due to a lack of suitable HCP metal for atomic-resolution operando TEM study and the difficulties in manipulating nanocrystals, application of in situ TEM in investigating the deformation of HCP metals is very limited[43-47] and barely achieves atomic-resolution operando[48] which is crucial for acquiring unambiguous twinning mechanisms in HCP metals.

In this dissertation, by in situ deforming rhenium (Re) nanocrystals inside a state-of-the-art aberration-corrected TEM, the atomistic mechanisms of major twinning modes and phase transformations in hexagonal close-packed (HCP) crystals are directly visualized. The results demonstrate novel mechanisms of twinning nucleation, growth, and phase transformations, providing deep insights on the transformation pathways and the shear-shuffle competition in HCP twinning. The mechanistic findings lay the foundation for twinning-based alloy design and processing of HCP metals with desired microstructure and mechanical performances.

Specifically, the investigation encompassed the {1 0 -1 2} twining, {1 1 -2 1} twinning, {1 1 -2 2} twinning and HCP-FCC phase transformations, focused on the critical unresolved questions in these transformations and, through the atomic-scale operando characterizations, established detailed and definitive mechanistic pictures of these transformations. Impressively, the results revealed twinning phenomenon that departed from the expectation of classical twinning theories, featuring with the dominant role of atomic shuffles in some HCP twinning modes, which held great implication for twinning in other double-lattice and multiple-lattice crystal structures. In addition, the study provided direct evidences on the deformation mechanisms of HCP nanocrystals.

In Chapter 2, the background of twinning theories and mechanisms for HCP crystals were reviewed; based on the literature review, several questions were proposed and hence research objectives were listed.

Chapter 3 introduced the general requirements of a suitable material for in situ TEM study, the material used for this research, and the principles of various TEM imaging modes used in this study. Then, the experimental methods including the sample preparation methods, crystal manipulation methods, experimental setup and procedures were described.

Chapter 4 focused on the most prevalent twinning mode in HCP metals, i.e. the {1 0 -1 2} twinning. Theoretical contentions and controversies on this twinning mode were briefly introduced. Then, the in situ results on atomic mechanisms of twinning nucleation, growth and detwinning were described. Detailed discussions were directed on the consequences of the observed mechanisms. Specifically, the observed mechanisms were used to interpret the “abnormal” behaviors of {1 0 -1 2} twinning in literatures.

Chapter 5 introduced two new mechanisms for HCP→FCC martensitic transformation revealed by in situ TEM. The underlying relation between the transformation mechanisms discovered here and reported in literatures was revealed, which was also used to interpret the observation on {1 0 -1 2} twinning. Thereafter, an effective method for predicting mechanisms of non-diffusional transformation was introduced. Additionally, the observations revealed a multi-functional role of the FCC phase in mediating deformation of HCP metals.

Chapter 6 addressed the mechanisms of another prevalent twinning mode in HCP metals, i.e. {1 1 -2 1} twinning. The atomic-scale observations revealed twinning elements that were consistent with the prediction of classical twinning theories. Additionally, the results showed direct evidences on the dominant twinning dislocations and atomic shuffles in the twinning process, clarifying long-standing suspicions in the {1 1 -2 1} twinning.

Chapter 7 focused on the {1 1 -2 2} twinning which was known as a "contraction" twinning mode in HCP metals. The debate on the conjugate twinning plane and twinning shear were introduced, together with the underlying competition of between shear and shuffle in choosing the twinning elements. Here, by tension along the <***c***> axis of a Re nanocrystal, the {1 1 -2 2} twinning was unexpectedly (but reasonably) formed wherein the conjugate twinning plane was the basal plane. This finding was further supported by the observations on the exceptionally large twinning shear and dominant elementary twinning dislocations. Additionally, the interactions of {1 1 -2 2} twinning with basal <*a*> dislocations and {1 1 -2 1} twinning were described. Due to its tension twinning nature, the {1 1 -2 2} twinning was found to cooperate with {1 1 -2 1} twinning, forming a unique three-fold twinning.

Major conclusions were summarized in Chapter 8. The outlook in Chapter 9 described potential guidance of the findings on the design and processing of HCP metals, and future

directions of in situ TEM technology for studying mechanical behaviors of materials. The research should be of general interest to people working on twinning theories, mechanisms of material transformations, nanomechanics, as well as HCP alloy design and processing.

2.0 BACKGROUND

2.1 CLASSICAL TWINNING THEORIES AND TWINNING IN CUBIC STRUCTURES

In the classical description of deformation twinning, twinning is a shear-driven reorientation of the parent crystal[18,19,49] and the resultant structure is a reflection of the parent crystal in the twinning plane (K_1) or a 180^o rotation of the parent crystal about the K_1 normal[18]. Specifically, twinning is defined by four crystallographic features (named as twinning elements)— twinning plane (K_1), twinning direction (η_1), conjugate twinning plane (K_2) and conjugate twinning direction (η_2). Classically, twinning is achieved by a homogeneous simple shear[19] on K_1 and along η_1; during twinning process, K_1 and K_2 are "invariant" and atoms move in a coordinated manner[50-52]. Based on a "minimum twinning shear" assumption, the classical twinning theories were able to predict feasible twinning modes for different crystal structures which has been validated extensively in a broad class of crystal structures[52,53].

It is generally believed that twinning formation is mediated by the movement of twinning dislocations on the coherent twin boundaries (or twinning planes)[50-52,54], which is well-proved by in situ observations on the twinning processes in FCC and BCC crystals. Figure 2.1a-c show the formation process of a typical {1 1 1} twinning in FCC Cu crystal; as shown in the sequential snapshots, the twinning band thickens by successive emission and gliding of 1/6<1 1 2>

twinning dislocations (see Figure 2.1d) from the grain boundary. Figure 2.1e-g demonstrate a similar process of {1 1 2} twinning formation in BCC W nanocrystal. These observations perfectly verified the classical descriptions of twinning which, however, have seen lots of challenges in HCP metals.

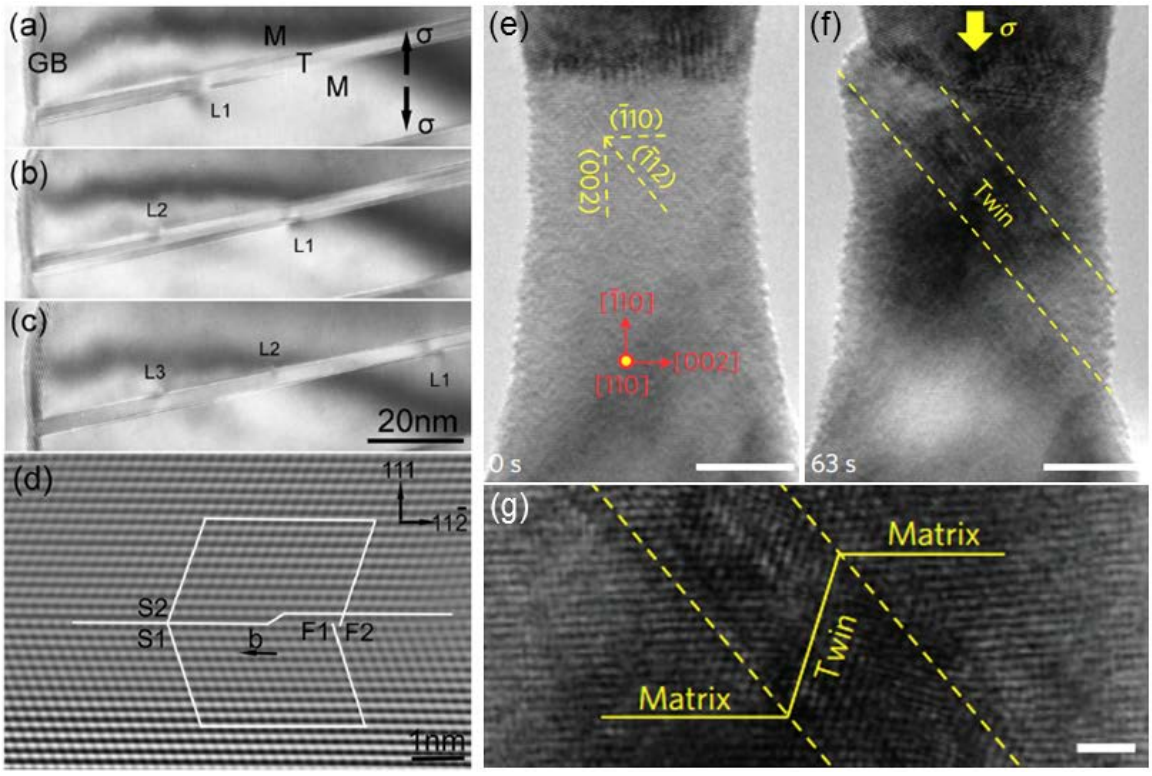

Figure 2.1 In situ TEM observation of twinning formation in FCC Cu (a-d)[55] and BCC W (e-g) crystals[26]. (a-c) Twinning dislocations were emitted from the grain boundary and glided on the coherent twin boundary. (d) High resolution TEM image of the twinning dislocation, i.e. a Shockley partial dislocation. White lines are the Frank circuit. (e-f) Twinning formation in a W crystal under [-1 1 0]-oriented compression. (g) High resolution TEM image of the twin band in (f); yellow dash lines mark the coherent twin boundary on (-1 1 2) planes. Scale bars in (e-f), 5nm; scale bar in (g) 1 nm.

2.2 TWINNING MODES IN HCP CRYSTALS

A total of seven twinning modes within the predictions of classical twinning theories have been discovered experimentally in HCP metals (see Figure 2.2). Depending on the strains generated along the <***c***> axis, twinning modes in HCP crystals are divided into two categories: contraction twins and tension twins[56]. In Ti or Zr alloys, {1 0 -1 2}, {1 1 -2 1} twinning are tension twins and {1 1 -2 2} twinning is contraction twins; and these are the three major twinning modes in room temperature deformation of Ti alloys[57]. {1 0 -1 2} twinning is the most prevalent twinning mode and can be found in all HCP metals[52,58]. Compared with twinning in cubic structures, a significant difference in HCP twinning (or twinning in double-lattice structures) is that homogeneous twinning shear alone normally cannot carry all atoms in the parent lattice to the correct twin positions[19]. As a result, additional atomic movements, called shuffles[18,19], are necessary to accomplish the twinning process. In classical twinning theories, feasible twinning modes in HCP crystals are also believed to have small twinning shear[18,19,49,51]. In dealing with atomic shuffles, the classical twinning theories further assume that feasible twinning modes should have “simple” atomic shuffles.

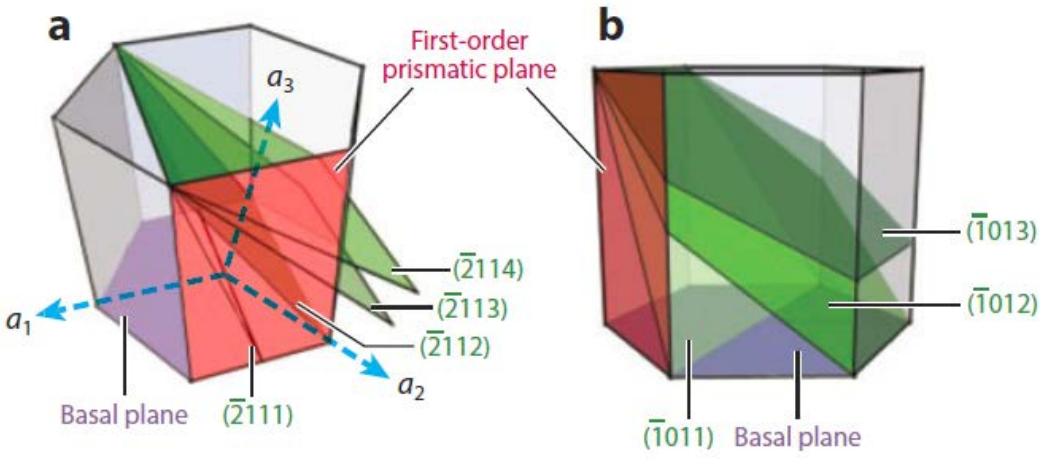

Figure 2.2 Schematic illustrations of the seven twinning planes and slip planes for <***a***> dislocations in the HCP unit-cell.[52]

Nonetheless, smallest twinning shear and simplest atomic shuffles normally cannot be achieved simultaneously in the same choices of twinning elements. As a result, a competition exists between shear and shuffle in choosing the twinning elements. For example, classical twinning theories based on above assumptions predict that the K_2 plane for the {1 1 -2 2}<1 1 -2 -3> twinning should be {1 1 -2 -4} plane[19,59], where twinning shear is relatively small (***b*****$_3$** in Figure 2.3) but required shuffles are large and complex (see Figure 2.4a-b[60]). By contrast, if the K_2 plane is {1 1 -2 -6} plane, required atomic shuffles are larger but the twinning shear becomes smaller (***b*****$_4$** in Figure 2.3); if the K_2 plane is {1 1 -2 -2} plane, required atomic shuffles are simpler but the twinning shear becomes larger (***b*****$_2$** in Figure 2.3); if the K_2 plane is (0 0 0 1) plane, atomic shuffles are not required[59,61] but the twinning shear becomes extremely large (***b*****$_1$** in Figure 2.3, ~1.2 for Mg)[62]. Moreover, recent atomistic simulations proposed that, when the K_2 plane for {1 1 -2 2} twinning was (0 0 0 1) plane, the twinning shear could be reduced by half if atoms shuffle along the twinning shear direction (see Figure 2.4c)[60]. Computational simulations have been carried out extensively to explore the active K_2 plane in {1 1 -2 2} twinning and

revealed different results[60-65]. Due to a lack of strong experimental evidences, the actual K_2 plane and corresponding twinning shear remain in debate[59,61,65-67]. Considering previous experimental investigations[68,69] and the fact that active K_2 plane is also critically influenced by the loading direction[59], the key question is whether an alternative {1 1 -2 2} twinning mode exists in tension along <***c***> axis and what is the associated twinning shear $\boldsymbol{b}_1$ or $\boldsymbol{b}_4$ (see Figure 2.3).

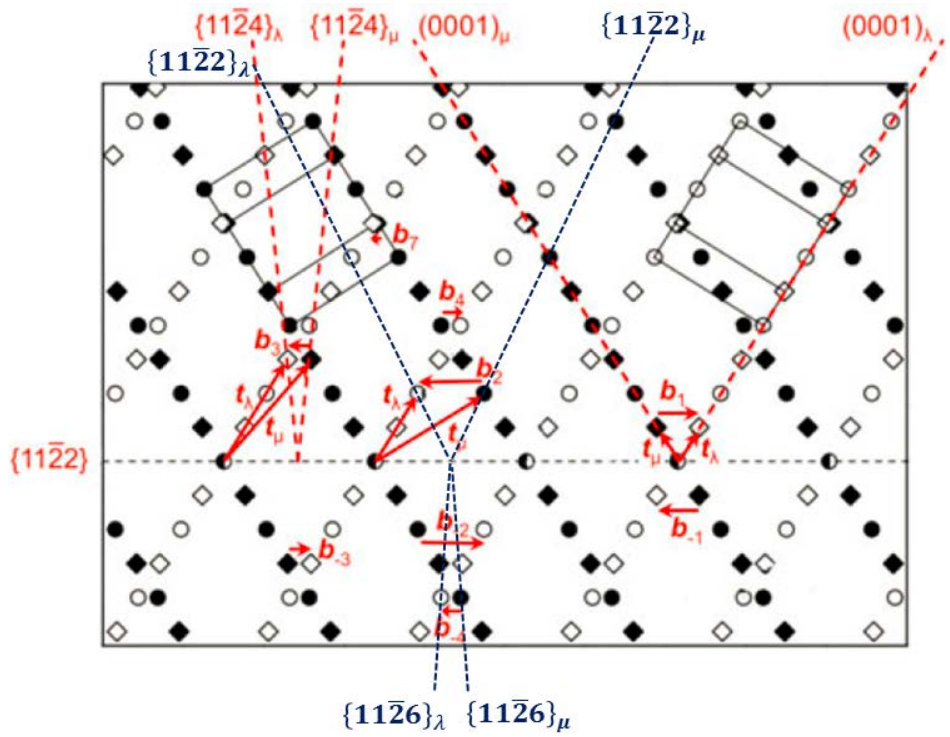

Figure 2.3 Dichromatic pattern for {1 1 -2 2} twinning in HCP viewing along <1 -1 0 0> direction.[59] Black balls and squares indicate atoms in the matrix (μ); white balls and squares indicate atoms in the twin (λ). $\boldsymbol{b}_1$~ $\boldsymbol{b}_7$ and $\boldsymbol{b}_{-1}$~ $\boldsymbol{b}_{-4}$ indicate the possible twinning shears for the {1 1 -2 2} twinning mode. The conjugate twinning plans for $\boldsymbol{b}_1$~$\boldsymbol{b}_4$ are (0 0 0 1), {1 1 -2 2}, {1 1 -2 4}, and {1 1 -2 6}, respectively (see dash lines). Vector $\boldsymbol{t}_\lambda$ and $\boldsymbol{t}_\mu$ are used to define the Burgers vector of a twinning disconnection[50].

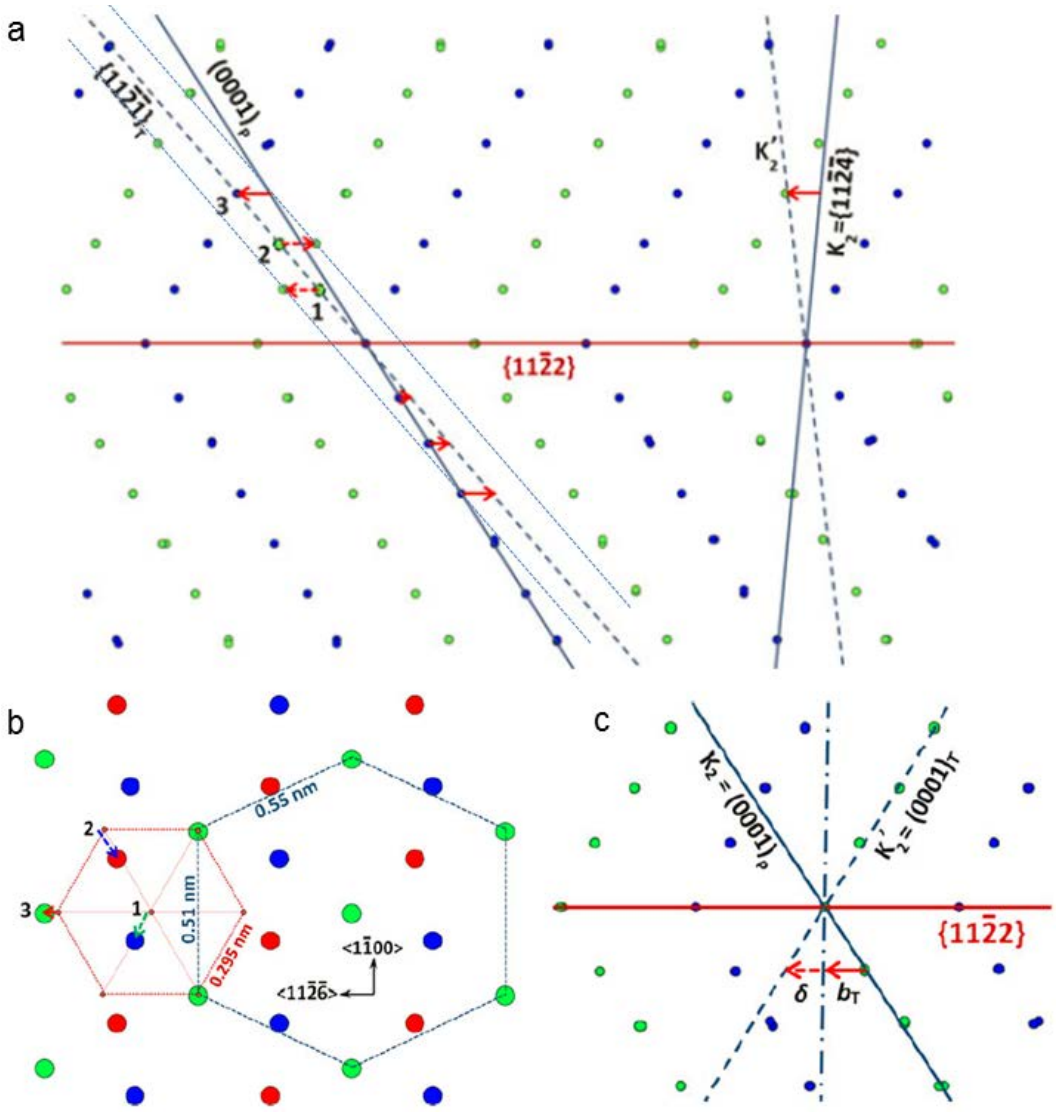

Figure 2.4 Topological analysis of the shear and shuffles required in {1 1 -2 2} twinning process[60]. The K_2 plane is {1 1 -2 -4} in (a-b) and (0 0 0 1) in (c). Red arrows in (a-b) indicate the homogeneous shear vector. Dash arrows indicate the complex atomic shuffles along the shear direction (see red dash arrows in (a)) or within the parent basal plane (see blue and cyan arrows in (b)). Red solid and dash arrows in (c) indicate the shear and shuffle components, respectively. Note that the dash arrows can also be accomplished by twinning shear, i.e. the twinning shear can complete the twinning process and no atomic shuffles are required[62].

When the motif of the crystal structure is complex and spacing of the twinning planes is small, large and complex atomic shuffles (e.g. those in Figure 2.4a) may require the atoms pass by each other at close distances which are energetically unfavorable. In such cases, the simple atomic shuffles may be more important than small twinning shear; in other words, in order to avoid energetically-unfavorable complex-shuffles, the twinning shear may have to be unexpectedly large. To achieve a more precise solution, Crocker[18] pointed out that, "*A purely geometrical analysis of this kind cannot establish uniquely the mode of twinning, which must be controlled by the free energy changes occurring. The discussion of these, of course, requires consideration of the binding forces between the various atoms involved.*" Thereby, accurate energetic calculations or explicit experimental evidences are needed to validate the predictions of classical twinning theories and reveal the exact twinning elements for each twinning mode in HCP metals.

2.3 TWINNING MECHANISMS IN HCP CRYSTALS

2.3.1 Twinning growth mechanisms in HCP crystals

To date, it is generally believed that twinning in HCP metals is mediated by shuffle-gliding of twinning dislocations on the twinning plane[50,70]. To minimize the twinning shear and atomic shuffles and ensure that the twin boundary structures were identical on the two sides of the twinning dislocation, twinning dislocation has to span several layers of the twinning plane, i.e. have a step feature. Therefore, zonal dislocation concept[71], previously used for describing dislocations in complex crystal structures, was applied to describe twinning dislocations in HCP

crystals[72,73]. In recent years, the concept of disconnection featuring with a Burgers vector (***b***) and a step height (h)[50,74], previously used for describing interfacial defect in phase transformations, is used for describing twinning dislocations in HCP metals. To avoid confusion, in this dissertation, we will use the term "twinning dislocations" and the nomenclature (b_n, h_n), where n is the number of layers (i.e. the "zonal" feature) the twinning dislocation embodies. Assuming the lattice periodicity on along η_2 direction is q, classical twinning theories predict that, in order to minimize the burgers vector and shuffles carried by the twinning dislocation and guarantee that the twin boundaries separated by the twinning dislocation have the same structure, the twinning dislocation should have a step height of $q/2$ (if q is even) or q (if q is odd)[19]. Though the exact characteristics of dominant twinning dislocations for a specific twinning mode may be under debate, the twinning dislocation mechanism is supported by extensive ex situ observations of the interfacial defects on coherent twin boundaries[75-78] (see Figure 2.5).

Based on atomistic simulations, sources of the twinning dislocations include dissociation of matrix dislocations[41,79], reaction of matrix dislocation with coherent twin boundary (or the "Serra-Bacon source")[80-82], nucleation of twinning dislocation loops on coherent twin boundary[60,83], nucleation of twinning dislocations from surface[46], and interfacial defects on incoherent twin boundaries[84,85]. However, due to the lack of strong experimental evidences, most of these mechanisms remain theoretical contentions.

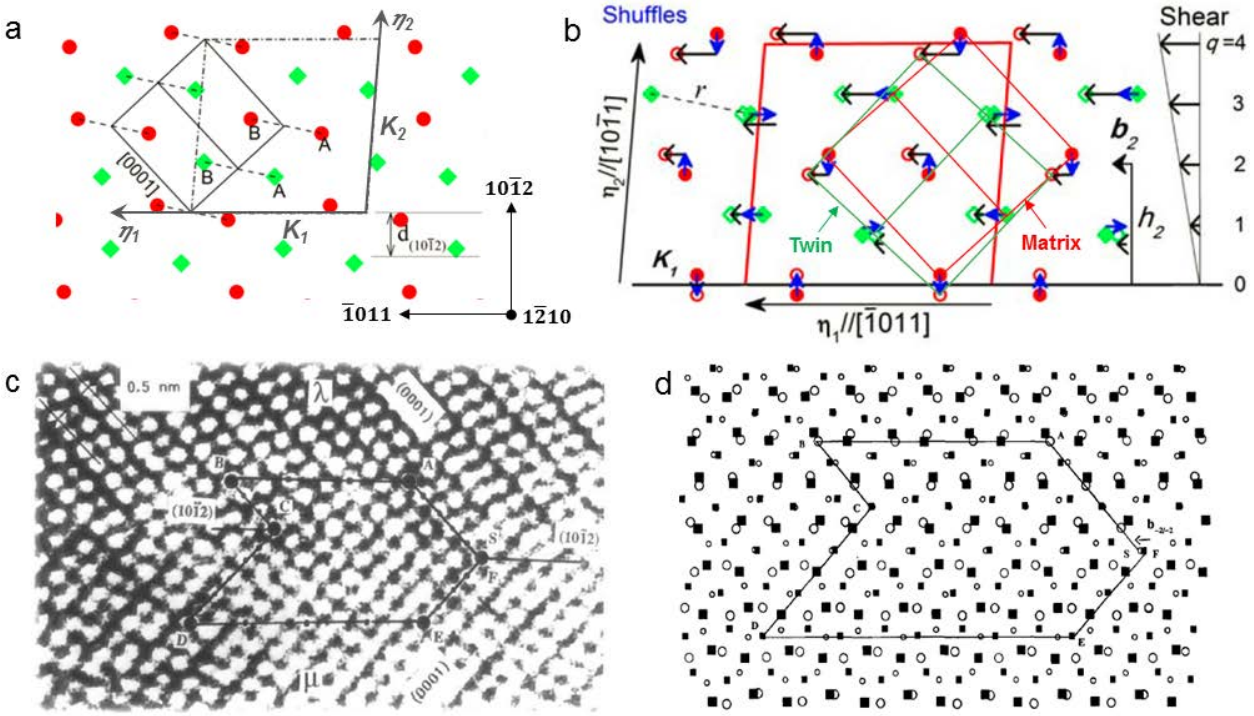

Figure 2.5 Classical description of {1 0 -1 2} twinning and corresponding twinning dislocation. (a) HCP crystal structure viewing along the [1 -2 1 0] direction[51]. Twinning elements for the {1 0 -1 2} twinning mode were indicated. (b) Bilby & Crocker description of the shear (black arrows) and atomic shuffles (blue arrows) in the {1 0 -1 2} twinning process[18,51], viewing on the shear plane. Note that the lattice periodicity along the η_2 direction, q, is 4, implying that the twinning dislocation for {1 0 -1 2} twinning should be (b_2, h_2). (c) HRTEM image of a (b_2, h_2) twinning dislocation on the {1 0 -1 2} twin boundary in Zn[77]. (d) Dichromatic complex of the twinning dislocation; open and solid markers indicate the atoms in the twin and matrix, respectively[77].

Though supported by extensive ex situ observations on the interfacial defects[77,78,86] (e.g. Figure 2.5), computational simulations[50,70,74,77,78], some in situ observations[46] (see Figure 2.6) and macroscopic indirect evidences[87], the twinning dislocation mechanism is challenged extensively by more and more abnormal experimental findings on the most prevalent {1 0 -1 2}<1 0 -1 -1> twinning mode[88-92]. For example, characterizations on deformed HCP metals show

that a considerable part of the prevalent twin boundaries of {1 0 -1 2} twinning deviates from the twinning plane and resides on the B│P-type interfaces (see Figure 2.7 and Figure 2.8)[89,93]. Though, based on twinning dislocation mechanism, the B│P-type interfaces were interpreted as the step risers of twinning dislocations with exceptionally large step height[86]. It is argued to be unfeasible, since an extremely high shear stress would be required to densely pile-up large number of ($\boldsymbol{b}_2$, h_2) twinning dislocations in order to form such a large twinning dislocation; should the twinning process be dominated by twinning dislocations on the twinning plane, the twin boundaries would primarily conform to the coherent twinning plane rather than the incoherent B│P-type interfaces (see Figure 2.8a and Figure 2.9a)[43,89]. In addition, orientation relation between the matrix and {1 0 -1 2} twin widely departs from that of ideal mirror symmetry (see Figure 2.9b)[89]. EBSD on deformed bulk HCP metals shows that twinning nucleation and growth are significantly influenced by non-Schmid stresses, showing a breakdown of the Schmid's law[90-92,94,95]. {1 0 -1 2} twinning has weak interactions with precipitates, matrix dislocations and concomitant slip in front of the twin tip[22,58].

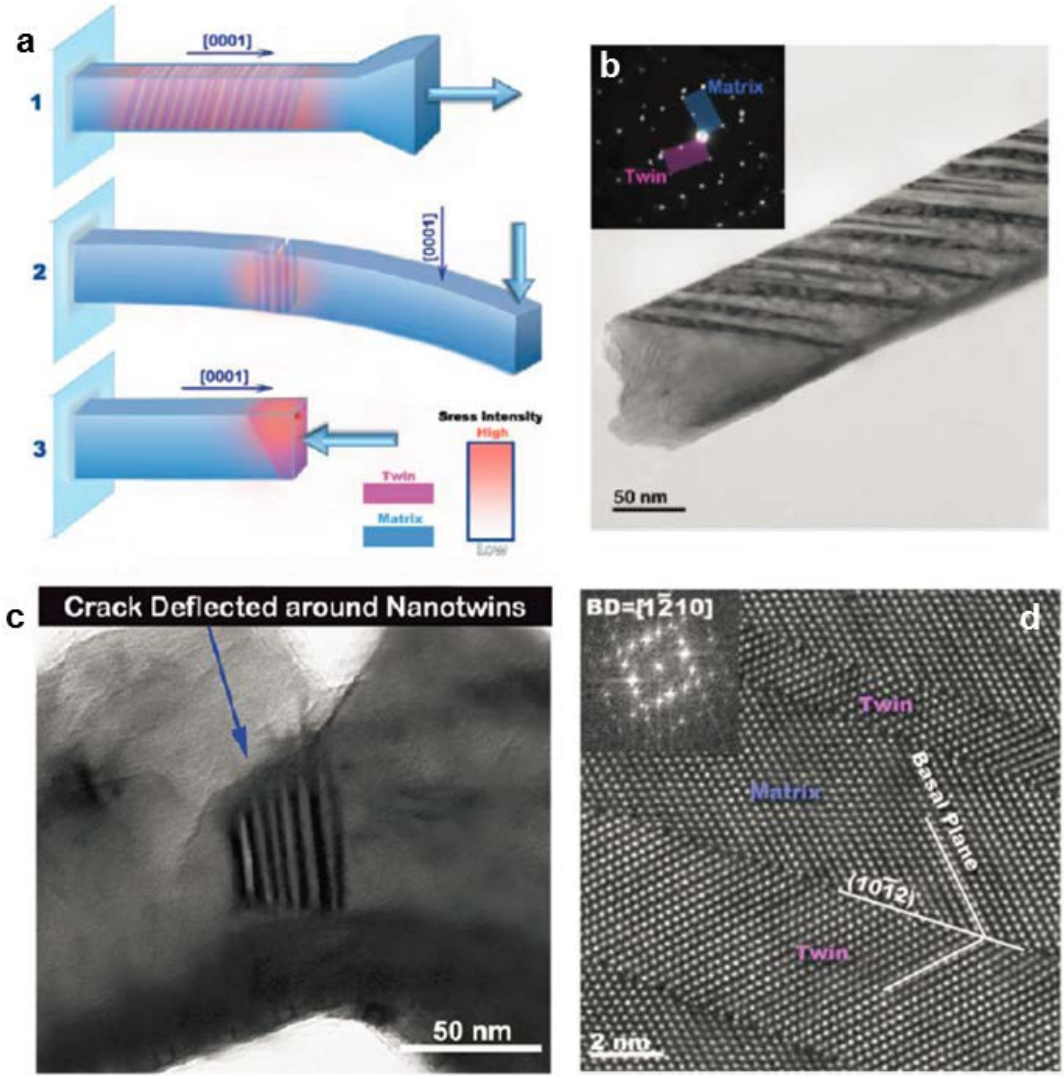

Figure 2.6 In situ TEM observation of the {1 0 -1 2} twinning process in Mg nanopillars[46]. (a) Schematic images showing the formation of {1 0 -1 2} twinning in Mg nanopillars under various loading conditions. (b) TEM image of the residual twin bands in a fractured Mg nanopillar. (c) TEM image of the residual twin bands in front of a crack tip formed during bending deformation. (d) HRTEM image of the twin bands shown in (b) which were obviously bonded by coherent twin boundaries. The low magnification morphology of the {1 0 -1 2} twins (after unloading) implies that the twinning was mediated by twinning dislocations on the coherent twin boundaries.

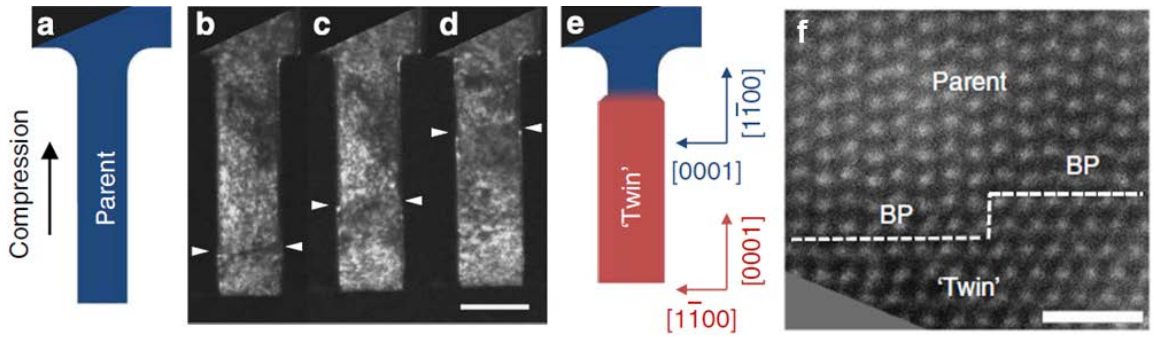

Figure 2.7 In situ evidences for the lack of shear features on the sample surface during twinning. (a, e) Schematic images to illustrate the deformation of a Mg nanopillar under [1 -1 0 0]-oriented compression[43]. (b-d) Sequential dark-field in situ TEM snapshots showing the growth of a {1 0 -1 2} twinning[43]. (f) Atomic resolution STEM image of the twin boundary on the B | P interface[43]. Scale bar in (d), 400 nm; scale bar in (f), 1 nm.

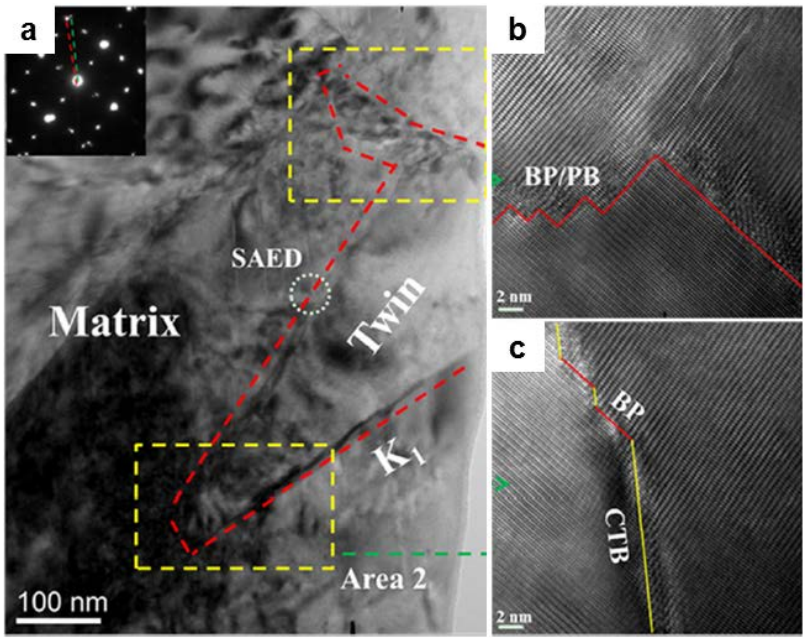

Figure 2.8 {1 0 -1 2} twinning in a deformed AZ31 Mg alloy[96]. (a) The irregular-shaped twin boundary (indicated by red dash lines). Inset is the select area electron diffraction pattern of the circled region, which proves that the twin belongs to the {1 0 -1 2} twinning mode. (b, c) HRTEM images of the twin boundaries which are dominated by B | P and P | B interfaces (indicated by red lines).

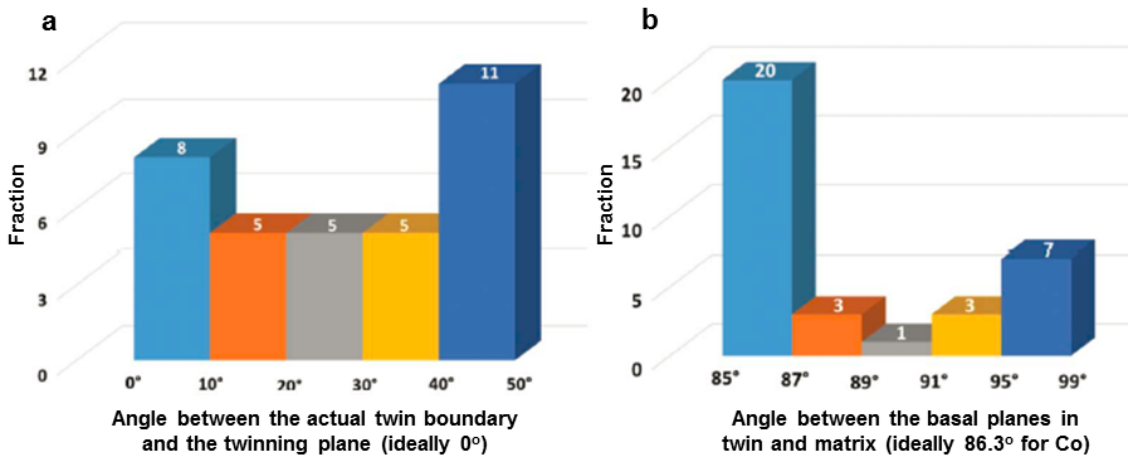

Figure 2.9 Statistical analysis of the orientation of the twin boundary (a) and lattice rotation as a result of the {1 0 -1 2} twinning (b). 79% of the twin boundaries deviate from the twinning plane; and 56% of the lattice rotation deviate from the value of an ideal {1 0 -1 2} twinning.[89]

Considering the important role of the {1 0 -1 2} twinning in deformation of HCP metals[97,98], above abnormal behaviors of the {1 0 -1 2} twinning call into questions the exact mechanism of the twinning nucleation and propagation in HCP metals. Theoretical endeavors based on topological analysis and computational simulations have been made, leading to the interfacial defect mechanism (see Figure 2.10)[50,58,84,99] and pure-shuffle mechanism (see Figure 2.11)[43,100,101]. Unfortunately, neither of these mechanisms can address all abnormal behaviors of the {1 0 -1 2} twinning; furthermore, the proposed twinning mechanisms are debatable as they lack solid experimental evidences and cannot reconcile with each other[101,102].

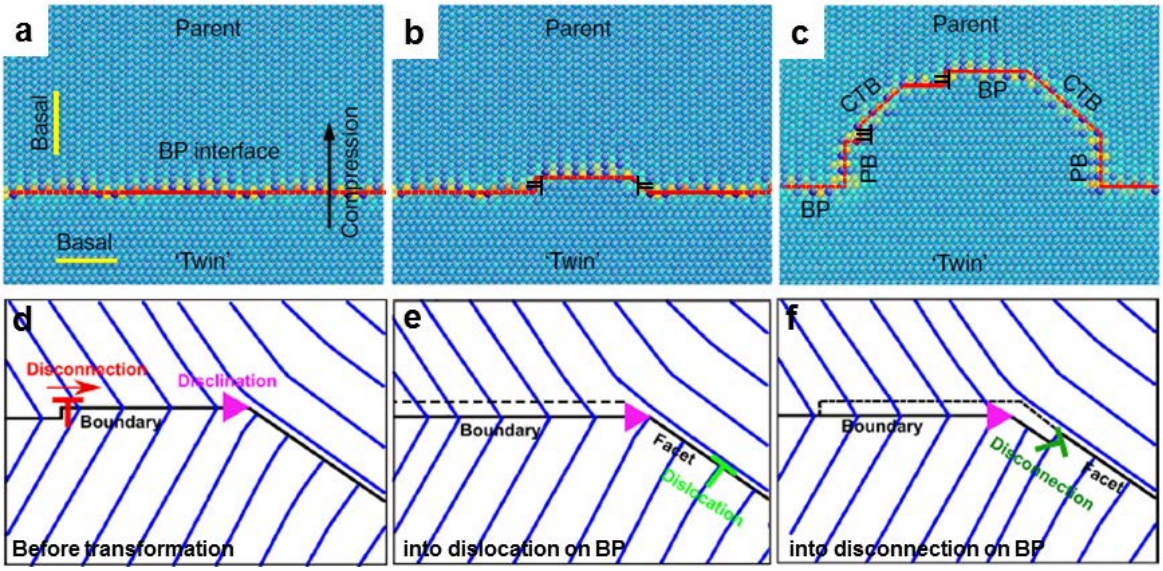

Figure 2.10 Interfacial defects on B|P-type interfaces and their role in the formation and propagation of serrated coherent twin boundaries. (a-c) MD simulation of interfacial defect dipoles formation (indicated by black markers in (b-c)) on the B|P interface under compression; the migration and accumulation of these interfacial defects formed B|P-type interfaces and coherent twin boundaries (CTB), and resulted in the propagation of the twin boundary[43]. (d-f) Schematic illustration of the twinning dislocation transformation onto the B|P interface; in scenario I (e), the twinning dislocation transformed into a dislocation on the B|P interface; in scenario II (f), the twinning dislocation transformed into a disconnection on the B|P interface. In both cases, the disclination moved but in different direction[103]. Refer to the reference for detailed topological and mathematical analysis[58,103].

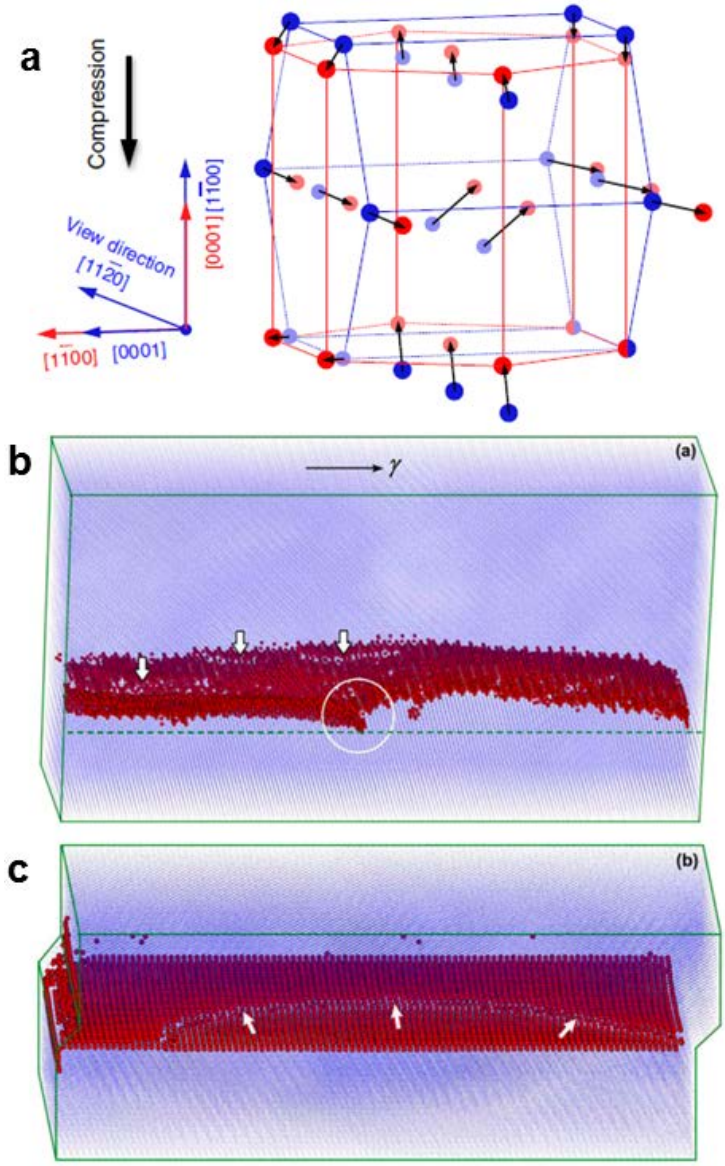

Figure 2.11 Schematic description (a) and MD simulation (b) of the shuffle-dominated {1 0 -1 2} twinning. (a) Schematic image showing the basal/prismatic transformation process (i.e. {1 0 -1 2} twinning[101]) mediated by atomic shuffles (indicated by black arrows)[43]. The parent and twin unit-cells were colored blue and red, respectively. (b) 3D view of the {1 0 -1 2} twin boundary migration from MD simulation. The atoms on the TB were highlighted in dark red. The dash line indicates the original position of the coherent twin boundary. Obviously the twin boundary was very rough during propagation with no well-defined twinning dislocation, in contrast to the twinning dislocation (indicated by white arrows in (c)) mediated {1 1 -2 2} twinning[104].

It should be noted that the pure-shuffle mechanism revealed by the molecular dynamics simulations can lead to a paradigm-shifting view on the {1 0 -1 2} twinning— twinning formation only requires the establishment of a specific lattice correspondence. As pointed out by Christian[105], "*A deformation which is physically significant implies a one to one correspondence between vectors in the two lattices. Each vector in one lattice may be associated unambiguously with a "corresponding" vector of the other lattice into which it is converted by the transformation.*" In the pure-shuffle mechanism[43,100,101,106], the parent prismatic planes directly transform into basal planes in the twin which follows the lattice correspondence of an ideal {1 0 -1 2} twin[107]. Though the resultant structure is different from an ideal {1 0 -1 2} twin in terms of generated grain rotation[108], the pure-shuffle mechanism establishes exactly the same lattice correspondence as that of an ideal {1 0 -1 2} twin[107]. As a result, the twinning formation can be "liberated" from the confinement of the twinning plane and hence violate the invariant plane strain condition[109]. Though the pure-shuffle mechanism stands out in explicating most abnormalities of the {1 0 -1 2} twinning, it cannot explain the presence of coherent twin boundaries and the dominant misorientations between the matrix and twin (refer to the diffraction patterns in references[86,96,110]).

It should be noted that the twinning dislocation mechanism for other major twinning modes, e.g. {1 1 -2 1}, {1 0 -1 1} and {1 1 -2 2} twinning, is generally accepted[51,52,63]. Yet, detailed and sometimes crucial questions exist in these twinning modes. For example, classical twinning theories predicts that the twinning dislocation in {1 1 -2 1} twinning should have a step height of a single {1 1 -2 1} plane. However, due to the structure degeneracy, it is suggested that each elementary twinning dislocation could be dissociated into two mobile ($\boldsymbol{b}_{1/2}$, $h_{1/2}$)

dislocations[51,63]. Similarly, it remains a theoretical contention as for how atomic shuffles proceed in the {1 1 -2 1} twinning[111].

2.3.2 Twinning nucleation mechanisms in HCP crystals

Proposed mechanisms of twinning nucleation in HCP crystals include the pole mechanism[41,112], dissociation of <***c***> and <***c***+***a***> dislocations[79,113], nucleation of twinning dislocations from free surface[46], nucleation of large zonal twinning dislocations from grain boundary[114], shuffle-dominated nucleation from grain boundary[100] and from free surface[115] (named as "homogeneous nucleation" by the authors). These mechanisms are more or less supported by indirect and obscure evidences which are far from convincing; and direct experimental validation are currently lacking. Due to the fast transformation speed, small volume involved and a strong tendency of detwinning[116-118], twin nucleation process has never been experimentally captured.

Given that the accuracy of the topological analysis and computational simulations relies critically on a correct description of interatomic potentials[18,100-102,104,114], and that ex situ experimental characterization using deformed samples could be misleading due to the tendency for detwinning upon unloading (especially in twin embryos[114,117]), atomically-resolved direct experimental investigation, if available, are highly desirable to elucidate the actual atomic shuffles and shear during twinning nucleation and growth, and hence obtaining a fundamental understanding on twinning mechanisms in HCP crystals[47,52,92]. Unfortunately, no atomic-scale direct investigation on the twinning process in HCP metals has been realized, likely due to a lack of advanced in situ techniques and a suitable model material for in situ TEM investigation.

2.4 MOTIVATION AND RESEARCH OBJECTIVES

The research is motivated by three factors. First, twinning plays important role in the deformation of HCP metals; and hence the design and processing of HCP metals with desired microstructures and properties inevitably require the knowledge of atomic mechanisms of major twinning modes. Second, in situ atomic-scale investigations of the twinning processes in HCP crystals are indispensable and highly desired to explicitly address the key questions in the field. As shown in above sections, related researches rely mostly on topological analysis and atomistic simulations which are limited by the imperfect description of interatomic potentials and require validation from experiments; and the atomic twinning mechanism is inaccessible to macroscopic and ex situ microscopic observations. Third, the study of twinning in HCP metals will shed light on the twinning behaviors in other important structural materials with double-lattice or multiple-lattice crystal structures (e.g. calcite and hydroxylapatite) which also proceed by shear and shuffles. In lieu of the significances and critical questions revealed in above background review, in this investigation, major twinning modes and phase transformation pertinent to twinning will be investigated by in situ deforming HCP rhenium crystals inside an atomic-resolution TEM. The major research objectives are as follows:

1. What is the exact mechanism for {1 0 -1 2} twinning nucleation?? Based on the non-Schmid effect and computational simulations, the twinning nucleation is more likely a “shuffle-dominated” process. Since our samples are mostly defect-free nanocrystals, the nucleation mechanism should be no other than the nucleation of twinning dislocations or shuffle-dominated process on surface or grain boundaries. Incidentally, the twinning dislocation mechanism and shuffle-dominated P→B transformation mechanism can be captured and explicitly differentiated by viewing the twinning along <1 1 -2 0> direction.

2. Is the {1 0 -1 2} twinning growth in HCP metals mediated by twinning dislocations? If yes, what is the dominant twinning dislocation? If not, what defects mediate the {1 0 -1 2} twinning growth? How to explain the "abnormal" behaviors of the {1 0 -1 2} twinning? Based on the reported experimental results so far, it seems that both "shuffle-dominated" and "shear-dominated" mechanisms should work in mediating the twinning. Yet, it is elusive as for how the B|P-type interfaces transform to CTB and how the two mechanisms cooperate. As shown in task 1, these questions should be resolvable by characterizing the twinning process along <1 1 -2 0> viewing direction.

3. Are the twinning elements predicted by the classical twinning theories correct for {1 1 -2 1} twinning? What is the dominant twinning dislocation for this twinning mode? Are there atomic shuffles involved in this twinning process? How do the atomic shuffles proceed? Based on computational simulations and ex situ experimental measurements, it is generally accepted that the {1 1 -2 1} twinning mode follows the classical prediction, except that the twinning dislocations are not ($\boldsymbol{b}_1$, h_1) but ($\boldsymbol{b}_{1/2}$, $h_{1/2}$) due to the structural degeneracy of the twin boundaries and it requires atomic shuffles though the manner of atomic shuffles is not clear. The investigation will be directed to verify the twinning elements, mechanism and dominant twinning dislocations by viewing the twinning process along the <1 -1 0 0> direction (i.e. looking down the plane of shear). Since the shuffles are likely perpendicular to the plane of shear, it will be characterized along a viewing direction that is not perpendicular to the <1 -1 0 0> direction but parallel to the {1 1 -2 1} twinning plane. Atomic resolution TEM image of a propagating twin boundary will be acquired and analyzed with the assistance of image simulations to reveal the angstrom-level shuffles.

4. Will the {1 1 -2 2} twinning happen in tension along <$\boldsymbol{c}$> axis? What is the K_2 plane for the {1 1 -2 2} tension twinning? What are the twinning shear and dominant twinning dislocation for this twinning mode? Why does the twin proceed in such a way? As shown in Figure 2.3 and literatures, the formation of {1 1 -2 2} tension twinning is theoretically possible. The absence of experimental evidence may be attributed to the exceptionally large twinning shear (when K_2 is basal, see $\boldsymbol{b}_2$ in Figure 2.3) or the complex atomic shuffles (when K_2 is {1 1 -2 -6}, see $\boldsymbol{b}\text{-}_4$ in Figure 2.3). In nanosized samples, surface provides easy strain accommodation and hence the large twinning shear may be tolerable. As such, it is likely to observe a {1 1 -2 2} tension twinning mode in HCP nanocrystals.

5. The implications of pure-shuffle mechanism of twinning should be able to extend to other non-diffusional transformations. In doing so, are there new mechanisms of HCP→FCC transformation? Furthermore, what is the role of HCP→FCC phase transformation in the deformation of HCP metals?

Experimental observations on the twinning and phase transformation processes will provide direct evidences on atomic mechanisms and hence resolve the critical controversies and confusions in twinning of HCP metals.

3.0 MATERIALS AND METHODS

To achieve above research objectives, we need a HCP metal that is suitable for in situ TEM study, a high or atomic resolution imaging capability, an experimental setup and crystal manipulation techniques for controlled deformation of the sample crystals inside TEM.

3.1 MATERIALS

Material suitable for atomic-resolution operando[48] TEM investigations has to satisfy following criterions. First, it has to be resistant to electron beam irradiation in TEM, or rather, have no "beam effects" (especially those that can potentially affect the mechanical behaviors). For metallic materials, the major "beam effects" include "atom displacement" which is known to create vacancies and interstitials, "sputter" which is known to remove atoms from the bottom surface of the sample, and "heating" which is known to increase temperature and possibly induce phase changes[119]. Second, it does not easily oxidize in air, since the oxidation layer can significantly alter the mechanical behavior of the sample by changing the strain field, introducing extrinsic defects and modifying the surface condition for dislocation or twinning nucleation[120]. It should be noted that focus ion beam (FIB) is a widely-used convenient method for making TEM samples with crystal orientation control. The damaging layer of a FIBed sample may potentially affect the deformation[121,122]. Third, the material should be able to deform by all important modes,

e.g. {1 0 -1 2}, {1 1 -2 1}, and {1 1 -2 2} twinning modes. With these criterions in mind, high strength refractory HCP metal of pure rhenium (Re) is satisfactory for this research.

Re is not only a model system for the fundamental studies of HCP metals[123-126], but also crucial structural materials for high temperature applications[127]. Re metal has the highest strength at >2000^{o}C[128], and is widely used as alloying elements to improve creep resistance of alloys in jet-engines[127]. Moreover, it has a typical HCP structure that is stable at room temperature as well as elevated temperatures, highly resistant to oxidation in air and 300 *KeV* electron beam irradiation in TEM[119,129]. Additionally, Re has a c/a ratio (hereinafter referred to as γ) of 1.615 which is very close to that of magnesium (1.624), titanium (1.588) and zirconium (1.593)[56]; and can deform by all important twinning modes in these alloys[123,130], hence the twinning mechanisms can be reasonably extended to Mg, Ti and Zr alloys. These qualities make Re a suitable material for in situ TEM investigation.

In this research, commercial Re metal (99.98% purity, 0.25mm thick plate) is acquired from *SIGMA-ALDRICH* (Missouri, USA). The Re plate is cut into small rods (dimension: 0.25 x 0.25 x 5mm) by using a diamond saw. Then, these rods are mechanically polished to reduce surface roughness and remove surface oxides, followed by rinsing in ethanol alcohol to remove organic contamination on surface. Right before the experiments, the Re rod is plasma cleaned.

Table 3.1 Trace metal analysis of the rhenium sample (Lot MKBQ7216V)

Element	Concentration, ppm	Element	Concentration, ppm
Aluminum	0.6	Iron	35.5
Boron	0.3	Magnesium	3.6
Barium	<0.1	Manganese	5.0
Calcium	1.1	Lead	29.1
Cobalt	2.6	Tin	6.8
Chromium	0.7	**Total**	85.3

3.2 MICROSCOPY METHODS

3.2.1 Introduction to in situ TEM

TEM is widely used in modern materials researches and industry. The unique function of a TEM is the combined direct detection of atomic structural information and chemical information at exactly the same position of a sample. The development of TEM has gone far beyond the pursuit of higher spatial resolution (e.g. by using high accelerating voltage and abbreviation correctors). In the past two decades, the “art” of in situ TEM has greatly advanced. People have been trying to move their experiments into the microscope, so that physical and chemical evolution can be recorded in real time whilst “reaction” happens. For example, in situ TEM is used to track surface atom migration in an Ag nanowire during deformation[29], image the martensitic transformation and amorphization in Si nanopillars during deformation[27], detect phase evolution

in electrode material in lithium ion battery during lithium ion insertion[131], investigate piezoelectric domain switching in a ferroelectric memory device[132], visualize how crystal grows from precursors[133] and reveal interaction of reactant gases and nanocrystal catalysts[134]. These studies directly and beautifully reveal the fundamental mechanisms in materials in response to external physical and chemical stimulus, providing fundamental pictures on how nature works as well as crucial information for rational design and processing of materials.

3.2.2 Contrast mechanisms of TEM

The contrasts in a TEM image can be categorized into mass contrast, diffraction contrast and phase contrast[135]. When electron beam passes through the material, it is deflected and absorbed by the specimen. Simply, when other factors (e.g. material type and orientation) are the same, sample regions with heavier elements and larger thickness absorb and deflect higher dose of the electron beam, and hence appear darker comparing to thin regions, giving rise to the mass-thickness contrast. In a polycrystalline material, the deflection of the electron beam is a function of crystal orientation; grains oriented on Bragg angles will defect more electron beam and hence appear brighter than those with crystal axis off the Bragg angles, giving rise to the diffraction contrast. TEM can also image the deflected beams generating diffraction pattern of the sample which contains information of the reciprocal space.

The parallel electron beams in TEM mode are synchronized and have the same wave length (or monochromatic). When the electron beams transmit through the periodic lattice of a crystal, the elastically deflected beam has the same wavelength as the transmitting beam; and hence it can interfere with the transmitting electron beam generating a phase contrast which contains the structure information of the crystal. Especially, when the crystal is on axis (in other

words, has a crystal zone axis parallel to the TEM electron beam), the interference can generate a 2-dimensional “atomic-resolution” image (also known as high resolution TEM or HRTEM) of the projection of the crystal along the zone axis. It should be noted that the bright dots in HRTEM images cannot be directly interpreted as atoms, image simulations are generally needed to accurately interpret the HRTEM image. Though, when the spatial resolution of the TEM image is larger than the minimum distance between atom columns, a one-to-one correspondence can be established between the bright dots and the atom columns.

In a scanning transmission electron microscopy (STEM), the electron beam is converged into a sharp “probe”. When the probe scans on the atom column, it is deflected; and on vacant sites, it is transmitted. By collecting the intensity of the deflected beam using an annular detector (e.g. high angle annular dark field detector, or commonly known as HAADF), atomic resolution images can be achieved. Since the total intensity of the high angle deflection is proportional to Z^2 (Z is the atom number of the element), the contrast acquired by HAADF-STEM can be directly linked to the Z number of the atom column. As such, the contrast of a HAADF-STEM image is also called Z-contrast. A great advantage of the STEM image over the TEM image is that STEM image can be directly interpreted without image simulation. However, due to the time required for point-to-point scanning, the temporal resolution of STEM is normally much lower than HRTEM. Besides, compared with HRTEM, atomic resolution STEM image is more sensitive to sample drift and crystal orientation changes during continuous straining in mechanical tests. Therefore, HRTEM imaging mode was used for this investigation. The true atomic-resolution HAADF-STEM was only occasionally used to verify the atomic structure of the static twin boundary.

3.2.3 Limitations of TEM

In situ TEM is limited by its temporal resolution, which is normally ~0.1s with conventional charge-coupled device (CCD). However, the speed of transformation (e.g. twinning nucleation), can approach the speed of sound (~340 m/s). Thereafter, TEM is not able to capture the instantaneous nucleation process. Besides, the lifetime of the defects that mediated the twinning is inversely proportional to the crystal size, which can be extremely short in nanosized crystals. Therefore, capturing details of these transformations require an extremely high frame rate, which is far beyond the capability of current TEM cameras. However, since the migration of twinning dislocations and twin boundaries is driven by stress, these defects may be captured by adopting extremely low strain rate (~10^{-3} s^{-1} here) and temporarily stopping the straining for imaging.

In addition, TEM image is acquired from the electron beam that transmits through the thickness direction of a sample. Therefore, when the transformation only happens at local regions along the thickness direction, information from both transformed and untransformed regions will be overlapped, giving rise to a complicated image contrast that is extremely hard for direct interpretation. For example, at the nucleation stage of a twin, the small twin embryo is embedded in the matrix along the thickness direction; and hence atomic resolution HRTEM imaging of the incipient twin embryo is difficult.

3.2.4 Determining twinning modes using HRTEM images

During tensile and compression experiments, all defects (including deformation twinning, dislocation, stacking fault and phase transformations) can be determined in HRTEM images based on their unique atomic-scale lattice structure. In HRTEM images, when the crystal is

orientated on zone-axis, each column of atoms is imaged directly. Any kind of irregularity or defects in the crystal lattice can be visualized directly under desired zone-axis (or orientation). Figure 3.1 presents examples on how to identify twinning modes and dislocation in HCP crystals. Figure 3.1b-c show the positions (represent by angles with the basal plane) of twinning planes viewing on corresponding plane of shear; Figure 3.1d shows an <***a***>-type full dislocation on the basal plane; the dislocation is identified and analyzed by drawing a Burgers circuit on the apparent defective area; Figure 3.1e-f show propagating coherent and incoherent twin boundaries of the {1 0 -1 2} twin, respectively; the twinning mode is identified by the orientation of the coherent twin boundary (i.e. by K_1); as for the incoherent twin boundary which has no obvious mirror symmetry, the twinning mode is determined by the shear plane (i.e. the viewing plane) and the misorientation between the matrix and twin.

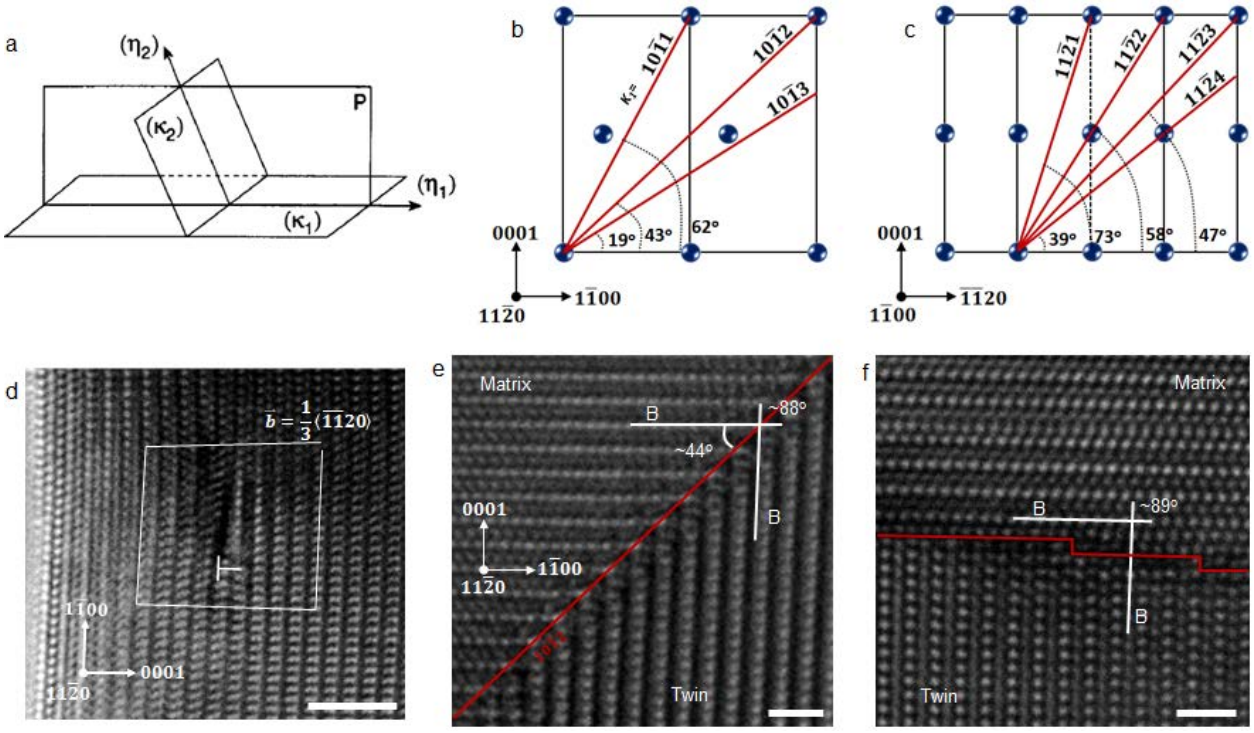

Figure 3.1 Twinning elements for the 7 active twinning modes in HCP metals (a-c) and determination of dislocations, coherent twin boundaries, and incoherent twin boundaries using HRTEM images (a) Schematic illustration of the 4 elements that defines a twinning mode[19]. (b-c) Schematic images showing 7 twinning planes (see red lines) on their respective plane of shear. (d) HRTEM image of an <***a***>-type dislocation. White square is Burgers circuit. (e) HRTEM image of a coherent {1 0 -1 2} twin boundary viewing along its plane of shear; the angles between parent and twin basal (B) planes and twinning planes are indicated. (f) HRTEM image of an incoherent twin boundary; the angle between parent and twin B planes indicates that it is {1 0 -1 2} twin. Scale bar in (d-f), 1 nm.

3.3 IN SITU TEM SETUP

For in situ TEM observation, FEI 80-300 Titan ETEM (Oregon, USA) equipping with an imaging lens spherical aberration corrector is employed (Figure 3.2). For in situ STEM observation, FEI 80-300 Titan STEM (Oregon, USA) equipping with a condenser lens spherical

aberration corrector is used. During the in situ experiments, the dynamic deformation processes are recorded by using a CCD at a few frames per second; snapshots of the deformation process are captured in the meantime. The TEMs operate at 300 *KeV* with ~0.10nm point-to-point resolutions after correction. The resolution is much smaller than the minimum distances between atoms columns in the projection view of the shear plane (~0.23nm for {1 1 -2 0} and ~0.27nm for {1 -1 0 0}). As such, atomic information of the deformation process can be unambiguously captured on the plane of shear. Furthermore, the aberration-corrected TEMs were able to minimize the "delocalization" effect on the TEM image, making it perfect to image processes happening on surface and interfaces.

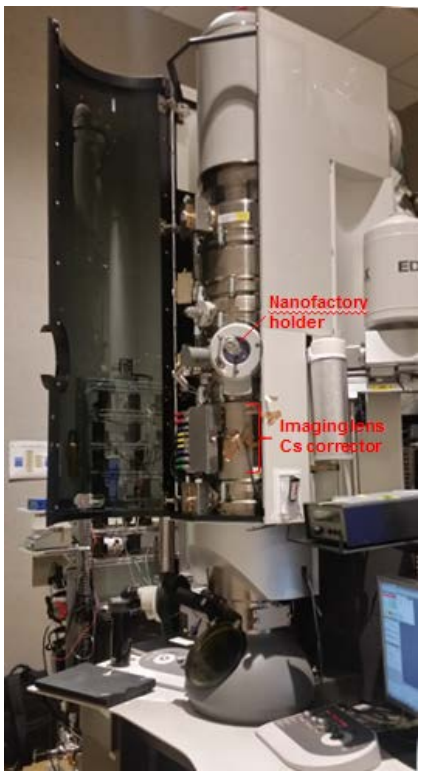

Figure 3.2 FEI Titan 80-300 TEM with imaging lens spherical aberration corrector at Environmental Molecular Science Laboratory of Pacific Northwest National Labs

A Nanofactory-STM holder is used for the in situ tension and compression tests (Figure 3.3a). There are two stages on the holder for loading sample: a fixed-stage on the left and a piezo-stage on the right. The piezo-stage is controlled by a piezo-system that can manipulate 3D motion of the sample at a sub-nanometer precision. The Re rods are loaded on both stages of the holder, with the fresh fractured surfaces facing each other. Monitored under TEM, the Re "nanotips" on the piezo-side is manipulated precisely to contact the "nanotips" on the fixed-stage (Figure 3.3b). Upon contact, an electric pulse is applied to weld the two Re nanocrystal together. Bi-crystal with a grain boundary forms in the process when the contacting nanotips have different orientations (Figure 3.3c); single-nanocrystal forms when the contacting nanotips have the same orientations (Figure 3.3d). Then, in situ straining experiments can be conducted by moving the Re nanocrystal on the piezo-stage using the piezo-system at a constant strain rate ($\sim 10^{-3}$ s^{-1}). Then the deformation inside the as-synthesized bi-crystal or single-crystal can be captured by using CCD under desired operation mode of TEM. This in situ setup has been widely used in previous publications on the deformation of Ag[136], Au[137], W[26] and Ta[138].

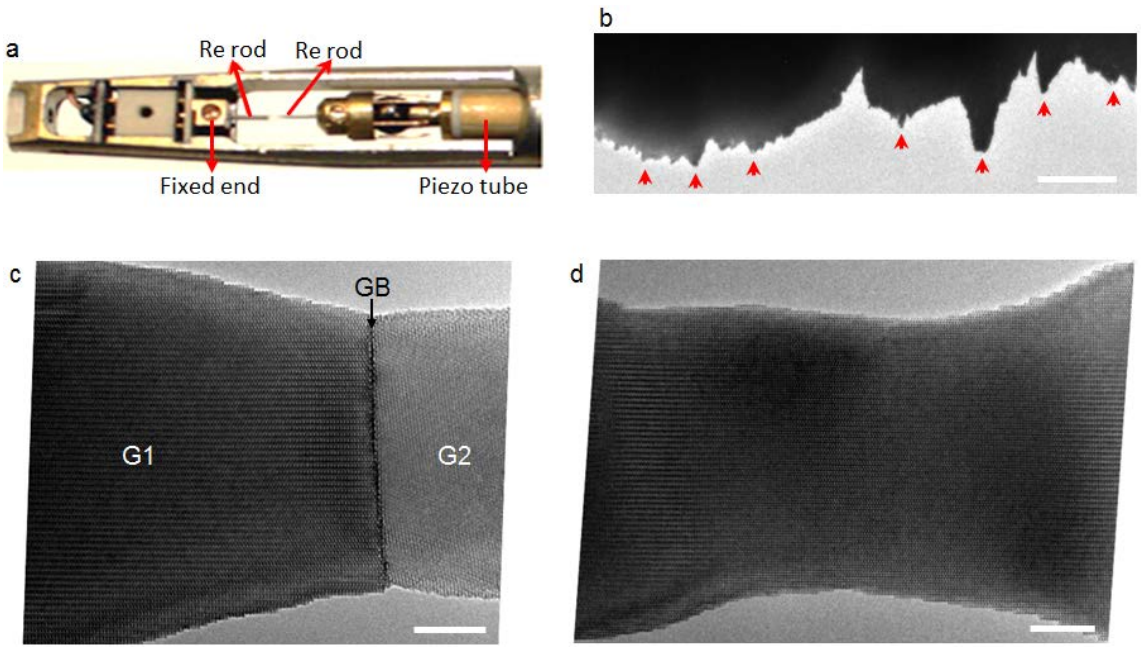

Figure 3.3 In situ TEM setup and sample processing technique. (a) The nanofactory-STM platform. (b) The "nanotips" (red arrows) induced on a Re rod. The nanotips are driven to contact with each other. An electric pulse is used to weld them together. (c-d) Examples of bi-crystal and single-crystal synthesized using this method. Scale bar in (b), 500 nm; scale bars in (c, d), 5 nm.

4.0 IN SITU TEM INVESTIGATION OF {1 0 -1 2} TWINNING

4.1 INTRODUCTION

{1 0 -1 2}<1 0 -1 -1> twinning (or simply {1 0 -1 2} twinning) is the most prevalent twinning mode in HCP structures[56]; it has been reported in almost all HCP metals including, for example, Ti[78,139], Mg[43], Zr[140], Zn[77], Re[123], Co[141], Ca[112] etc. However, the behavior of this twinning mode is rather perplexing from a standpoint of conventional understanding of twinning. For instances, characterizations on deformed HCP metals showed that considerable part of the twin boundaries depart from the theoretical twinning plane and reside dominantly on the B|P and P|B interfaces, i.e. twin basal facing parent prismatic or parent basal facing twin prismatic[89,93]; orientation relation between the matrix and twin widely departs from that of ideal mirror symmetry[89]; twinning nucleation and propagation are not driven by shear and can violate the Schmid's law[90-92]; moreover, it has a weak interaction with matrix dislocations as well as concomitant slip in front of the twin tip, and can completely change the orientation of an entire grain[22,58]. To explain these abnormal behaviors of the {1 0 -1 2} twinning, various mechanisms of the twinning nucleation and growth have been developed. For example, interfacial defect theory was adopted by defining and describing the transition of interfacial defects on the B|P and P|B interfaces into twinning dislocations on the twin plane[50,58,84,99]; alternatively, pure-shuffle models were proposed for both twinning nucleation[100] and growth[43,101]. Unfortunately,

neither mechanism can satisfactorily address all behaviors of the {1 0 -1 2} twinning, and they are under intense discussion as they cannot reconcile with each other[102,104,142]. For decades, researches on the mechanisms of {1 0 -1 2} twinning relies largely on topological analysis, computational simulations and ex situ experimental observations; yet they remain in mystery and intense debating. Given that the validity of topological modeling or computational simulations critically depends on an accurate description of the interatomic potentials[18,92], and that ex situ experimental characterizations on post-deformation samples can be misleading due to the strong tendency for detwinning upon unloading which, especially, makes it impossible to capture the twin embryos in unloaded samples[114,117]. Therefore, atomic-resolution direct observation on the twinning process is generally believed essential for obtaining an accurate mechanistic pictures of the twinning nucleation and growth in HCP crystals[52].

In this chapter, by using state-of-the-art in situ TEM, we carried out unprecedentedly atomic-scale direct observation of the {1 0 -1 2} twinning process in HCP metal. The results unambiguously uncovered the atomistic mechanisms of the {1 0 -1 2} twinning nucleation and growth, featuring with a dominant role of atomic shuffles in both processes. The findings depart from the conventional idea that twinning formation is shear-dominated. The twinning dislocation-mediated twinning was only dominant during detwinning and instantaneous reloading.

4.2 EXPERIMENT PROCEDURES

The tests procedures were, in general, the same as those described in Chapter 3.3; except that the loading orientation of the Re nanocrystals were oriented to favor {1 0 -1 2} twinning, and the

observation direction of the Re nanocrystals were adjusted such that the twinning planes belonging to the favorable {1 0 -1 2} twinning mode were edge-on and hence shear and shuffles could be directly captured. Here, compression were applied along <1 -1 0 0> or tension applied along [0 0 0 1]. In the meantime, the <1 1 -2 0> or <1 1 -2 -3> axis of the nanocrystal was aligned with the electron beam, so that the imaging could be made with {1 0 -1 2} twinning planes edge-on; particularly, imaging along <1 1 -2 0> axis enabled observation of the twinning process at high resolution on the shear plane. In addition, the strain rate was controlled to be ~10^{-3} s^{-1} in all tests.

4.3 RESULTS

4.3.1 In situ HRTEM observation of {1 0 -1 2} twinning nucleation

Figure 4.1 showed the nucleation process of a {1 0 -1 2} twin in a Re bi-crystal under <1 -1 0 0>-oriented compression. The viewing direction was normal to the shear plane, i.e. <1 1 -2 0>. The crystal initially deformed elastically (Figure 4.1b); then plastic deformation started by twinning nucleation on the (0 0 0 1) side surface of the crystal (Figure 4.1c). The incipient twin embryo had a rectangular shape and was primarily bounded by B | P and P | B interfaces, i.e. twin basal plane facing matrix prismatic plane (B | P) or twin prismatic plane facing matrix basal plane (P | B). In subsequent compression, the twin embryo grew by transformation of matrix prismatic planes into twin basal planes (P→B transformation), which was manifested by the formation of new twin basal planes on the B | P interfaces and lateral expansion of the existing twin basal planes (Figure 4.1c-e). Viewing along the <1 1 -2 0> direction, the angle between

twin basal plane and the parent basal plane was ~86^{o}, proving that the embryo was indeed a {1 0 -1 2} twin (refer to Figure 3.1f). The {1 0 -1 2} twin embryo was unstable and instantly de-twined upon unloading (Figure 4.1f).

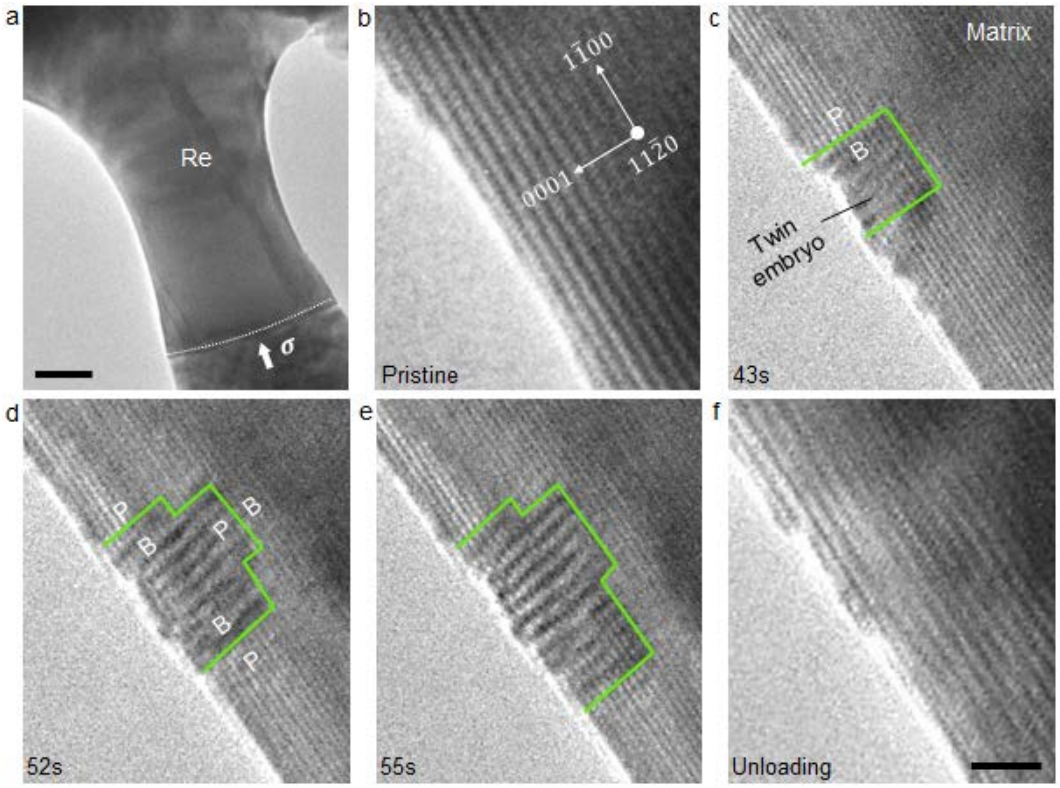

Figure 4.1 {1 0 -1 2} twin nucleation on the side surface of a Re bi-crystal under <1 -1 0 0>-oriented compression. The viewing direction is <1 1 -2 0>, i.e. normal to the plane of shear for {1 0 -1 2} twinning mode. (a) TEM image of the pristine Re pillar. White block arrow indicates loading direction. Dashed white line indicates grain boundary of the bi-crystal. (b) HRTEM image of the nanocrystal side surface before compression. (c) Onset of plastic deformation by nucleation of a {1 0 -1 2} twin which is indicated by a green box. (d-e) Sequential HRTEM images showing growth of the {1 0 -1 2} twin embryo. (f) The {1 0 -1 2} twin embryo fully detwinned upon unloading. Scale bar in (a), 20 nm; scale bar in (f), 2 nm.

Figure 4.2 showed another case of {1 0 -1 2} twin nucleation on the (0 0 0 1) side surface of the Re crystal, wherein lattice of the twin embryo was much clearer. Similar to that shown in Figure 4.1c, the twin embryo was dominantly bounded by B│P and P│B interfaces rather than the theoretical twinning planes (as indicated by the green and yellow lines in Figure 4.2b). The twin embryo growth was fast; and during the process, the twin embryo remained on B│P and P│B interfaces and no twinning dislocation was identified. Fast Fourier transformation (FFT) of the twin embryo and nearby matrix indicated that the {1 0 -1 2} planes in the twin and matrix were not parallel, indicating a breakdown of invariant plane strain condition during the twinning nucleation process. Figure 4.2c schematically depicted the P→B transformation-mediated twinning nucleation from surface; apparently, only small shuffles were required in the process due to the structural similarity between the P and B planes. If we superimpose a basal plane (B) with a prismatic plane (P), a striking structural similarity between B and P was revealed (Figure 4.2d); as indicated by the red arrows, only small shuffles (indicated by red arrows) were needed to accomplish the observed P→B transformation. During the process, the corrugated prismatic plane in matrix (outlined black) was transformed to the flat basal plane in twin (outlined green).

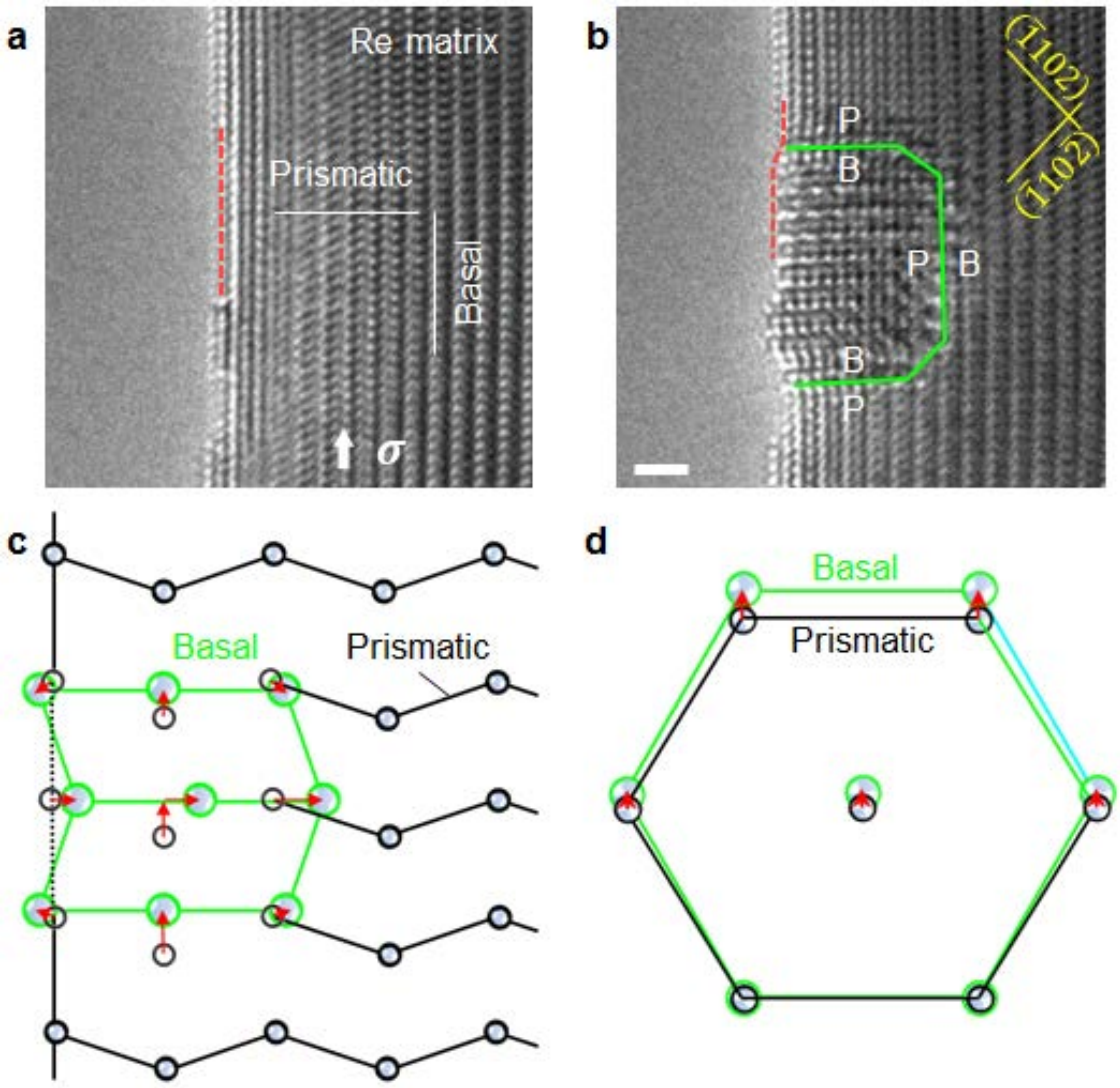

Figure 4.2 In situ observation and schematic illustration of a {1 0 -1 2} twinning nucleation on the side surface of a Re crystal under <1 -1 0 0>-oriented compression. The viewing direction is <1 1 -2 0>, i.e. normal to the plane of shear for {1 0 -1 2} twinning mode. (a-b) Sequential HRTEM snapshots showing twin nucleation (enclosed in green lines). The twin boundaries are primarily interfaces of basal (B) and prismatic (P) planes, instead of the theoretical twinning plane (indicated by yellow lines). (c) Schematics of the nucleation process by transformation from parent P to twin B. (d) Superimposed view of a B (green atoms and hexagon) and a P (black atoms and hexagon). The striking structural similarity between B and P planes permits the observed direct transformation. Scale bar in (b), 1 nm.

{1 0 -1 2} twinning nucleation did not always take place on the (0 0 0 1) surfaces; twin nucleation events were also found on non-(0 0 0 1) surfaces (Figure 4.3), grain boundaries (Figure 4.4), and at dislocation core (Figure 4.5). Figure 4.3 showed an example of {1 0 -1 2} twinning nucleation on a non-(0 0 0 1) surface area. Possible nucleation sites along the thickness direction were illustrated in Figure 4.3b; considering the strain compatibility condition provided by the surface, top or bottom surfaces should be more likely nucleation site than the crystal interior. The geometry, boundary, and dynamic behavior of this twin embryo appeared to be the same as those described in above cases (see Figure 4.1 and Figure 4.2). Figure 4.4 showed the {1 0 -1 2} twin nucleation event on the grain boundary of a Re bi-crystal. The low-angle tilt "grain boundary" should favor twinning due to the easy strain compatibility across the grain boundary[123]. Incipient plastic deformation started at a local region of the grain boundary with the nucleation of a {1 0 -1 2} twin embryo containing only a few unit-cells (Figure 4.4a). In subsequent compression, the embryo grew via P→B transformation, as manifested by the formation and extension of basal layers of the twin; note that the twin embryo was bounded by B│P-type interfaces during its growth (Figure 4.4b-d). Similar to above nucleation events, this twinning nucleation process appeared to involve no twinning dislocation activities on the twinning plane, which was also supported by the fact that the {1 0 -1 2} twinning planes in the matrix and twin were not parallel (see the FFT in Figure 4.4e). Moreover, the angle between B and P in the twin embryo was 87^{o} rather than 90^{o} (of an undistorted lattice), implying that the embryo lattice was distorted (Figure 4.4e); lattice distortion was also identified in the surrounding matrix, which was likely due to the intrinsic misfit on the B│P-type twin boundaries and made the atomic shuffles during initial nucleation more complex (than those described in the simple topological analysis[101]).

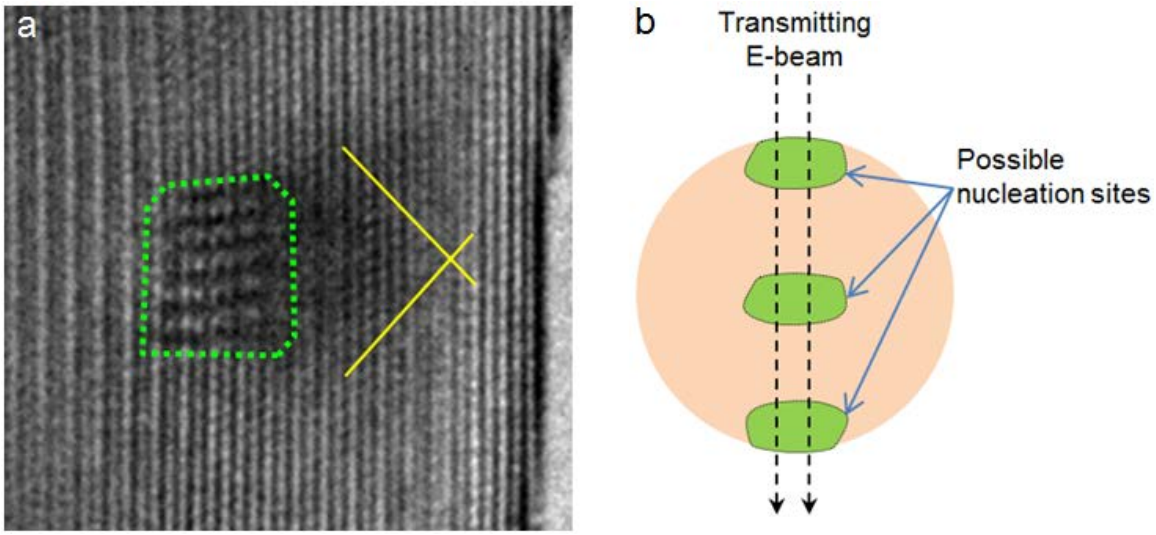

Figure 4.3 {1 0 -1 2} twinning nucleation "apparently" inside a Re crystal. (a) HRTEM image of a {1 0 -1 2} twinning nucleation "inside" the Re crystal which was under <1 -1 0 0>-oriented compression and viewed along <1 1 -2 0> direction. (b) Schematic illustration of the possible position of the twin embryo since the TEM images is a projection view along the sample thickness direction. And, the twinning nucleation site was more likely the top or bottom non-(0 0 0 1) surface than the crystal inside, due to the strain compatibility condition provided by the free surface.

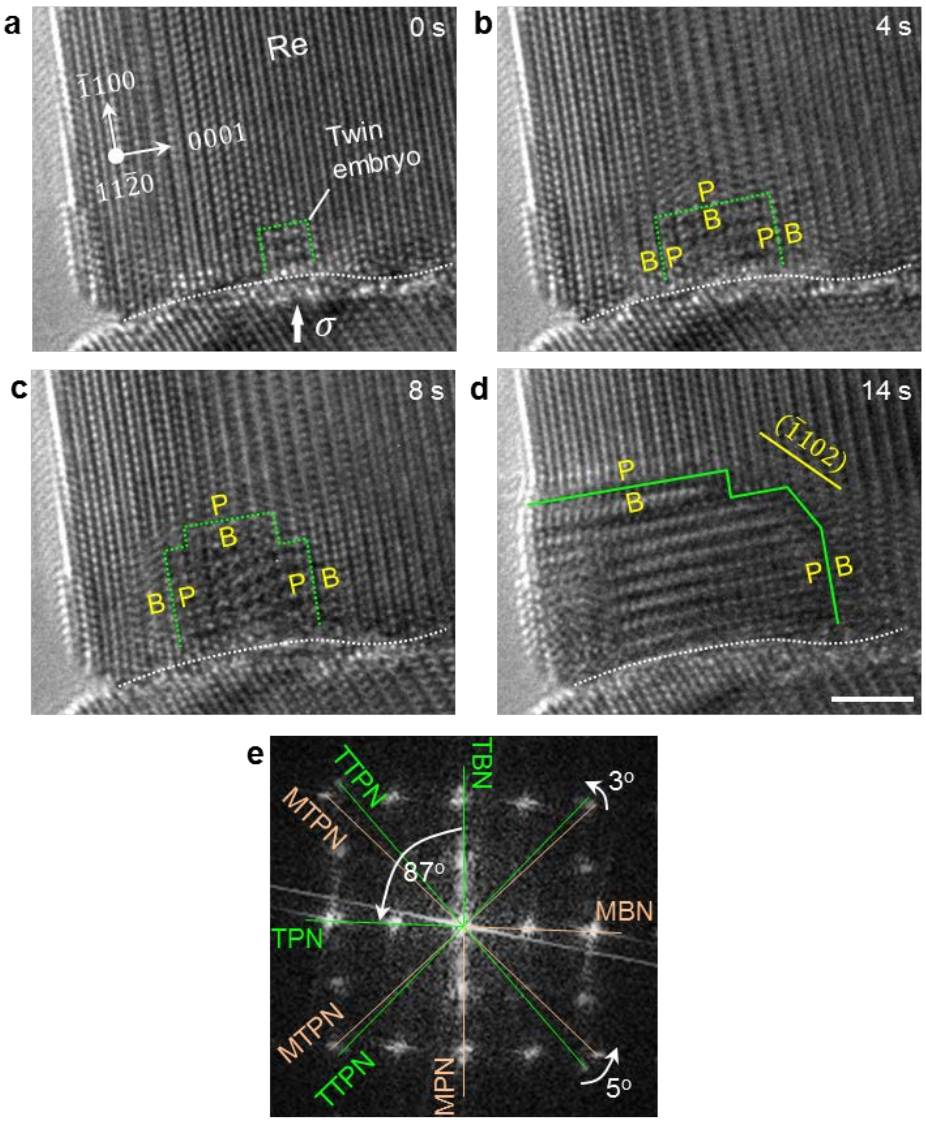

Figure 4.4 {1 0 -1 2} twinning nucleation on a low angle grain boundary. (a-d) Sequential HRTEM snapshots showing twinning nucleation on the grain boundary in the upper crystal. The twin boundaries (green lines) were primarily B|P-type interfaces, instead of the theoretical twinning plane (yellow lines in (d)). The twin embryo expanded by P→B transformation. (e) FFT of the twin embryo in (d). The normal of basal, prismatic and twinning planes in the twin and matrix are marked as TBN (twin basal normal), TPN, TTPN and MBN, MPN, MTPN respectively. As a result of P→B transformation, TBN is parallel to MPN; TPN is parallel to MBN; while TTPN and MTPN are not parallel. Moreover, the lattice of the twin embryo is distorted as manifested by the 87^o angle between TBN and TPN which should be 90^o in an undistorted lattice. Scale bar in (d), 2 nm.

{1 0 -1 2} twinning nucleation event was also identified near the dislocation core. Figure 4.5a-d showed sequential HRTEM snapshots of this process in a Re single-crystal under <1 -1 0 0>-oriented compression. The twin nucleated right next to the core of a pre-existing <***a***>-type edge dislocation (Figure 4.5b-c). Quantitative geometrical phase analysis[143,144] revealed the strain field of the dislocation core (see Figure 4.5e). By filtering the TEM image using the reflections in FFT from the twin basal (Figure 4.5h), the basal layers of the twin embryo was revealed (Figure 4.5f-g). By overlaying the filtered TEM image and the strain distribution image, it was found that the twin nucleated right at the compressive strain field of the dislocation core, manifesting that the edge dislocation acted as a "prompter" or a "seed" for the {1 0 -1 2} twinning nucleation. It should be noted that the twinning nucleation started more likely at the top or bottom end of the dislocation (where the dislocation met the sample surface), due to the strain compatibility condition provided by the sample surface.

In subsequent straining, the embryo grew as shown in the sequential filtered TEM images in Figure 4.5f-g, and finally seized the whole area (Figure 4.5d). Though, the detailed transformation mechanism was too fast to be captured; it proceeded likely by the P→B transformation, since the twin basal planes were parallel to the matrix prismatic planes (see Figure 4.5h).

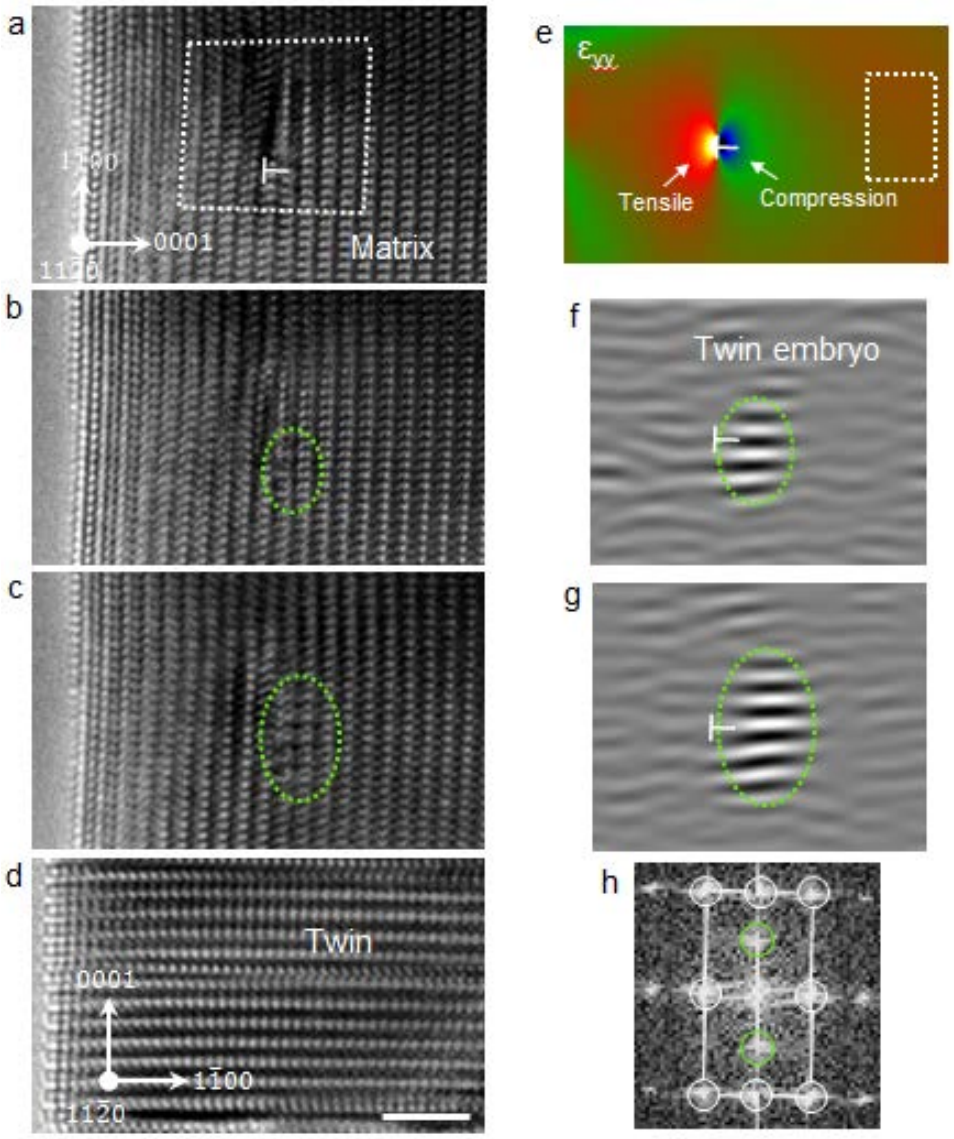

Figure 4.5 Twin nucleation assisted by the strain field of an <***a***>-type edge dislocation on the basal plane. The Re nanocrystal was under <1 -1 0 0>-oriented compression and viewed along <1 1 -2 0> direction. (a-d) Sequential HRTEM images showing nucleation, growth of a twin embryo nearby an <***a***>-type edge dislocation on the basal plane. White dashed lines indicate the Burgers circuit. Green circles mark the region of twin nucleation. (e) Relative compressive strain (ε_{yy}) map around the dislocation core in (a), generated by geometric phase analysis. Boxed region is the reference region. (f-g) Inverse FFTs of panel (b-c), using the twin (0 0 0 1) reflections (green-circled spots) in the FFT (h). White circles and lines indicate the reciprocal lattice of the matrix; green circles indicate that of the twin embryo. Scale bar in (d), 2 nm.

4.3.2 In situ HRTEM observation of {1 0 -1 2} twinning growth

4.3.2.1 {1 0 -1 2} twinning growth by P→B transformation

A typical example of {1 0 -1 2} twinning growth is shown in Figure 4.6a-c. With increasing strain, the twin embryos grew into large twins that were predominately bounded by P│B and B│P interfaces which were also unambiguously revealed by the atomic-resolution STEM images in Figure 4.7. Similar to the twinning nucleation process (see Figure 4.1 and Figure 4.4), {1 0 -1 2} twinning growth was also mediated by direct P→B transformation, as shown in the sequential HRTEM images in Figure 4.6d-h. During the twinning growth, new basal layers nucleated at the junction of the P│B interface and (0 0 0 1) surface, which then expanded laterally inward by transforming the matrix prismatic planes. The P→B transformation process (Figure 4.6f) was leaded by a series of "steps" or interfacial defects on the P│B interface; each step carried a single-layer or multi-layers of twin basal planes (or matrix prismatic planes). These interfacial defects migrated as the prismatic planes in matrix transformed into basal planes of twin following a one-to-one planar correspondence. It should be noted that the twinning growth process was apparently dominated by the P→B transformations rather than by twinning dislocations which was not identified in our sample, and hence the twin boundaries were dominantly B│P-type interfaces (see Figure 4.6 and Figure 4.7). Additionally, the angle between the twin basal plane and matrix basal plane varied between 90^{o} and 86^{o}, implying a lack of mirror symmetry across the twin boundary. Surprisingly, no disregistry or interfacial dislocation was identified on or nearby the B│P-type twin boundaries (see Figure 4.7), likely due to the nanoscale sample size allowing the intrinsic misfit strains on the B│P-type interfaces fully resolved by the sample.

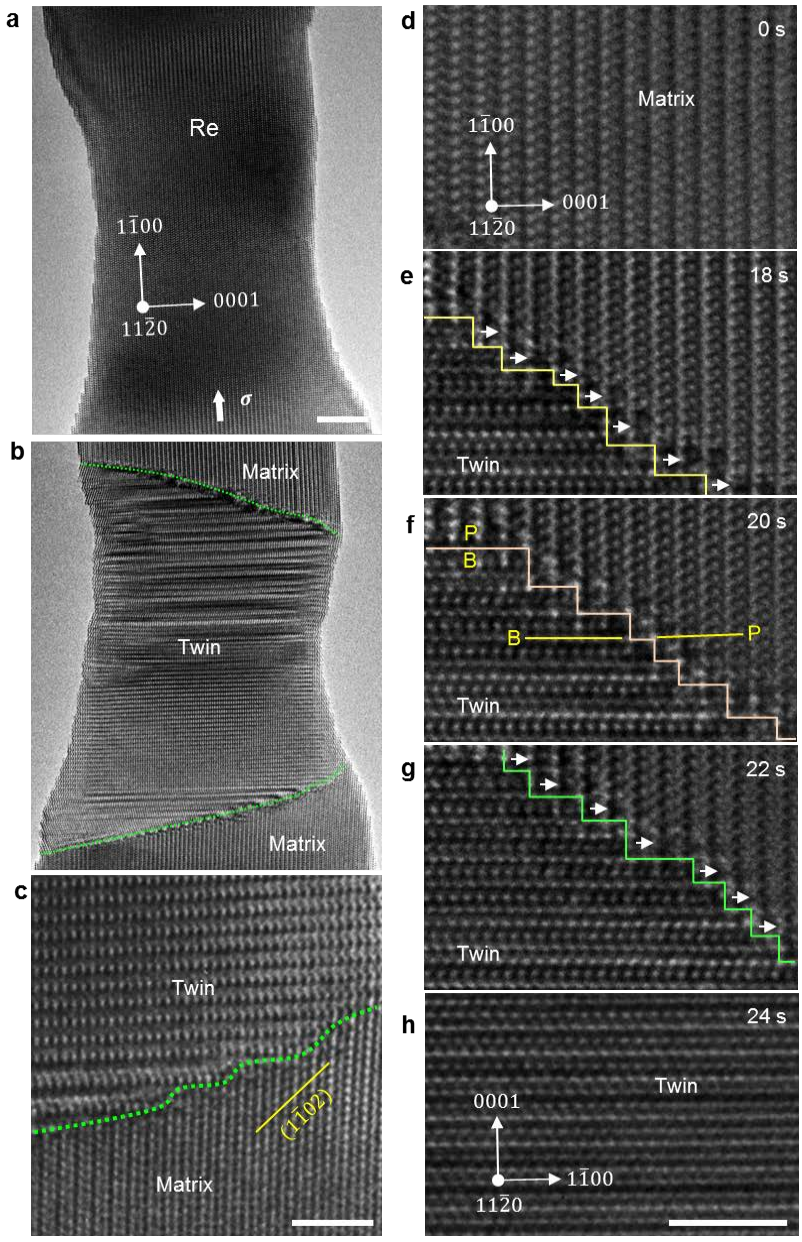

Figure 4.6 {1 0 -1 2} twinning growth via P→B transformation. (a-b) Sequential HRTEM images showing twinning in a Re crystal under compression along <1 -1 0 0>. (c) Magnified view of the twin boundaries (green lines) which are primarily P│B segments and largely depart from the twinning plane (yellow lines). (d-h) Sequential HRTEM snapshots showing migration of the twin boundaries (colored lines) during the twinning growth in a separate specimen. The twin boundary comprises a series of B│P and P│B interfaces. Twin grows via P→B transformation. Arrows indicate lateral expansion of the twin basal planes by transformation of matrix prismatic planes. Scale bar in (a), 5 nm; scale bars in (c, h), 2 nm.

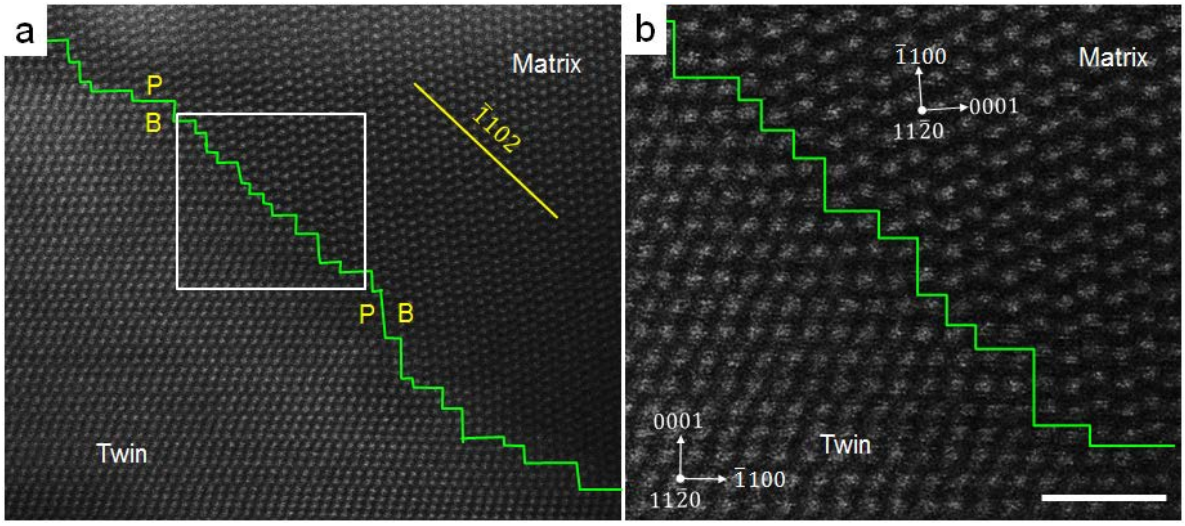

Figure 4.7 Atomic resolution STEM-HAADF image of the twin boundary during {1 0 -1 2} twinning growth in Re crystal. Panel (b) shows an enlarged image of boxed region in (a); the twin boundaries are B│P-type interface rather than coherent twin boundaries on the twinning plane. No disregistry or interfacial dislocation was identified on the twin boundary. Scale bar in (b), 1 nm.

4.3.2.2 Detwinning via P→B transformation and twinning dislocations

In our in situ observations, the as-formed {1 0 -1 2} twin always spontaneously detwined upon unloading and sometimes fully detwined when reverse loading could be applied. During the detwinning process, the twin boundaries retreated from the incoherent B│P-type interfaces and relocated to coherent twin boundaries (CTB) on the {1 0 -1 2} twinning plane (see Figure 4.8). Since external driving force was removed, the detwinning might be driven by the interfacial energy. Thus, the incoherent B│P-type interfaces tended to align with the theoretical twinning plane to reduce the interfacial energy[145].

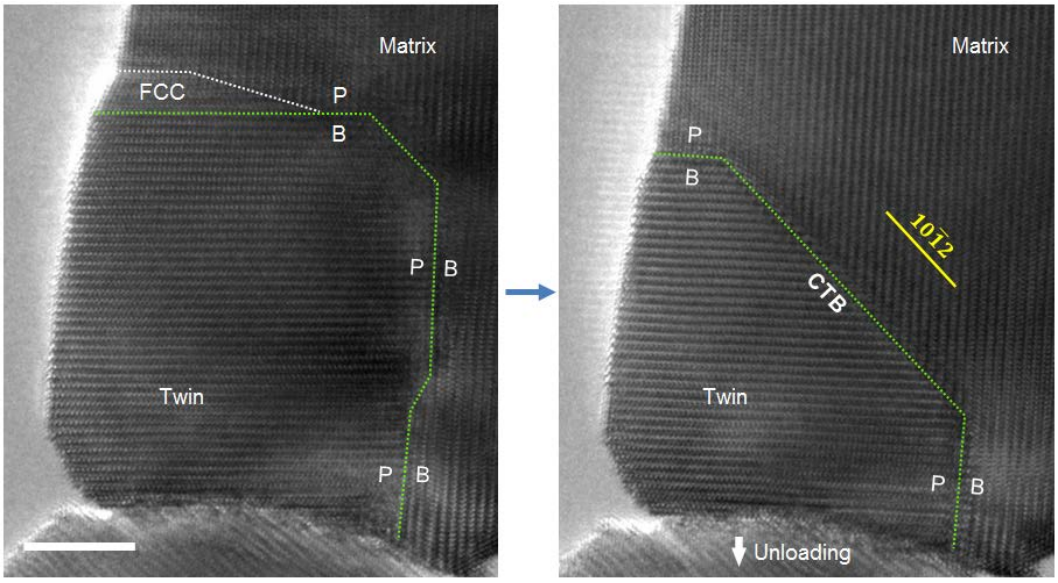

Figure 4.8 Detwinning process of a {1 0 -1 2} twinning upon unloading. During the process, twin boundaries retreated from B | P-type interfaces and relocated to coherent twin boundaries (CTB). Scale bar, 5 nm.

Impressively, the subsequent migration of CTB was mediated by the twinning dislocation mechanism. As shown in the sequential HRTEM images in Figure 4.9a, "step defects" are nucleated by "etching" the P | B interface on the lower-right corner of the image; then, these "step features" moved upwards along the CTB and piled-up at the upper-left P | B interface which elongated as a result (Figure 4.9a). During this process, the inclined CTB sections moved rightwards and contemporarily the twin shrunk. Circuit analysis[146] shows that each "step feature" contains two consecutive {1 0 -1 2} planes (Figure 4.9b) which is the same as the ($\boldsymbol{b}_2$, h_2) twinning dislocation[19,21,52,117]. Besides, as shown in Figure 4.9c, one of the twinning planes in the matrix and twin were perfectly parallel and the angle between the conjugate {1 0 -1 2} planes was 8^o, implying that the local twinning shear was consistent with classical expectation; as such, the "step features" on CTB were indeed the classical ($\boldsymbol{b}_2$, h_2) twinning dislocations. The twinning

dislocations on CTB migrated at a speed of ~4nm/s right after nucleation and slowed down dramatically to ~1nm/s as it approached those in the front, likely due to the repulsive interactions between them.

Comparing to the classical ($\boldsymbol{b}_2$, h_2) twinning dislocation, the twinning dislocation here should have different atomic shuffles. As shown in Figure 4.9c, the angles between prismatic and basal planes in both the twin and the matrix were 88^o rather than 90^o, implying that the lattices of matrix and twin across the CTB were distorted. As a result, the required atomic shuffles in transformation between the distorted lattices should be different from that in transformation between undistorted lattices[51].

Based on our observation, the B | P-type interfaces acted as sources as well as sinks of the ($\boldsymbol{b}_2$, h_2) twinning dislocations on CTB. At later stage of detwinning, the CTB sections decomposed into zig-zag B | P and P | B interfaces, indicating that the CTB acted as the source of interfacial defects on the B | P and P | B interfaces (see Section 4.3.2.1). Moreover, as shown in Figure 4.9a, the twinning dislocation on CTB might have induced the B→P transformation on the upper-left B | P interface, demonstrating the same process as that described in the interfacial defect mechanism[21,50,84,99]. Above all, these observations indicate a synergy of the "shuffle-dominated"[100,101] and "shear-dominated"[19,21,52,117] twinning mechanisms in the detwinning process. In our observation, when CTB and twinning dislocations formed upon unloading, subsequent reloading stopped the detwinning and the twin started to grow by the synergy of twinning dislocations movement on the CTB and P→B transformation. It should be noted that the length of CTB gradually shrunk and finally overwhelmed by the B | P-type interfaces during reloading; and thereafter, the P→B transformation re-dominated the subsequent twinning.

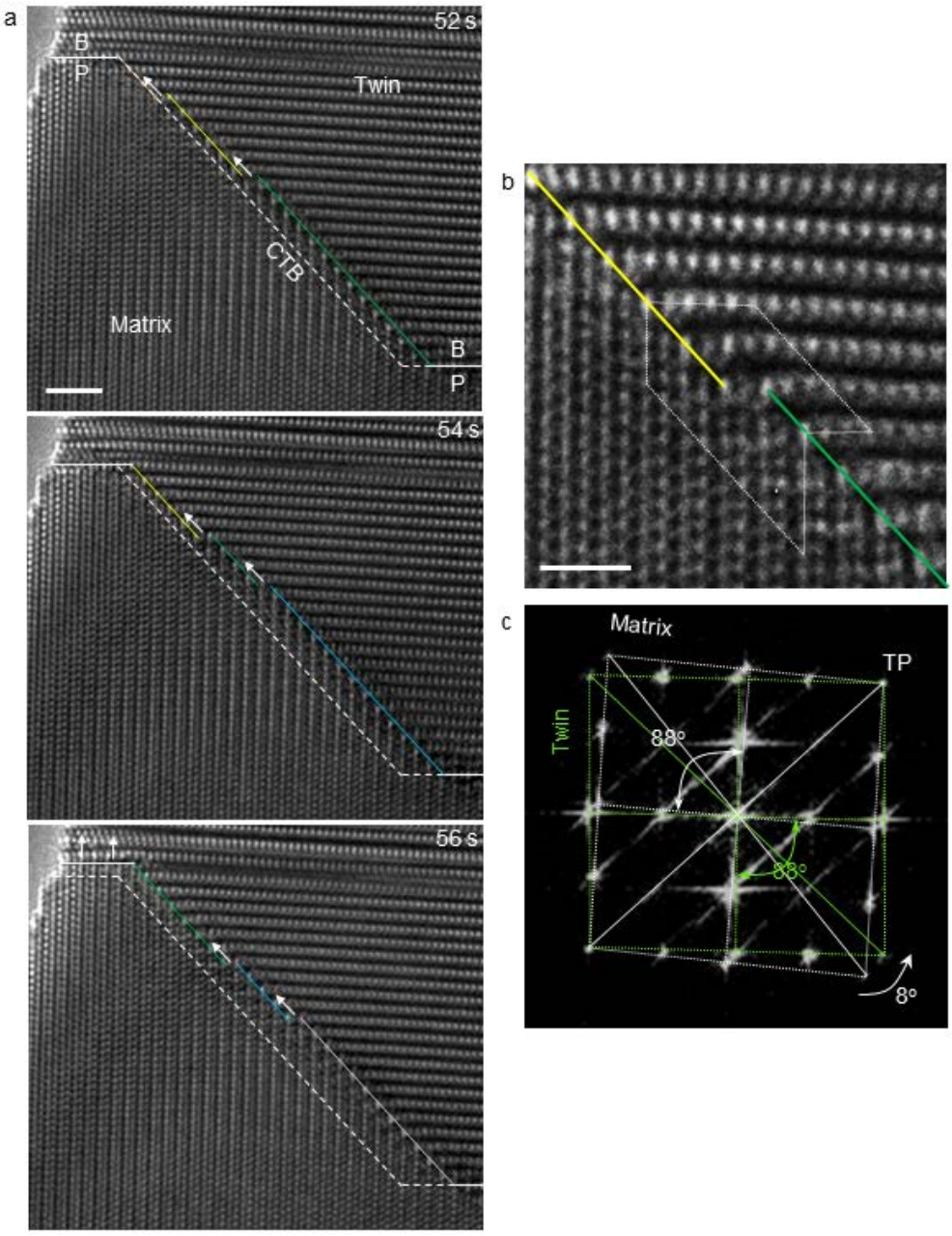

Figure 4.9 Twining dislocations mediated detwinning of a {1 0 -1 2} twin. (a) Sequential HRTEM images showing the detwinning process during unloading. Sections of CTBs are discerned by colored lines. The twinning dislocations were nucleated from the lower-right P│B interface, migrated upwards, and annihilated at the upper-left P│B interface. White dash line is reference for tracking the migration of CTB. (b) Enlarged HRTEM image of the ($\boldsymbol{b}_2$, h_2) twinning dislocation on CTB. (c) FFT of the matrix and twin across the CTBs, showing lattice distortion in the matrix and twin. Scale bar in (a) 2nm; scale bar in (b) 1 nm.

4.4 DISCUSSION

4.4.1 P→B transformation-mediated twinning nucleation

In above Section 4.3.1, we have demonstrated several typical events of {1 0 -1 2} twinning nucleation on surface sites ((0 0 0 1) and non-(0 0 0 1)), grain boundary and dislocation core. Independent of the nucleation site, all the observed twinning nucleation processes were mediated by prismatic to basal (P→B) transformations, i.e. the matrix prismatic planes transformed into the twin basal planes. This process involved no twinning dislocations as described in pole mechanism[41,112] or in zonal twinning dislocation mechanisms[46,114]. Should twinning dislocation mechanism dominated the twinning, the twin nucleus would be bounded primarily by the CTB rather than B│P-type interfaces. Moreover, twinning dislocation-related mechanism requires that the twinning plane should be invariant during the twinning process. Yet, as shown in Figure 4.4e, the twinning planes in the twin and the matrix were not parallel, demonstrating that the transformation was not invariant plane strain as described in the shear-dominated twinning model and hence excluding the dominant rule of twinning dislocation in the {1 0 -1 2} twinning nucleation process. On the other hand, the P→B transformation-mediated twinning nucleation appeared to be consistent with the shuffle-dominated twinning mechanism[100,101], except that the incipient twin embryos are highly distorted (see Figure 4.2 and Figure 4.4).

It should be noted that the scarcity of pre-existing defects at such a small sample volume may have prevented the activation of the dislocation-related mechanisms (e.g. pole mechanism or dislocation dissociation mechanism[41,79]). As shown in the in situ results, {1 0 -1 2} twinning nucleation through P→B transformation did not necessitate pre-existing dislocations (Figure 4.1

and Figure 4.2). Note that free surface and low angle grain boundary may prompt the twinning nucleation via P→B transformation, presumably due to the strain accommodation conditions.

As for surface nucleation of twinning dislocations[46], the Schmid factor for the {1 0 -1 2} twinning dislocation under current test conditions was ~0.5 and that for basal slip was 0, meaning that surface nucleation of twinning dislocation was at its best odds in the competition with the P→B transformation[91]. It is well known that due to the increasing imaging force, the critical stress for dislocation nucleation from the surface of nanoscale samples increases dramatically[147]. As such, it is reasonable to expect a higher critical stress for the surface nucleation of twinning dislocation in smaller samples. On the other hand, the shuffle-dominated mechanism generates no shear on the twinning plane[109] and hence should be less sensitive to the imaging force and sample sizes. Therefore, it is reasonable to expect P→B transformation-mediated twinning nucleation in small-scale samples. This is indeed what has been found in our in situ TEM observations, wherein interfacial defects on B|P-type interfaces rather than twinning dislocations were nucleated from surface of the nanocrystal. In confined volume and local stress concentrations of bulk samples, the shear stress would be suppressed[148] and the normal stress on prismatic or basal planes could be high enough to activate the P→B mechanism. Referring to macroscopic findings on the twinning nucleation and growth, it is highly likely that the P→B transformation is a dominate mechanism of {1 0 -1 2} twinning in bulk samples.

It should be noted that the misorientation between the matrix and twin formed by P→B transformation was slightly different to that between the matrix and an ideal {1 0 -1 2} twin formed by twinning dislocations[108]. In a more rigid treatment, the P→B transformation was named as "twin-like lattice reorientation"[43] or simply as grain rotation[85]. Possibly due to the pre-existing defects or surface damage, previous studies did not find the subsequent transformation

from the "twin-like lattice reorientation" to ideal {1 0 -1 2} twinning as shown in our observation (see Figure 4.8 and Figure 4.9). Moreover, as shown in Figure 4.10, the prismatic plane in matrix transformed exactly to the basal plane in twin (i.e. P→B), and the basal plane in matrix was transformed exactly to the prismatic plane in twin (i.e. B→P), implying the lattice correspondence established by the P→B transformation is exactly the same as the classical definition of {1 0 -1 2} twinning[107,109]. As such, our observations imply that twinning can be formed by transformations that establish the "desired" lattice correspondence and shear-dominated process on the twinning plane is not a necessary requirement of twinning.

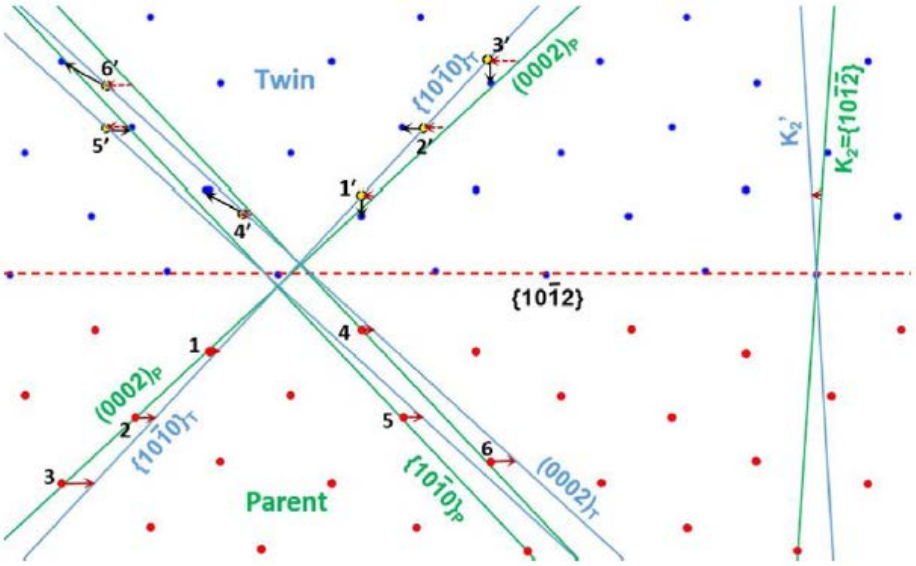

Figure 4.10 Topological illustration showing that the lattice correspondence of an ideal {1 0 -1 2} twinning gives P↔B correspondences[109]. The atoms in twin and matrix are colored blue and red, respectively. Clearly, the lattice correspondence requires that the K_1 plane (i.e. {1 0 -1 2}) is invariant; the K_2 plane (i.e. {1 0 -1 -2}) in parent corresponds to the K_2' plane (i.e. {1 0 -1 -2}) in twin; and importantly, the prismatic and basal planes in parent correspond to basal and prismatic in twin, i.e. P→B and B→P. The figure is reprinted from reference[109].

There are three immediate results from the P→B transformation-mediated twinning nucleation. First, as illustrated in Figure 4.11, P→B transformation generated normal strains on prismatic and basal planes[149] rather than homogeneous shear strain on the twinning planes (indicated by dash lines in Figure 4.11); therefore, the twinning nucleation process was not shear-dominated; and normal strains (compression on prismatic or tension on basal planes) can be the primary driving force for the {1 0 -1 2} twinning nucleation. Defects that can contribute such normal strains can prompt the P→B transformation and hence facilitate the {1 0 -1 2} twinning nucleation (see Figure 4.5a for example). Since the P→B transformation process does not require twinning dislocations, resolved shear stress on the twinning plane does not drive the twinning nucleation. This well explains the non-Schmid effect of twinning nucleation[90-92].

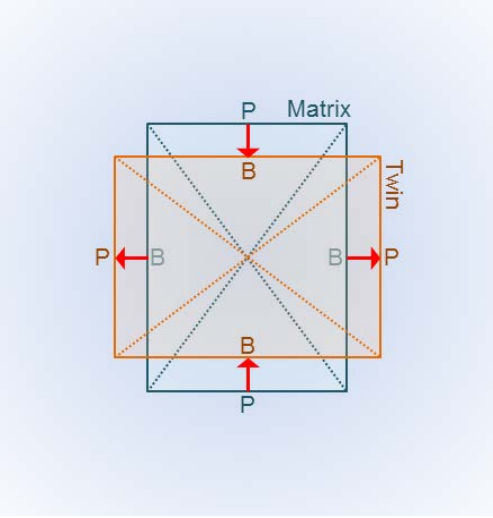

Figure 4.11 Schematic image showing the shape changes generated by P→B transformation in bulk sample (shade background). Blue and orange rectangles indicate the shape of matrix and twin, respectively. Note that the sizes of prismatic (P) and basal (B) planes are adjusted to exaggerate their difference. Dash lines indicate the twinning planes, which are obviously not parallel demonstrating the violation of invariant plane strain condition.

Second, since the P→B transformation does not require specific pre-existing defects, given appropriate loading orientation, stress concentration, and strain compatibility condition, the {1 0 -1 2} twinning can be readily and prevalently nucleated in all HCP metals. For instance, since the shape change as a result of twinning formation (see Figure 4.11) is tetragonal, under uniaxial compression on the prismatic plane (e.g. experiments in Figure 4.1-Figure 4.5), accommodation mechanisms are necessary for strain perpendicular to the basal plane. The (0 0 0 1) surface can provide such strain accommodation by forming surface "bumps", as indicated by the red dash lines in Figure 4.2. Moreover, it is reasonable to expect that possible surface reconstruction by physi-chemi-adsorption or alloying may play a role in the twinning nucleation process. The low angle grain boundaries can provide the strain accommodation by deformation in the other grain (Figure 4.12). In the meantime, stress concentrators at grain boundary, surface step and dislocation core provide favorable twinning nucleation sites, which is exactly what we have observed using in situ TEM. As such, stress concentration, strain accommodation capability, and crystal orientation render selectivity of twinning nucleation site, giving rise to the heterogeneity and probabilistic behaviors of twinning nucleation[123,150].

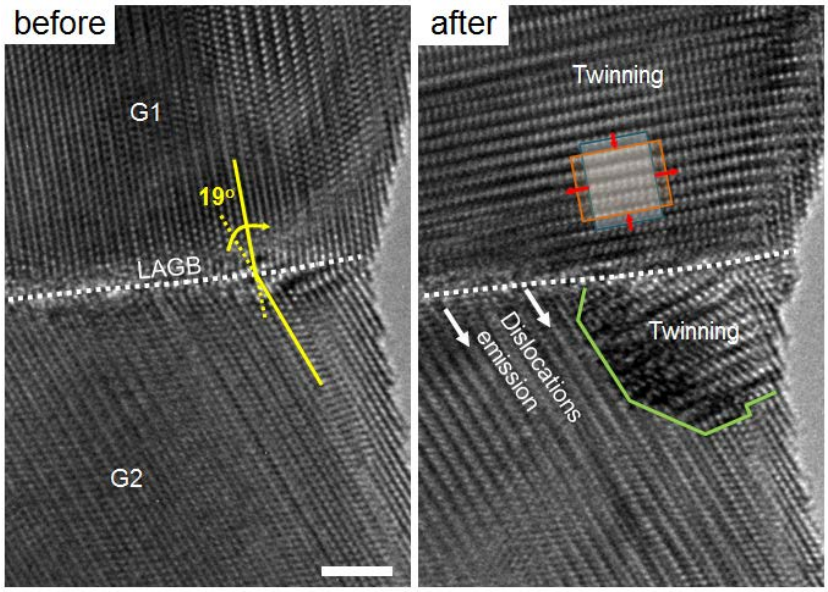

Figure 4.12 Strain accommodation mechanisms on a low angle grain boundary (LAGB), including dislocation emission (white arrows) and twinning (enclosed by green lines) in the lower grain (G2) to accommodate the strain generated on the grain boundary by twinning in the upper grain (G1, see schematic inset and red arrows). Scale bar, 2 nm.

Third, since the P→B transformation generated an orientation relation (of the matrix and the twin) that is ~4^{o} off the ideal mirror symmetry[108], strains were generated during the twinning nucleation process, giving rise to the lattice distortions in the twin and the matrix. As such, the mirror symmetry of an ideal {1 0 -1 2} twinning was absent during twinning nucleation; and the lattice distortion might provide the driving force for the detwinning of the twinning embryos (see Figure 4.1e-f).

4.4.2 P→B transformation-mediated twinning growth

As shown in Figure 4.6 and Figure 4.7, the {1 0 -1 2} twinning growth primarily proceeded by P→B transformation, the same process as that in twinning nucleation, which generated

essentially the same lattice correspondence as the {1 0 -1 2} twinning[107,109], except for a minor lattice rotation[108]. As such, above discussion on its relation to the non-Schmid effect, lack of mirror symmetry and predominant presence of B│P-type twin boundaries can also be extended to twinning growth and will not be repeated here.

Since the twinning growth was also mediated by P→B transformation, the discussion on its influences on the {1 0 -1 2} twinning nucleation should also apply to the {1 0 -1 2} twinning growth. First, the normal strains (e.g. tension on basal plane or compression on prismatic plane) should be able to prompt the twinning growth. As shown in Figure 4.13a, tension straining was applied on the basal plane of a Re nanocrystal which then deformed by the formation of a {1 0 -1 2} twinning. The twin boundary largely departed from the twinning plane (see Figure 4.13b); a feature that is directly resulted from the B→P transformation. Additionally, the twin boundary propagation seemed to have been blocked temporarily by dislocations in the parent crystal. It is readily comprehensible considering that the B→P transformation requires tensile strain on basal plane while compressive strain was supplied by the dislocation core (see white-circled region in Figure 4.13b) which biased the external stress and temporarily retarded the twinning growth. The effects of normal strains on the twinning growth via P→B and B→P transformations (see Figure 4.6 and Figure 4.13) also explains the non-Schmid effect of the {1 0 -1 2} twinning growth[90-92,94,95].

It should be noted that the dislocations did not stop the twinning growth (see 13~27s snapshots in Figure 4.13a). Since the twinning growth was shuffle-dominated involving no twinning dislocations, the twin boundary was not confined by the twinning planes but could take any form; thereby the twin boundary propagation could circumvent the barriers (e.g. dislocations and precipitations) and continue propagation with increasing straining. Particularly, with such

capability, the {1 0 -1 2} twinning growth can readily overtake the whole crystal or grain in a polycrystalline material which is exactly what have been observed in ex situ studies[22,58]. Second, twinning growth via P→B and B→P transformations incurred predominantly B│P-type twin boundaries and a grain rotation that slightly depart from the ideal twin. These facts satisfactorily explains the wide presence of B│P-type interfaces and the lack of mirror-symmetries in ex situ characterization of static twin boundaries of {1 0 -1 2} twinning[88].

Classically, twinning growth is believed to be dominated by shear and mechanistically through the shuffle-glide of twinning dislocations[50,70]. Here, the triumph of P→B and B→P transformations over twinning dislocations can be explained by the lack of sources for twinning dislocation nucleation. Due to a lack of proper pre-existing defects, the sources of twinning dislocations, such as matrix dislocations (see the Serra-Bacon mechanism)[41,79], coherent twin boundary[60,80,81,83], are limited in nanocrystals. Though, interfacial defects on incoherent B│P-type interfaces may transform into twinning dislocations at the disclination[84,85]. However, in our observation, CTB did not dominate the twinning growth in the most cases. Since surface can also provide nucleation sites for twinning dislocations, as discussed in the above section, the nanoscale sample size might have hindered the nucleation of twinning dislocation from surface. Note that our observation indicates that twinning dislocation mechanism does work in mediating twin boundary migration (see Figure 4.9). Therefore, it is reasonable to expect that in bulk samples where twinning dislocation sources are abundant twinning dislocation mechanism also plays dominant role in the {1 0 -1 2} twinning growth.

Considering the prevalent presence of B│P-type twin boundaries and the abnormal behaviors of {1 0 -1 2} twinning in bulk samples, it is reasonable to expect that P→B and B→P transformations-mediated {1 0 -1 2} twinning growth in bulk HCP metals. The strengthening of

materials through dislocations and precipitations will be in vine, since they cannot effectively pin the twin boundary propagation which can be in arbitrary shape as a result of the shuffle-dominated mechanism[43,88,104]. An effective way to pin down the {1 0 -1 2} twinning for improving strength of the HCP metal will be to use pre-deformation, and add in solution elements to pin down the CTB[13], or by alloying and increasing the energy of B|P-type twin boundaries and hence compelling the twinning to proceed by twinning dislocations on CTB.

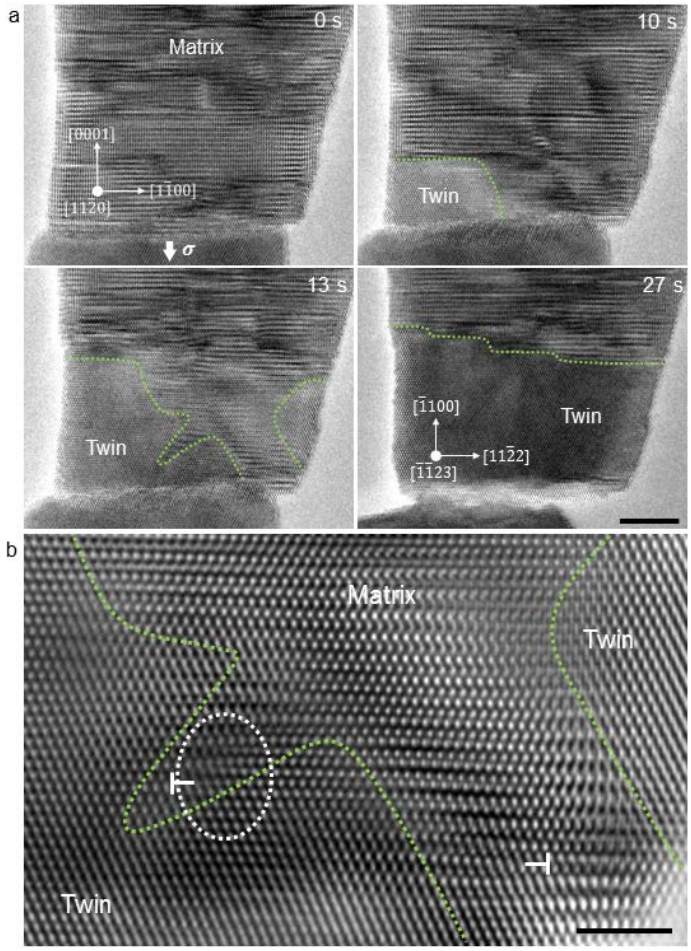

Figure 4.13 {1 0 -1 2} twinning in a defective Re crystal under [0 0 0 1]-oriented tension (a) and its interaction with matrix dislocations (b). The twin boundaries were indicated by green lines. Dislocations were indicated by white "⊥" signs. Scale bar in (a), 5 nm; scale bar in (b), 2 nm.

4.4.3 Detwinning of the {1 0 -1 2} twin

The discovery on the movement of twinning dislocations in Figure 4.9 directly proved the classical twinning dislocation mechanism of HCP metals; though, the process prevailed in the detwinning process rather than twinning formation. The underlying reason for the absence of twinning dislocation during twinning growth may be the small sample size and lack of specific defects that can be sources of twinning dislocations. The different dominant mechanisms for twinning and detwinning may hold the fundamental reason for the asymmetrical stress-strain hysteresis in fatigue tests[151].

The transformation from B│P-type interfaces to CTBs emphasizes the critical role of operando characterization in studying the twinning mechanisms in HCP metals. Based on observations of the statistic "twin embryo" after unloading, twinning nucleation is believed to proceed by spontaneous nucleation of multiple twinning dislocations from surfaces[46]. However, our observations reveal a totally different mechanism which should be more accurate picture due to following reasons. First, the sizes of the twin embryo we captured was much smaller than that reported in literatures, meaning that our observation represented a more incipient state of the twinning embryo. Second, in our observations (e.g. Figure 4.1), almost all twin embryos fully detwinned upon unloading. Therefore, the observed "twin embryos" in unloaded samples are likely detwinned structures. In lieu of the fact that the twin boundaries dramatically changed from B│P-type interfaces to CTB during detwinning, it is not surprising that the "twin embryos" in literature are predominately bounded by CTBs.

4.5 CONCLUSIONS

In this chapter, the {1 0 -1 2} twinning nucleation, growth and detwinning in HCP Re nanocrystals have been investigated. The results are the first operando study on the {1 0 -1 2} twinning and unambiguously reveal the {1 0 -1 2} twinning process in HCP metals.

Based on the observation, for all nucleation sites (including (0 0 0 1) surface, non-(0 0 0 1) surface, grain boundary, and dislocation core), the morphology of the twinning embryo and their dynamic behavior shared some similarities. First, all embryos were bounded by B│P and P│B interfaces. Second, the growth of all twin embryos was mediated by P→B and B→P transformations. Third, the lattices of twin embryos and nearby matrixes were distorted and shared no parallel twinning planes. In addition, no twinning dislocation was identified in all the twinning nucleation events. As such, the {1 0 -1 2} twinning growth was likely primarily mediated by P→B and B→P transformations; and the twin boundaries were primarily B│P-type interfaces which, upon detwinning, retreated to the coherent twin boundaries. The detwinning process was mediated by the synergy of classical ($\boldsymbol{b}_2$, h_2) twinning dislocations on the {1 0 -1 2} planes and the B→P transformation. The classical twinning dislocation mechanism does work for the {1 0 -1 2} twinning, but primarily in the detwinning and immediate reloading processes in our observations.

These results satisfactorily explain all the abnormalities of the {1 0 -1 2} twinning nucleation and growth including the non-Schmid effect, co-existence of CTB and B│P-type interfaces, lack of mirror symmetry, and weak interaction with dislocations in front of the twin tip. Due to the fact that P→B and B→P transformations only generate dilatational strains, the twinning nucleation and growth dominated by such transformation are essentially shuffle-dominated rather than shear-dominated.

Furthermore, based on the lattice correspondence of the {1 0 -1 2} twinning, the corresponding plane of the matrix prismatic plane is the twin basal plane, and the corresponding plane of the matrix basal is the twin prismatic[107]. And, the lattice correspondence established by P→B and B→P transformations gives planar correspondence between {1 0 -1 2} twinning planes in the matrix and "twin". Therefore, P→B and B→P transformations establish the same lattice correspondence as the ideal {1 0 -1 2} twinning, but via a totally different interfacial process in contrast to the shuffle-gliding of twinning dislocations on the twinning plane.

Classical twinning dislocation mechanism of twinning formation in HCP crystals originates from describing the twinning process as a homogeneous shear by Bilby and Crocker[18]. There is a silent assumption that the twinning has to be a one-step process enchanting on the coherent twin boundary. However, from the non-diffusional transformation point of view[105,152], non-diffusional transformation should be defined by the lattice correspondence it completes. Therefore, it is reasonable to conjecture that, as long as the transformation completes the lattice correspondence, twinning is not necessarily confined on the twinning plane; any interfacial process that conforms to the "target" lattice correspondence may be a potential transformation pathway. It should be noted that twinning via the "non-classical" twinning pathway (e.g. P→B and B→P transformations) deviates from the ideal matrix-twin orientation-relation. In twinning modes with relatively large twinning shears, the non-classical interfacial processes should be hard to activate. These hypotheses are further validated in the following chapters.

5.0 MARTENSITIC TRANSFORMATION MEIDATED TWINNING IN HCP CRYSTALS

5.1 INTRODUCTION

Martensitic transformations share lots of similarities with deformation twinning. In fact, due to the existence and random distribution of point defects, e.g. chemical disorder in solid solutions, ideal mirror symmetry of a twinning does not exist; and hence all twinning can be treated as martensitic transformations[19]. Both are important category of shear-driven solid-state transformations in materials. Both are widely used for tuning the properties of materials, e.g. steels, shape memory alloys, diamond-cubic silicon[27], β-titanium alloys and HCP alloys. Both are interfacial processes that are mediated by interfacial defects on the twin boundary (for twinning) or habit plane (for martensitic transformation)[105,153]; especially in multiple-lattice crystal structures, e.g. HCP metals, both processes are mediated by interfacial defects that carry both shear and atom shuffle[105]. Therefore, they are the same class of non-diffusional transformations[107,142], except that twinning does not change the structure of the parent crystal[105]. It has been found that martensitic transformation could mediate the twinning process[19,154].

Here, by deforming rhenium nanocrystals using state-of-the-art in situ TEM, we captured a novel martensitic transformation from HCP to FCC at atomic-resolution. The results uncovered

a new transformation twinning mechanism via an intermediate FCC phase, which, again, stood in contrast to the twinning dislocations mechanism[50,70,84,85].

Additionally, the mechanism of HCP→FCC transformation in literatures and this report were inter-related by using lattice correspondence analysis which further predicted more interfacial mechanisms for the HCP→FCC transformation. Surprisingly, the predictions were directly proved by using in situ TEM here. The findings demonstrate the multifunctional role of the FCC phase in the deformation of HCP crystals, and provide in-depth understanding to the fundamentals underneath case-dependent mechanisms of non-diffusional transformations.

5.2 PROCEDURE

The experimental procedures were generally the same as those described in Chapter 3.3. The orientations of the Re nanocrystals in this chapter were tuned such that the compression direction was along <1 -1 0 0> which strongly favored the {1 0 -1 2} twinning. And, the viewing direction was tuned to <1 1 -2 0> axis for HRTEM investigation of the twinning process; these viewing directions put the twinning plane edge-on so that HRTEM observation could be made on the shear plane. External shear on the matrix prismatic planes was applied by slightly tilting the crystal along the viewing direction, such that the compression direction was a few degrees off the <1 -1 0 0> direction giving a non-trivial resolved shear stress on the prismatic planes (or the B | P interface). The shear component of external loading prompted the martensitic transformation from HCP to FCC. The strain rate was controlled to be ~10^{-3} s^{-1} in all tests.

5.3 RESULTS

5.3.1 In situ TEM observation of HCP→FCC martensitic transformation

Figure 5.1 showed the HCP to FCC transformation in a Re nanopillar under <1 -1 0 0>-oriented compression. After initial elastic straining, {1 0 -1 2} twinning started by transformation of matrix prismatic planes in to twin basal planes, i.e. P→B transformation; and a FCC region was identified at the intersection of the P│B interface and surface (Figure 5.1a). With increasing strain, the FCC region expanded through layer-by-layer formation and propagation of {1 1 1} planes from the surface. During this process, single-layer interfacial defects[74,105] migrated and contemporarily transformed the HCP prismatic planes into FCC {1 1 1} planes (Figure 5.1b). In contrast to previous reports on HCP to FCC transformation[155-160], this process established a novel orientation relation between the FCC phase and the HCP matrix, i.e. {1 -1 0 0}//{1 1 1}, [0 0 0 1]//<1 1 -2>, <1 1 -2 0>//<1 -1 0>. Moreover, the transformation was martensitic, generating a shear strain of 0.36 as manifested by the surface inclination angle of ~20^{o}. As shown in the atomic resolution TEM snapshot in Figure 5.2, the single-layer interfacial defect carried atomic shuffles that transformed corrugated prismatic plane into flat {1 1 1} plane (cyan lines in Figure 5.2), and magnitude of the Burgers vector was ~0.8Å as shown by the circuit analysis[146]. It should be noted that the observed martensitic transformation from HCP to FCC was reversible upon reverse loading (see Figure 5.3).

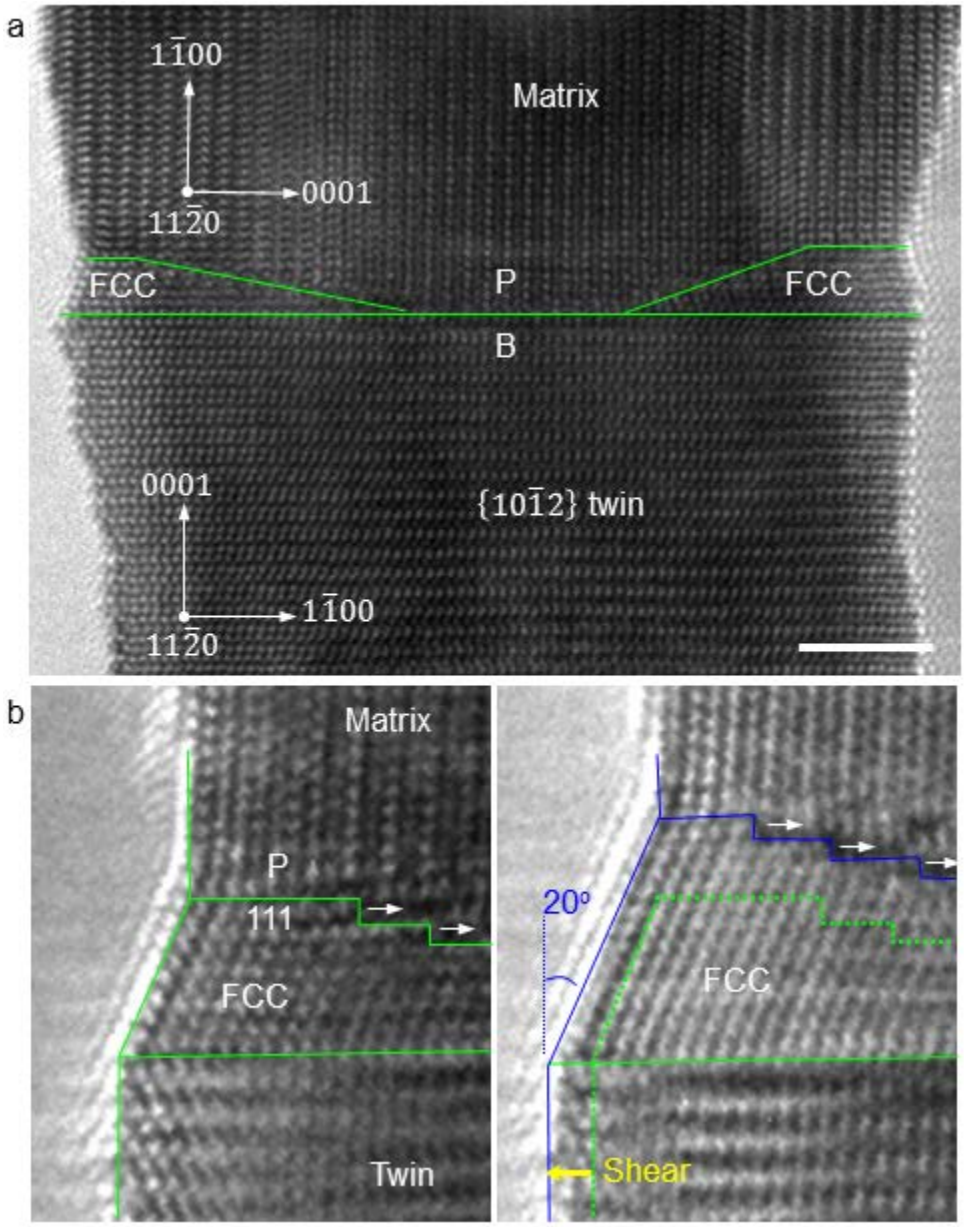

Figure 5.1 HCP→FCC martensitic transformation in a Re nanocrystal under <1 -1 0 0>-oriented compression. (a) HRTEM image of the FCC phase (enclosed in green lines) on the {1 0 -1 2} twin boundary. Nucleation of the FCC phase started from the intersection of the surface and the P│B interface. (b) Sequential TEM snapshots showing growth of the FCC phase by emission of interfacial defects from the surface and propagation (white arrows). Green and blue lines indicate the FCC│HCP phase boundaries. Scale bar in (a), 2 nm.

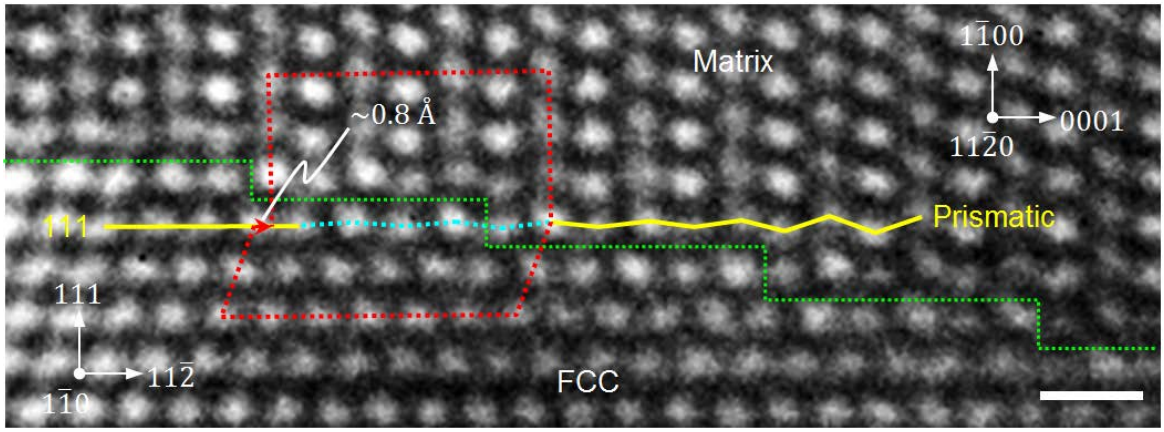

Figure 5.2 Enlarged atomic resolution TEM image showing single-layer interfacial defect that mediated the HCP→FCC transformation. The single-layer interfacial defect transforms HCP prismatic planes into FCC {1 1 1} planes. Green lines indicate the FCC | HCP phase boundary. Cyan lines demonstrate atom shuffles that flatten the corrugated prismatic plane. Circuit analysis (red circle and arrow) highlights the shear carried by each interfacial defect. Scale bar, 500 pm.

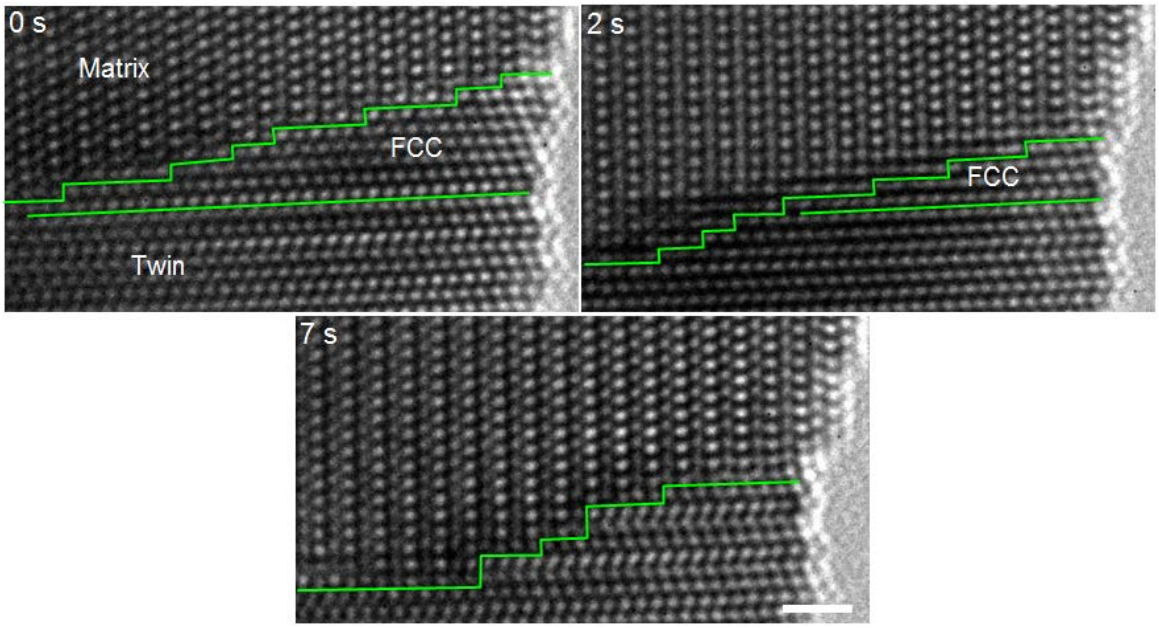

Figure 5.3 Sequential atomic resolution TEM image showing that the FCC phase reverses back to HCP (matrix) structure under reverse loading. Scale bar, 1 nm.

5.3.2 In situ TEM observation of FCC phase mediated {1 0 -1 2} twinning

Remarkably, in further compression, the FCC phase transformed to HCP which was in twin orientation with the original HCP matrix, indicating that the FCC phase was an intermediate phase in the {1 0 -1 2} twinning process (Figure 5.4). During this process, the FCC {1 1 1} planes transformed into HCP basal planes, establishing an orientation relation of {1 1 1}//(0 0 0 1) and <1 1 -2>//<1 -1 0 0>.

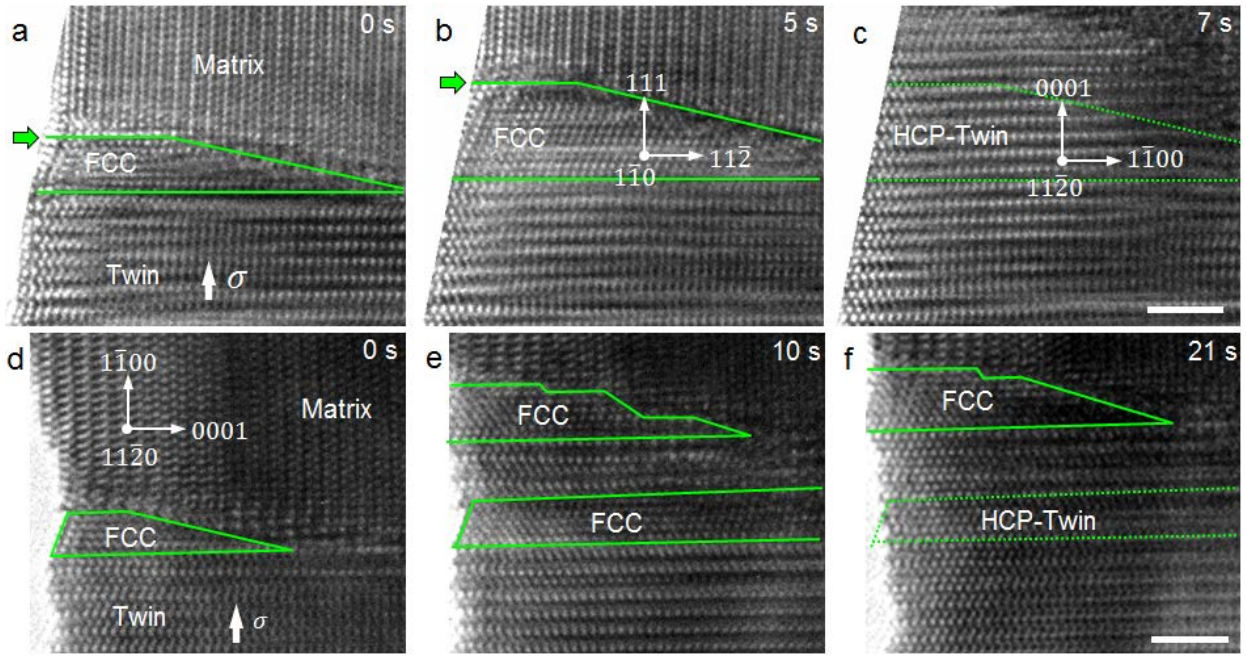

Figure 5.4 Sequential HRTEM snapshots showing FCC→HCP transformation in further compression, indicating that the FCC phase was an intermediate step in the {1 0 -1 2} twinning. Green lines denote the region of the FCC phase. Scale bars in (c, f), 2 nm.

To demonstrate the sequential $HCP_{maxtrix}$→FCC→HCP_{twin} transformations in three dimensions, we schematically illustrated the transformations using a HCP unit-cell. As shown in

Figure 5.5a&c, the corrugated prismatic planes (P1~P3) in the unit-cell of HCP matrix were flattened by atomic shuffles and the in-plane structure became that of a FCC {1 1 1}. Then, as shown in Figure 5.5b&d, a homogeneous shear on every prismatic plane changed the stacking sequence from AB'AB'AB' into ABCABC stacking of the FCC {1 1 1} planes. As such, the shear should be along the [0 0 0 1] direction of the matrix with a magnitude of ~0.3, which was fairly consistent with the experimental observation in Figure 5.2.

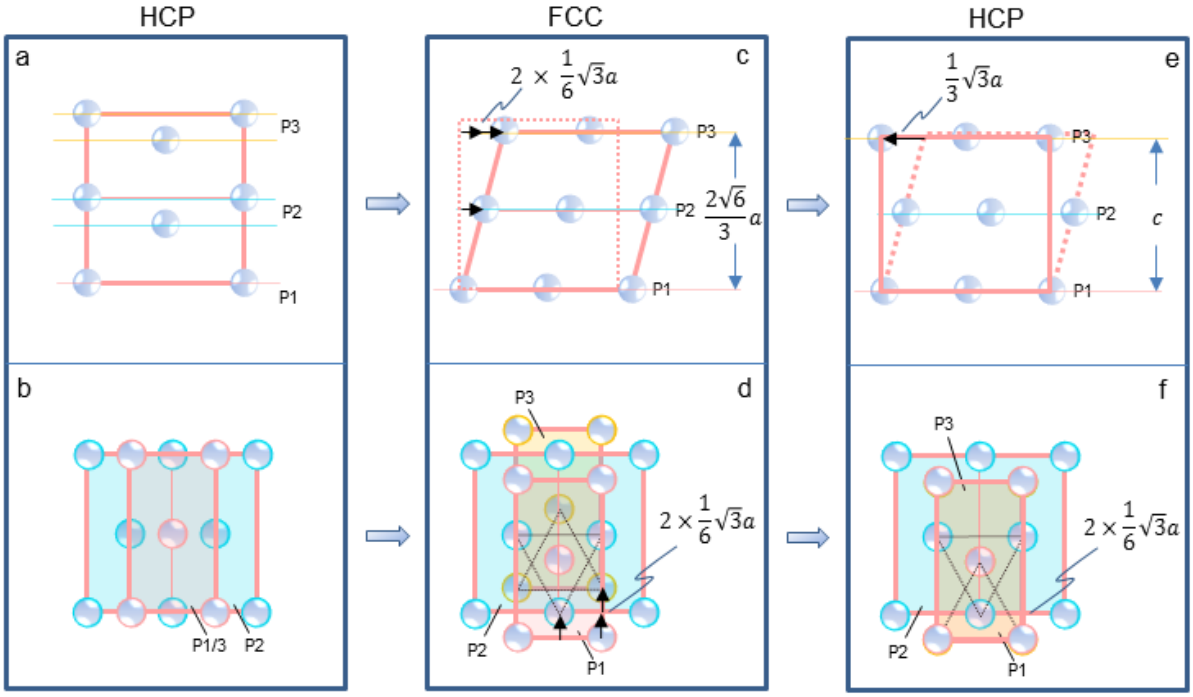

Figure 5.5 Schematic image of HCP_{matrix}→FCC→HCP_{twin} transformations via P→{1 1 1}→B, viewing along <1 1 -2 0> direction (a, c, e) and <1 -1 0 0> direction (b, d, f).

5.4 DISCUSSION

5.4.1 The uniqueness of observed HCP→FCC martensitic transformation

Based on crystallographic analysis, it is generally believed that martensitic transformation are mediated by interfacial defects that shear and shuffle matrix atoms into their corresponding positions in the martensite[105,161]. Even though static interfacial defects on martensitic phase boundaries have been imaged, it remains questionable whether these defects are able to move and dominate the transformation[104]. The in situ observations here (e.g. Figure 5.1) provide unprecedented evidence that martensitic transformation was indeed mediated by shuffle-gliding of interfacial defects.

The martensitic transformation from HCP to FCC in Figure 5.1 is novel and totally different from those reported in literatures. To date, two orientation relation of HCP→FCC transformations have been reported in HCP metals[155,156]. The most common mechanism corresponds to an orientation relation of (0 0 0 1)//{1 1 1}, <1 -1 0 0>//<1 1 2>, <1 1 -2 0>//<1 1 0>; experimental evidences suggest that such transformation is mediated by Shockley partial dislocations gliding on alternative basal planes, transforming the ABABAB stacking of HCP basal planes into ABCABC stacking of FCC {1 1 1} planes[156,159,160,162]. It is recently found that such orientation relation can also be established by mixed partial dislocations dissociated from both screw and 60^{o} <***a***>-type dislocations on HCP basal planes[157]. The other HCP→FCC orientation relation is {1 -1 0 0}//{1 -1 0}, [0 0 0 1]//<0 0 2>, <1 1 -2 0>//<1 1 0>. Simulations suggest that it proceeds by shear-shuffle or pure-shuffle of HCP prismatic planes into FCC {0 1 1} planes via two-layer or four-layer interfacial defects[155,158]. In contrast, the results here

demonstrate an unique orientation relation of {1 -1 0 0}//{1 1 1}, [0 0 0 1]//<1 1 -2>, <1 1 -2 0>//<1 -1 0> (see Figure 5.2), manifesting a totally new transformation mechanism.

5.4.2 Role of the FCC phase in HCP twinning

The comparison of Gibbs free energies of HCP and FCC phase is critically influenced by the stress state[163]. In the HCP→FCC transformation process, the stress state at the intersection of the surface and the B│P interface could temporarily favor the HCP→FCC transformation. As shown in Figure 5.1, the FCC transformation happened in the matrix right next to the twin boundary where the compressive stress should be lower that needed for twinning. Compared to twinning, the HCP→FCC transformation should generate smaller compressive strain (-0.05 vs. -0.07) along the <***c***> axis, therefore the compressive strain field in the matrix nearby the twin boundary favored the HCP→FCC transformation.

Besides, due to the intrinsic packing-density difference between the basal and prismatic planes, mismatch (see Figure 5.6) and presumably threading dislocations[43] might have been created on the P│B interface. Presumably, driven by imaging force from the surface, these threading dislocations near the surface glided along the P│B interface and annihilated on the surface, providing a shear strain that drove the formation of FCC phase. In addition, the external shear stress due to the titled compression could also provide the driving shear for the HCP→FCC transformation (see Figure 5.4a-c). Compared with twinning, the HCP→FCC transformation could generate larger shear strain (~0.3 vs. 0) on the P│B interface, and hence effectively mediated the internal or external shear strains on the P│B interfaces.

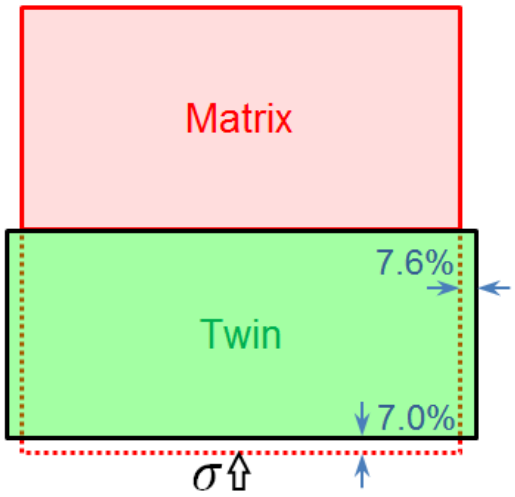

Figure 5.6 Strain incompatibility on the P│B interface as a result of {1 0 -1 2} twinning mediated by P→B transformation

Besides offering more slip modes and interfaces to impede dislocation motion, the FCC phase provided several unique contributions to the mechanical behaviors of HCP metals. First, as shown in Figure 5.5, this transformation could mediate normal strain along <***c***> axis which was particularly valuable to the ductility of HCP metals[1]. Second, it works cooperatively with the {1 0 -1 2} twinning by mediating the external shear strain on the B│P-type twin boundaries. And, in further compression, it could transform back to HCP structure through, presumably gliding of partial dislocations on every other {1 1 1} planes[156,162]; thus the FCC phase acted as an intermediate step of P→B transformation and hence the {1 0 -1 2} twinning.

5.4.3 More on HCP↔FCC phase transformation

In the following, the HCP→FCC transformation mechanisms in literatures and this study were co-related, and more interfacial mechanisms for HCP→FCC transformation were predicted with

one more successfully validated here. Martensitic transformations in crystals are normally mediated by interfacial defects on the phase boundaries; the shuffle-gliding of the interfacial defects transform one plane in the matrix into the corresponding plane in the martensite (or twin)[19,74,164]. As hinted by the findings in {1 0 -1 2} twinning, a transformation is not necessarily mediated by a unique interfacial process; any interfacial processes that conforms to and establishes the "target" lattice correspondence could offer a potential transformation pathway. The activation of these possible mechanisms seemed to be associated with factors including small shear and simple shuffle[18]. In other words, corresponding planes gave a superset of transformation pathways that required further verification.

To achieve small shear, planes involving in the interfacial process should have decently large *d*-spacing (or higher in-plane packing density); in other words, these planes should have low miller index. Referring to a well-known mechanism of HCP→FCC transformation wherein the HCP (0 0 0 1) becomes the FCC {1 1 1} (see plane ABC in Figure 5.7), the corresponding planes for all other {1 1 1} planes in the Thompson tetrahedral can be found. When ABCA stacking of FCC {1 1 1} became ABAB stacking of HCP (0 0 0 1), the green plane in Figure 5.7a has to shear in one of three alternative ways (see pink arrows in Figure 5.7b); each way of shear results in a unique corresponding plane for plane BCD in Figure 5.7a—BCD_1, BCD_2 and BCD_3[152]. Note that the three alternative shear pathways correspond to the same HCP lattices (Figure 5.7c). Plane BCD_1 and BCD_2 are the same {0 1 -1 1} plane, and plane BCD_3 is the prismatic plane. The corresponding planes for all other {1 1 1} planes in the Thompson tetrahedral (i.e. ACD and ABD in Figure 5.7a) can be found in the same way; and the results show that the corresponding planes for a FCC {1 1 1} can only be (0 0 0 1), {1 -1 0 0} or {1 -1 0 1}. Similar analysis can also be applied to identify corresponding planes for the other low-index

planes in FCC, e.g. {1 1 0}; results indicated that low-index corresponding planes for a FCC {1 1 0} are HCP {1 1 -2 0} or {1 -1 0 0}.

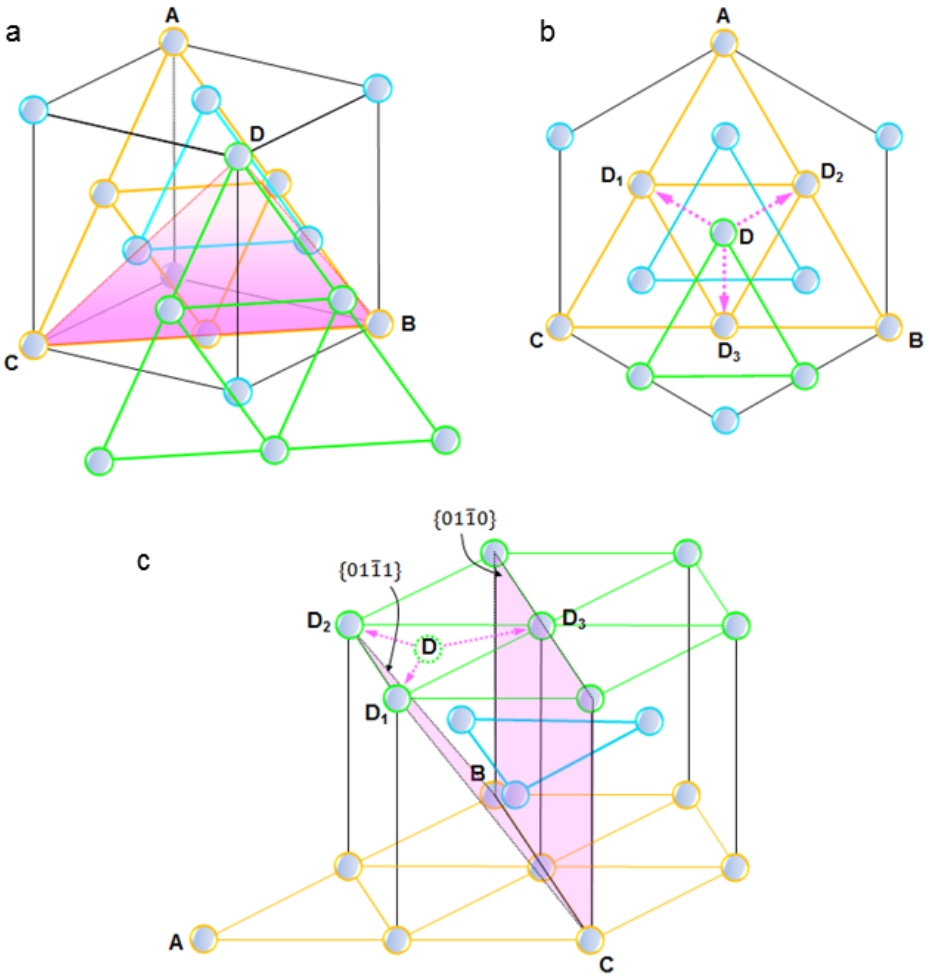

Figure 5.7 Topological analysis of lattice correspondences between FCC and HCP structures. (a) Unit-cell of a FCC lattice. The {1 1 1} planes are color-coded in yellow, cyan and green, respectively, to differentiate the ABCABC stacking. (b) Projection view of the unit-cell along the [1 1 1] direction. Pink arrows indicate possible shear directions of the green plane to achieve the FCC to HCP transformation. (c) Unit-cell of a HCP lattice. The FCC {1 1 1} plane (BCD) becomes the HCP {0 1 -1 0} or {0 1 -1 1} plane after the transformation.

HCP↔FCC transformations through interfacial processes of $(0\ 0\ 0\ 1)_{hcp}\rightarrow\{1\ 1\ 1\}_{fcc}$ [156,157,159,160] and $\{1\ -1\ 0\ 0\}_{hcp}\rightarrow\{1\ 1\ 0\}_{fcc}$ [155,158] have been widely reported. Interestingly, the in situ investigation here unprecedentedly verified transformations following the other two interfacial processes. Observations in Figure 5.1 and Figure 5.2 demonstrated the HCP→FCC transformations through $\{1\ -1\ 0\ 0\}_{hcp}\rightarrow\{1\ 1\ 1\}_{fcc}$. And, observations in Figure 5.8 and Figure 5.9 demonstrated the HCP→FCC transformation through $\{1\ -1\ 0\ 1\}_{hcp}\rightarrow\{1\ 1\ 1\}_{fcc}$.

The Re nanocrystal in Figure 5.8 was under {1 -1 0 0}-oriented compression. The deformation was primarily dominated by the P→B transformation (i.e. {1 0 -1 2} twinning) and $\{1\ -1\ 0\ 0\}_{hcp}\rightarrow\{1\ 1\ 1\}_{fcc}$ transformation (i.e. HCP→FCC phase transformation). A series of transformations took place in the upper-left region of the nanocrystal (see the boxed region in Figure 5.8b). Microstructure evolution of the very region was shown in the sequential HRTEM snapshots in Figure 5.8c. The HCP matrix transformed into a FCC structure at 43s (see Figure 5.8c). The FCC {1 1 1} layers of FCC were emitted from the surface and expanded laterally into the HCP matrix by transforming the HCP (-1 1 0 1) planes right in front of each FCC {1 1 1}; and the surface facet of HCP (-1 0 1 1) transformed into the other {1 1 1} plane of FCC (see Figure 5.9). This observation vividly demonstrates a novel interfacial process of $\{1\ -1\ 0\ 1\}_{hcp}\rightarrow\{1\ 1\ 1\}_{fcc}$ which establishes a unique orientation relation between HCP and FCC lattices— {-1 1 0 1}//{1 1 1}, <2 -1 -1 3>//<1 -1 0>, <-1 -2 3 1>//<1 1 -2>.

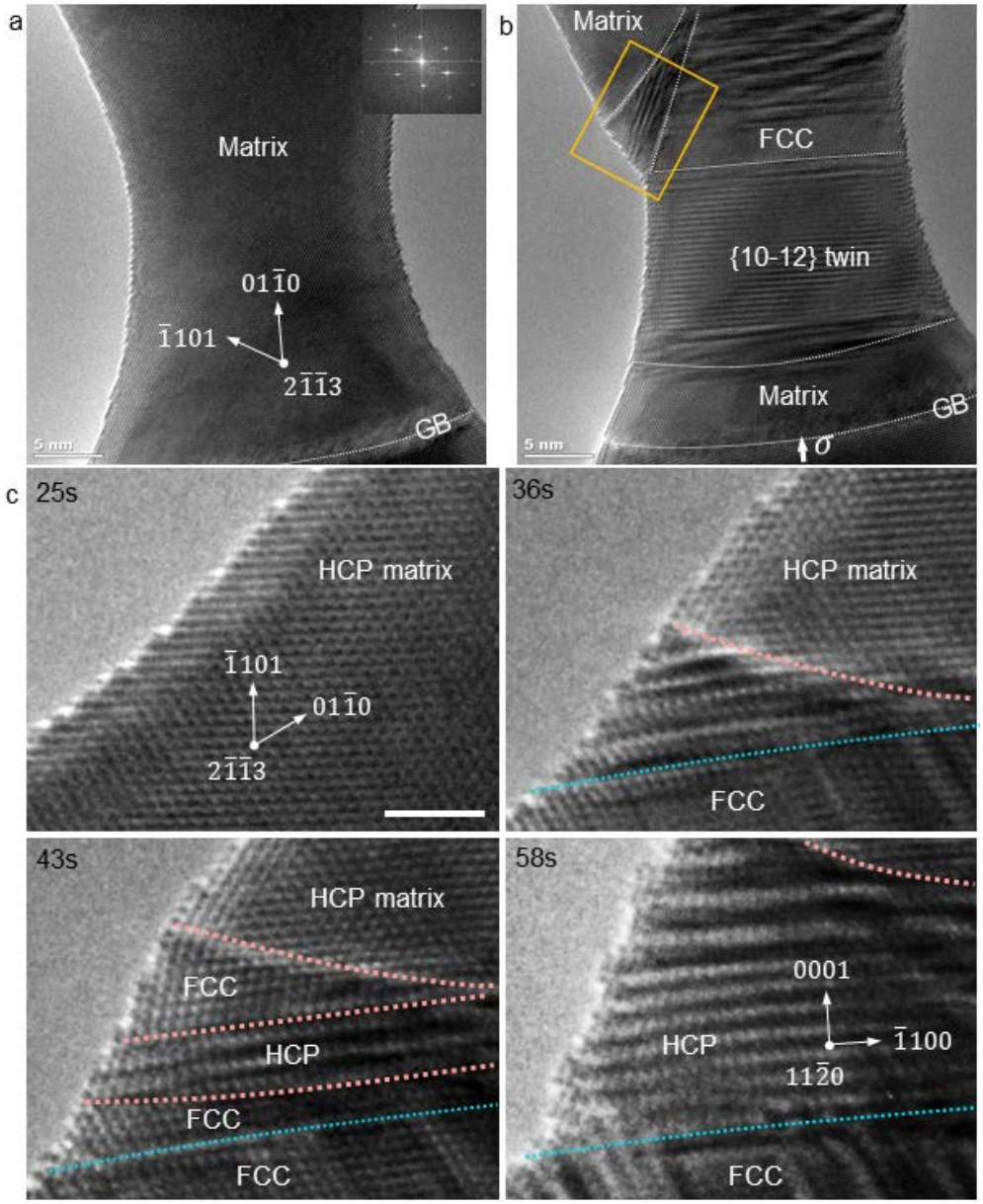

Figure 5.8 Grain rotation assisted by HCP→FCC phase transformation. (a-b) Sequential HRTEM images of a Re crystal under <1 -1 00>-oriented compression. Inset in (a) is the FFT of the HRTEM image. White dash lines indicate grain boundary, twin boundary and phase boundaries formed during deformation. (c) Sequential HRTEM snapshots showing the microstructure evolution of the boxed region in (b). The region went through a grain rotation in the period, mediating by sequential transformations from HCP→FCC→HCP. Scale bar in (c), 2 nm.

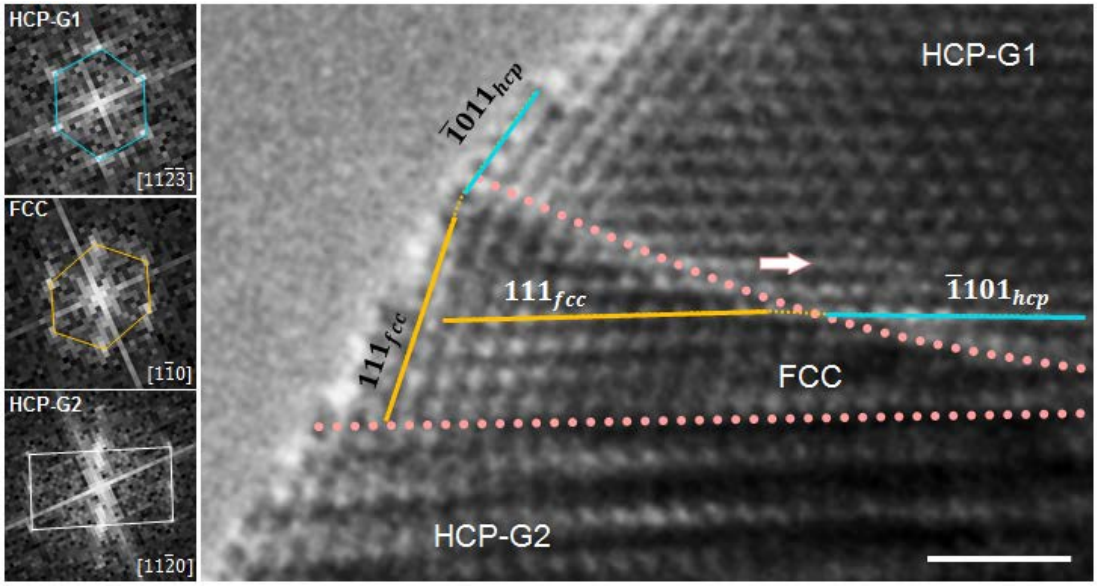

Figure 5.9 Enlarged HRTEM image of the FCC│HCP phase boundary (pink lines) in Figure 5.8b, demonstrating the unique interfacial process wherein HCP (-1 1 0 1) planes transform to FCC {1 1 1} planes. Insets on the left were FFTs of the HCP matrix (HCP-G1), FCC phase, and the HCP grain transformed from the FCC phase (HCP-G2). Solid lines are corresponding planes of twin (in yellow color) and matrix (in cyan color). Block arrows indicate the migration direction of the phase boundary. Scale bar, 1 nm.

The multiple transformation pathways between FCC and HCP leads to the attendant multifunction of the FCC phase in the deformation of HCP crystals. For example, as shown in Figure 5.4, the FCC could act as an intermediate phase in the {1 0 -1 2} twinning process of the HCP matrix through the sequential $\{1\ -1\ 0\ 0\}_{hcp}\rightarrow\{1\ 1\ 1\}_{fcc}\rightarrow(0\ 0\ 0\ 1)_{hcp}$ transformations; moreover, the FCC phase could assist grain rotation of the HCP matrix through sequential $\{1\ -1\ 0\ 1\}_{hcp}\rightarrow\{1\ 1\ 1\}_{fcc}\rightarrow(0\ 0\ 0\ 1)_{hcp}$ transformations (see 43s & 58s snapshots in Figure 5.8c). Therefore, prompting the HCP↔FCC transformation can be useful for the grain pulverization of HCP metals, generating a microstructure with duel-phase (HCP and FCC) and fine grain sizes which may lead to combined increases of strength and ductility[7].

5.5 CONCLUSIONS

Through in situ atomic-resolution TEM, a novel martensitic transformation from HCP to FCC was revealed, which acted as an intermediate step in the {1 0 -1 2} twinning process. Direct evidences were captured for the interfacial defects mediating martensitic transformation. The sequential HCP→FCC→HCP transformation presents a novel pathway of deformation twinning, and may explain the wide existence of FCC domains in the {1 0 -1 2} twins of HCP metals.

The underlying principle in the HCP→FCC transformation mechanisms in this investigation and literatures was discussed. New transformation mechanisms were predicted and directly testified by using in situ TEM. The in situ observations further revealed that the facile transformation pathways between HCP and FCC gave in a multifunctional role of the FCC structure in the deformation of HCP crystals.

6.0 IN SITU TEM INVESTIGATION OF {1 1 -2 1} TWINNING

6.1 INTRODUCTION

The twinning dislocation mechanism has been widely accepted for twinning formation in HCP crystals[19]. However, the in situ results on {1 0 -1 2} twinning (see Section 4.5) revealed a different mechanism wherein the dominant interfacial process that mediated the twinning formation was not on the twinning plane. As shown in the discussion, the abnormal twinning pathway may be attributed to the extremely low shear of {1 0 -1 2} twinning mode[101]. Therefore, it is intriguing and promising to verify the dominant role of twinning dislocation mechanisms in twinning modes with large twinning shear.

{1 1 -2 1} twinning widely exists in Ti[139], Zr[68], Co[165] and particularly Re[123]. Classical twinning theories predict that the K_2 plane for the {1 1 -2 1} twinning is {0 0 0 2}; and corresponding twinning shear is $1/\gamma$ (~0.62 for pure Re)[19,51,166]. It should be noted that the abnormal twinning shear[68] and associated mechanisms[72,166] regarding {1 1 -2 1} twinning in Zr are far beyond the findings on Re and will not be covered here. Since the {1 1 -2 1} twinning mode has a much larger twinning shear (theoretically the largest among all prevalent twinning modes[19]), interfacial processes other than the twinning dislocation mechanism would result in large deviation from the orientation relation of an ideal {1 1 -2 1} twinning which hence is most likely dominated by twinning dislocation mechanism.

Based on computational simulations and ex situ experiments, it is generally agreed that the {1 1 -2 1} twinning is mediated by twinning dislocations on the {1 1 -2 1} twinning plane[59]. However, it remains debatable as for the type of dominant twinning dislocations. Classically, twinning dislocation on {1 1 -2 1} twinning plane should be a single-layer twinning dislocation (or elementary twinning dislocation) with a step height *h* of one {1 1 -2 1} plane[19,73]. Though, molecular dynamics simulations by Serra *et al.* showed that such dislocation was not stable and would decompose into two dislocations with step heights of 1/2{1 1 -2 1} plane[51,62]. By tracking the atomic movement during the twinning process, their recent simulations further revealed that the twin boundaries adjoining by the ($\boldsymbol{b}_{1/2}$, $h_{1/2}$) were energetically degenerated and hence the twinning dislocation was stable; in addition, the core of the ($\boldsymbol{b}_{1/2}$, $h_{1/2}$) twinning dislocation was highly expanded giving rise to its good mobility[51]. However, direct experimental evidences to the twinning dislocations and their mobility are currently lacking.

Additionally, the atomic shuffles in the {1 1 -2 1} twinning remain elusive. Earlier molecular dynamics simulations concluded that shuffle normal to the shear plane was not necessary for this twinning mode[62,167]. However, simulations revealed that the twinning shear changed the stacking sequence of the basal planes, and atomic shuffles were necessary to re-establish the stacking of basal planes in the twin[111,168]. 4 alternative shuffle mechanisms have been suggested[111]. Unfortunately, due to the difficulty in detecting the angstrom-scale atomic movement in the complex HCP structure, the problem remains inconclusive.

Here, through state-of-the-art in situ TEM, the {1 1 -2 1} twinning process was directly captured at atomic resolution. The results unambiguous unravel above questions, especially the mystery on dominant twinning dislocations and atomic shuffles.

6.2 PROCEDURE

The prevalent deformation mode of bulk Re was characterized by using ex situ TEM observation on the microstructure of a cold-rolled Re plate. The Re plate was initially recrystallized at 960^{o}C in inert argon atmosphere for 4 hours to minimize pre-existing defects. Then, it was manually cold-rolled at room temperature and thinned by mechanical polishing into ~50 μm thick foil. The Re foil was cut into round disks (~3mm in diameter) by using a punching machine, and then milled to electron transparency by using precision Ar ion polishing system. The sample was loaded on a conventional double-tilt TEM holder and characterized under low magnification and HRTEM modes.

In situ experimental procedures were basically the same as those described in Section 3.3. For in situ HRTEM observations, the orientations of the Re nanocrystals in this study were tuned such that the {1 1 -2 1} twinning plane was edge-on. Tension tests were made along a direction that was a few degrees off the [0 0 0 1] direction of the sample; this loading orientation rendered a high Schmid factor for the {1 1 -2 1} twinning mode which was in competition with the basal slip. Compression tests were made along a direction that was a few degrees tilt about the [2 -1 -1 3] direction with respect to [0 1 -1 0] direction. It should be noted that this loading direction should favor the {1 0 -1 2} twinning, the activation of {1 1 -2 1} twinning might be attributed to the possible misaligned compression. The twinning processes were characterized on two viewing directions— <1 -1 0 0> direction (i.e. normal to the shear plane) and <1 1 -2 -3> direction; the <1 1 -2 -3> view of the twinning process made it possible to capture the atomic shuffles along the <1 -1 0 0> direction. The strain rate was controlled to be ~10^{-3} s^{-1} in all tests.

6.3 RESULTS AND DISCUSSION

6.3.1 Ex situ observation of the {1 1 -2 1} twinning in bulk Re

Ex situ TEM characterization of deformation twinning in cold-rolled bulk HCP pure Re was shown Figure 6.1. Low magnification TEM image (see Figure 6.1a) revealed massive twinning bands in the deformed sample. The viewing direction of the deformed grain was adjusted to the <***c***> axis of the matrix crystal, such that all 3 orientations of {1 1 -2 1} twinning bands could be observed. These twinning bands were parallel to the edge of the same family of crystal planes, i.e. the {1 1 -2 1}. Select area electron diffraction pattern and HRTEM lattice image of the twin band (see Figure 6.1b-c) showed the same orientation relation that was consistent with the theoretical orientation relation of the matrix and a {1 1 -2 1} twin, further proving that the observed twinning belonged to the {1 1 -2 1} twinning mode.

Schematic image in Figure 6.1d illustrates the orientation relation of the matrix and the twin unit cells. When the inclined (2 -1 -1 1) twinning planes in the matrix and the twin are aligned, the matrix <***c***> direction should be “nearly” parallel to the [2 -1 -1 3] direction of the twin, and the matrix [2 -1 -1 0] direction should be parallel to the twin [2 -1 -1 2] direction; such orientation relation is exactly the same as those shown in Figure 6.1b-c. These observations unambiguously demonstrated that the {1 1 -2 1} twinning was a dominant twinning mode in bulk HCP Re, which was consistent with previous report[123].

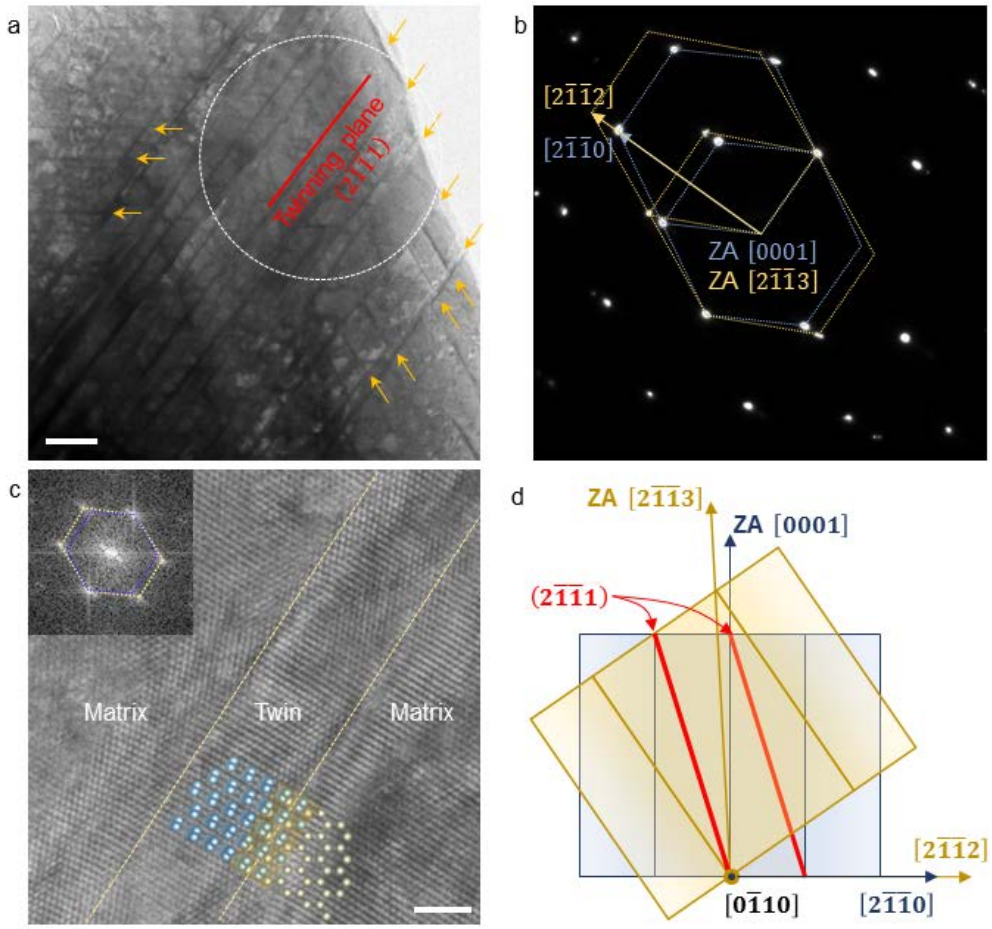

Figure 6.1 Prevalent {1 1 -2 1} twinning in bulk Re. (a) Low magnification TEM image showing massive {1 1 -2 1} twins (yellow arrows). (b) Selected area diffraction pattern from the circled region in (a). The blue and yellow hexagons mark the reciprocal lattice of matrix and twin, respectively. (c) HRTEM image of a {1 1 -2 1} twin, viewing along the [0 0 0 1] direction of the matrix crystal. The (2 -1 -1 1) twinning plane is inclined ~17.3^{o} to the viewing direction. Inset is FFT of the HRTEM image. (d) Schematics of the matrix cell (in blue) and twin cell (in yellow), with an orientation relation corresponding to that in (b). Red lines indicate the invariant {1 1 -2 1} twinning planes. Scale bar in (a), 500 nm; scale bar in (c), 2 nm.

6.3.2 In situ low-magnification observation of the {1 1 -2 1} twinning

The Re nanocrystals for the in situ low magnification characterization of the {1 1 -2 1} twinning process were shown in Figure 6.2. In situ compression tests was carried out using a bi-crystal which was synthesized by welding two Re nanocrystals together using an electric pulse (Figure 6.3a). As shown in Figure 6.2, the upper crystal had an angle of ~10^{o} with respect to the lower crystal about the viewing direction. As such, the bi-crystal had a low angle tilt "grain boundary", providing the strain compatibility condition for easy twinning formation.

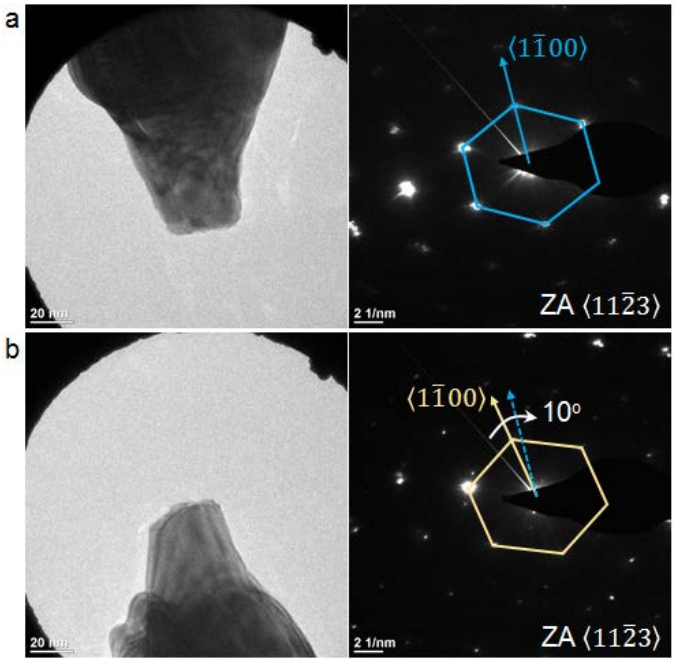

Figure 6.2 TEM images and corresponding select area diffraction patterns of the upper (a) and lower (b) crystals. The upper and lower crystals had the same zone axis (ZA) and a mutual rotation of ~10^{o} about the ZA.

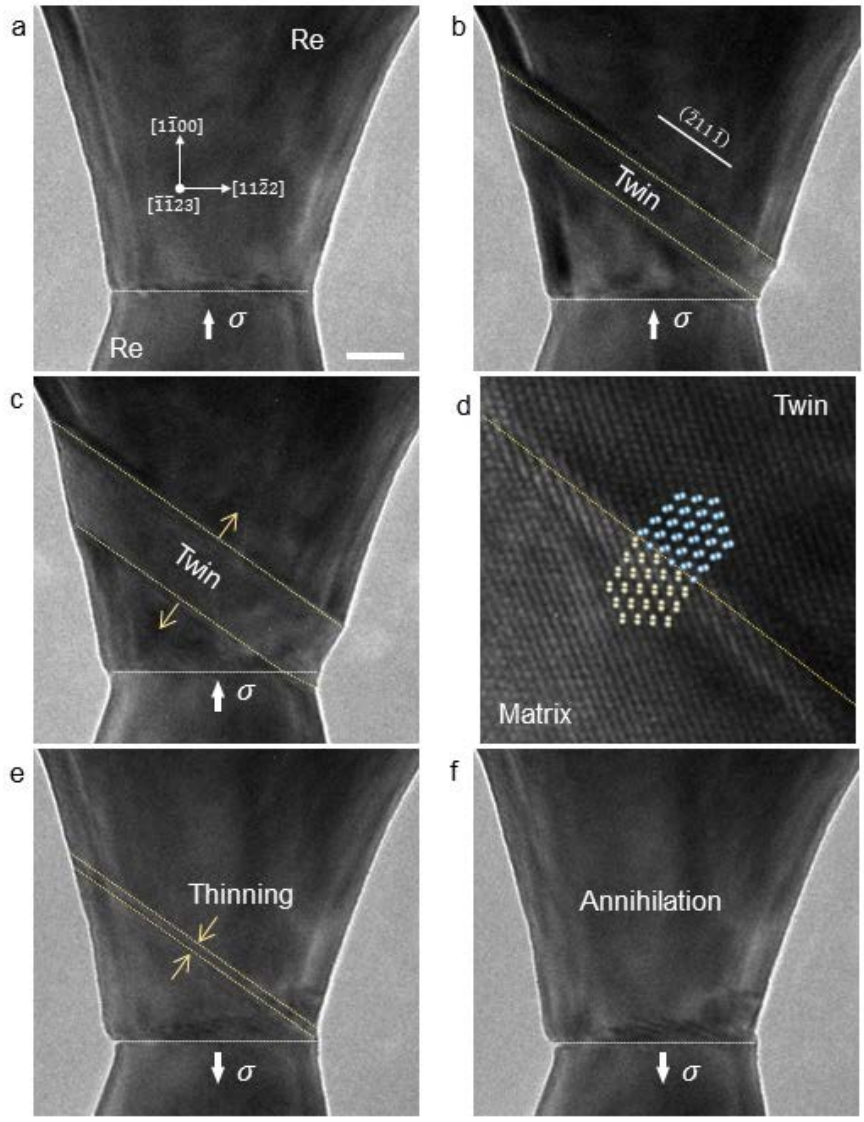

Figure 6.3 Sequential in situ low magnification TEM snapshots showing the {1 1 -2 1} twinning (a-c) and detwinning (e-f) processes in Re bi-crystal. (d) HRTEM image of the {1 1 -2 1} twin boundary (indicated by yellow dash lines). Inset in (d) shows the atomic model of the {1 1 -2 1} twin boundary under current viewing direction. White dash lines mark the grain boundary of the bi-crystal. Scale bar in (a), 10 nm.

Compression was applied roughly along the [5 -6 1 -1] direction of the upper crystal which had a diameter of ~35nm and was free of defects initially. Upon compression, the bi-

crystal deformed elastically; and then plastic deformation started with an immediate twinning nucleation from the side surface of the crystal (Figure 6.3b). The twin nucleus penetrated through the whole crystal upon nucleation. Subsequent compression was mediated by the twinning growth, i.e. thickening of the twin band (Figure 6.3c). The twin boundaries apparently remained parallel to the (-2 1 1 -1) twinning plane, and the twinning penetrated through the grain boundary into the lower crystal (see Figure 6.3c). Lattice image of the twin boundary in Figure 6.3d shows a consistent structure with the model of an ideal {1 1 -2 1} twin boundary, further proving that the {1 1 -2 1} twinning mode. Upon unloading and/or reverse loading, the twin band gradual thinned and eventually disappeared (Figure 6.3e-f), demonstrating that the {1 1 -2 1} twinning was totally reversible. It should be noted that there were cases when part of the {1 1 -2 1} twin remained even after the bi-crystal fractured at the grain boundary, meaning that the {1 1 -2 1} twinning was not pseudo-elastic.

The {1 1 -2 1} twinning nucleation process was too fast to capture with current TEM. The nucleus penetrated the whole cross-section of the crystal within 0.3s; and no strain accommodation mechanism was observed at the "twin tip"[165]. In addition, the critical stress for the twinning nucleation should be larger than that required for the twinning growth; since the deformation was primarily dominated by the twinning growth of a single twin band. Though, the easy nucleation of the twinning dislocations during twinning growth might be attributed to the stress concentration on the surface steps generated by the twin.

6.3.3 In situ atomic-resolution observation of {1 1 -2 1} twinning growth

To reveal the exact defects that mediated the {1 1 -2 1} twinning, in situ compression tests were carried out to characterize the {1 1 -2 1} twinning process at atomic resolution. In <1 -1 0 0>

view (see Figure 6.4), the smallest distance between atom columns was ~1.38 Å which was larger than the spatial resolution of the TEM; and hence atomic resolution could be validly achieved. Moreover, the detectable magnitude of twinning shear was largest and the K_2 plane was edge-on under this viewing direction. These features of the viewing direction enabled the study of atomic twin-boundary structures.

Figure 6.4 shows the sequential HRTEM snapshots of a Re nanocrystal under [1 -2 1 13]-oriented tension. Note that the maximum Schmid factors for the {1 1 -2 1}<1 1 -2 -6> twinning and basal <***a***> slip were 0.44 and 0.23, respectively. The deformation in tension and subsequent unloading/compression was mediated by the {1 1 -2 1} twinning and detwinning, respectively. By imaging the intersection of the surface and the propagating twin boundary, individual twinning dislocations and surface facet evolution were recorded. The migration of the twin boundary was found to be mediated by twinning dislocations which had universal step height of 1/2 {1 1 -2 1} plane, i.e. ($\boldsymbol{b}_{1/2}$, $h_{1/2}$). Furthermore, as indicated by the surface facet evolution (see red arrows in Figure 6.4), basal surface facets of the matrix transformed into basal surface facets of the twin during twinning process; this planar correspondence directly proved that the basal plane was the second invariant plane (i.e. K_2). By measuring the surface inclination (i.e. rotation angle of the K_2 plane), the magnitude of twinning shear was estimated to be ~0.65, which was reasonably consistent with the theoretical predictions (~0.62 for Re). It should be noted that twinning dislocations with much larger step heights were occasionally discovered during the {1 1 -2 1} twinning growth, but they generally had a much lower mobility than the ($\boldsymbol{b}_{1/2}$, $h_{1/2}$); and according to the in situ observations here, the ($\boldsymbol{b}_{1/2}$, $h_{1/2}$) dislocations were the dominant interfacial defects that mediated the {1 1 -2 1} twinning process.

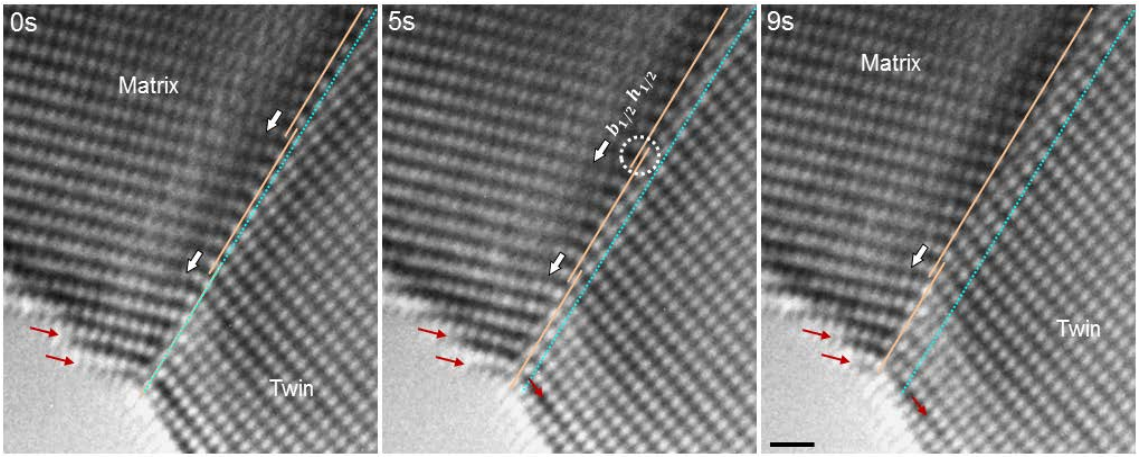

Figure 6.4 Sequential in situ HRTEM snapshots of the {1 1 -2 1} twinning growth process in a Re nanocrystal under [1 -2 1 13]-oriented tension, viewing along the plane of shear. The images are aligned. Pink lines indicate the {1 1 -2 1} twin boundary. Red arrows indicate the evolution of surface facets during twinning process. Cyan lines are reference line for tracking the thickening of the twin. White circle and white arrows indicate the twinning dislocations of (***b***$_{1/2}$, $h_{1/2}$) type and their motion direction. Scale bar, 500 pm.

6.3.4 In situ atomic-resolution observation of {1 1 -2 1} detwinning

Figure 6.5 shows sequential atomic-resolution TEM snapshots of the detwinning process of a {1 1 -2 1} twin. The Re nanocrystal was initially under [2 -4 2 23]-oriented tension; and the deformation was mediated by nucleation and growth of a {1 1 -2 1} twinning. Upon unloading or reversed loading, the deformation was dominated by detwinning of the {1 1 -2 1} twin. As shown in Figure 6.5a, the detwinning proceeded by migration of the twin boundary which resided on the coherent {1 1 -2 1} twinning planes throughout the process. Enlarged atomic-resolution TEM image of the twin boundary revealed unambiguously a dislocation (see Figure

6.5b) which had a step height of half {1 1 -2 1} plane and was the same as the twinning dislocation of ($\boldsymbol{b}_{1/2}$, $h_{1/2}$) discovered in twinning growth (see Figure 6.4).

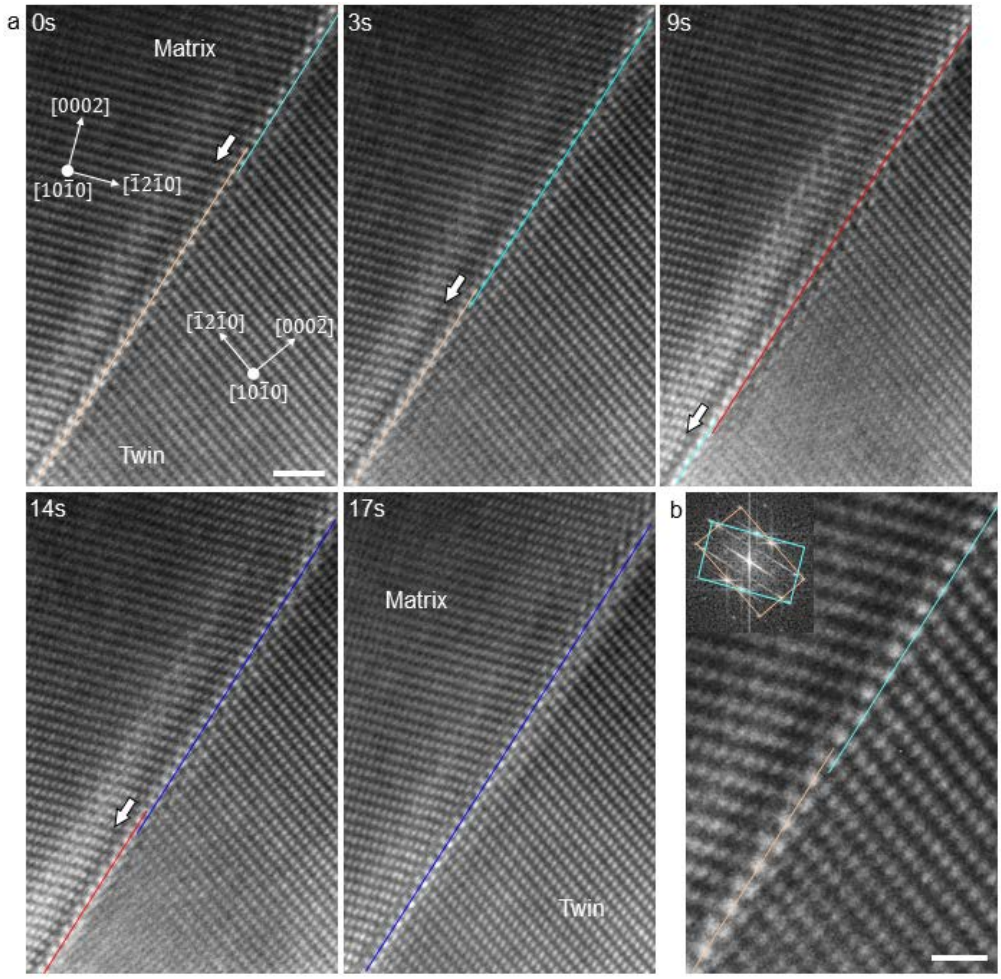

Figure 6.5 ($\boldsymbol{b}_{1/2}$, $h_{1/2}$) twinning dislocation mediated detwinning of a {1 1 -2 1} twin. CTBs are discerned by colored lines. (a) Sequential atomic resolution snapshots of the process. (b) Enlarged HRTEM image of a twinning dislocation on the {-1 2 -1 1} twin boundary. Inset is the FFT of the region. Scale bar in (a) 1 nm; scale bar in (b) 500 pm.

It is surprising that the reverse deformation is mediated by the detwinning rather than basal slip in the twin considering that the Schmid factor for basal slip in the twin was quite large

(~0.49). A possible explanation for the detwinning mediated reverse deformation is that the stress required for basal dislocations nucleation (see calculation on Mg[169]) is higher than that required for the ($\boldsymbol{b}_{1/2}$, $h_{1/2}$) twinning dislocation migration (see calculation in Zr[51]). Above all, the in situ observations provide clear evidences that {1 1 -2 1} twinning is shear-dominated process mediated predominantly by twinning dislocations; and the conjugate twinning plane was basal plane and the twinning shear was ~0.6, which were all consistent with the expectation of classical twinning theories. However, the dominant twinning dislocations are the mobile ($\boldsymbol{b}_{1/2}$, $h_{1/2}$) dislocations rather than ($\boldsymbol{b}_1$, h_1), providing direct evidences to the prediction of molecular dynamics simulations[51,62]. It should be noted that the ($\boldsymbol{b}_1$, h_1), if present, would likely dissociate into two ($\boldsymbol{b}_{1/2}$, $h_{1/2}$) dislocations spontaneously, since the ($\boldsymbol{b}_{1/2}$, $h_{1/2}$) carries a smaller Burgers vector and the dissociation significantly reduces the long-range elastic strain energy of the ($\boldsymbol{b}_1$, h_1) twinning dislocation.

6.3.5 In situ investigation of atomic shuffles in the {1 1 -2 1} twinning

To determine whether atom shuffles were involved in the twinning process, in situ HRTEM investigation was carried out by viewing the {1 1 -2 1} twinning process along the <1 1 -2 -3> direction. Though the <1 1 -2 -6> view is the best choice to detect atom shuffles in this twinning mode, 2D atomic (or lattice) resolution image cannot be achieved along <1 1 -2 -6> viewing direction, due to the fact that the minimum distance between atom columns within the prismatic layers is smaller than the spatial resolution of the TEM; moreover, it is hard to determine whether the twinning if there the shuffle is trivial. Referring to the projection of the {1 1 -2 1} twinning plane, <1 1 -2 -3> was the only low-index direction that had a non-zero projection on

the <1 -1 0 0> shuffle direction (see Figure 6.6); and hence it was the best viewing direction to study atomic shuffles in the {1 1 -2 1} twinning.

As shown in Figure 6.7a, the pristine Re nanocrystal was defect-free with a diameter of ~18nm and an asperity ratio of ~1.2. Upon [-6 5 1 -1]-oriented compression and de-compression, deformation of this nanocrystal was dominated by {1 1 -2 1} twinning and detwinning, respectively (see Figure 6.7b). The twinning nucleated from the surface near the grain boundary. After nucleation, the twinning grew by shearing the matrix and the twin boundary migrated concomitantly. Sequential lattice-resolution TEM snapshots of the twin boundary propagation were shown in Figure 6.8. No twinning dislocations or step features could be identified directly from the snapshots. However, the operation of twinning dislocations was hinted by the "step-wise" movement of the twin boundary (see Figure 6.8). The twin boundary apparently advanced by one {1 1 -2 1} layer each step, implying that the dominating twinning dislocation should have a maximum step height of one {1 1 -2 1} layer; in other words, the operating twinning dislocations should be ($\boldsymbol{b}_{1/1}$, $h_{1/1}$) or ($\boldsymbol{b}_{1/2}$, $h_{1/2}$). Considering the fact that the twin boundaries leaded by ($\boldsymbol{b}_{1/2}$, $h_{1/2}$) and ($\boldsymbol{b}_{1/1}$, $h_{1/1}$) have the same lattice image under <1 1 -2 -3> observation, it is essentially impossible to differentiate these two twinning dislocation under <1 1 -2 -3> viewing direction. Considering that no moving single-layer steps, which would likely present if the dominant twinning dislocations were ($\boldsymbol{b}_{1/1}$, $h_{1/1}$) type, were captured on the twin boundary, the dominant twinning dislocations should be ($\boldsymbol{b}_{1/2}$, $h_{1/2}$) the same as those found in Figure 6.4.

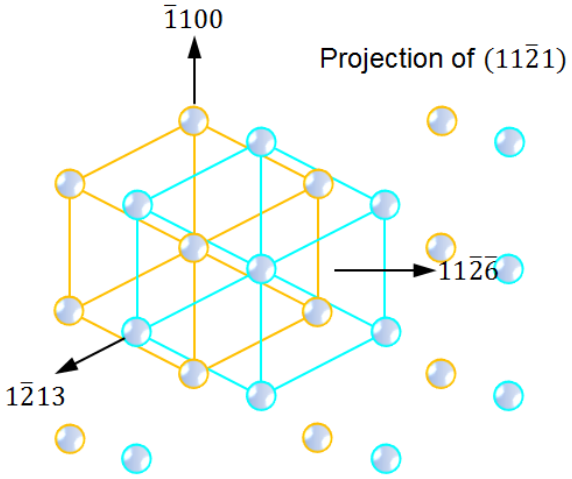

Figure 6.6 Structure model of the (1 1 -2 1) twinning plane. Atoms and lattices of the two sub-planes, i.e. the (2 2 -4 2) planes, are distinguished by yellow and cyan colors. Arrows indicate the low-index directions within the plane.

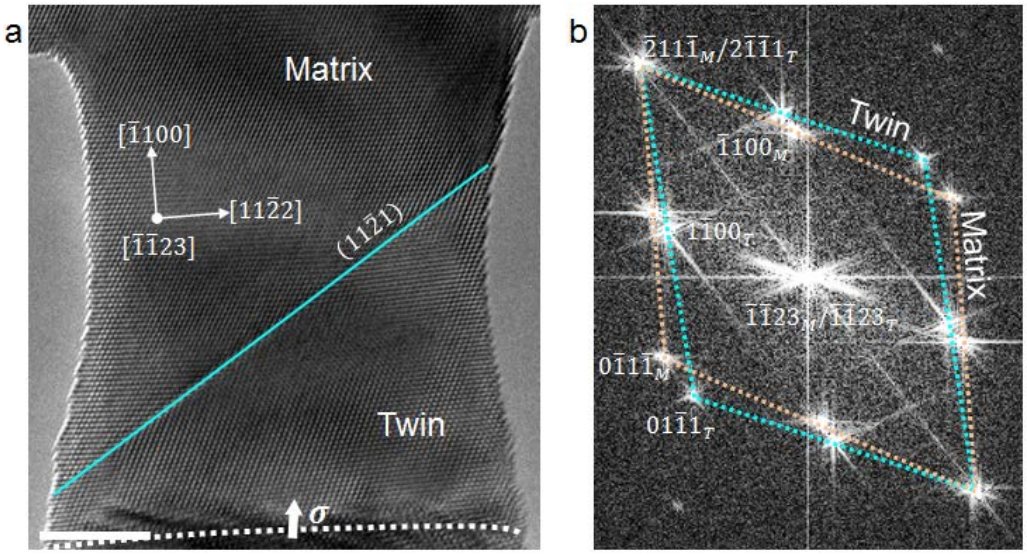

Figure 6.7 HRTEM observation of the {1 1 -2 1} twinning process viewing along <1 1 -2 3> direction. (a) The Re single-crystal used for the experiment. Cyan lines indicate the {1 1 -2 1} twin boundary. (b) FFT of the twinning region in panel (a), showing an orientation relation that is fully consistent with that of a {1 1 -2 1} twinning. Pink and cyan squares indicate the reciprocal lattices of the twin and matrix, respectively. Scale bar in (a) 5 nm.

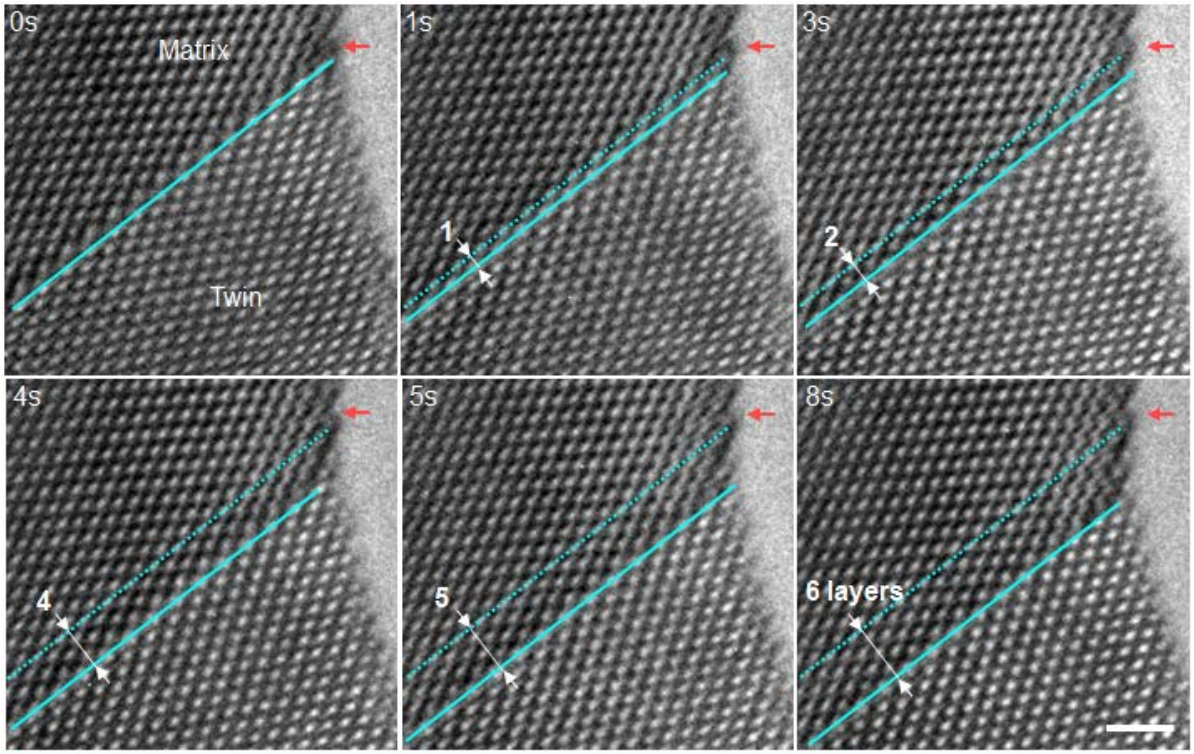

Figure 6.8 Sequential HRTEM snapshots showing the {1 1 -2 1} coherent twin boundary migration (during detwinning). Solid and dash cyan lines indicate the current and original (0s) position of the twin boundary. Red arrows marked the reference point. Scale bar, 1 nm.

To identify the atomic shuffles involving in the {1 1 -2 1} twinning, detailed HRTEM analysis was carried out on the in situ snapshot of the twin boundary during twinning growth (Figure 6.9). In the <1 1 -2 -3> view, the edges of the prismatic planes were marked as red lines in Figure 6.9a. As shown in the atomic model (Figure 6.9b), if there was no atomic shuffle along the <1 -1 0 0> direction, the edges of the prismatic planes in the matrix and the twin should be connected exactly on the twin boundary with perfect mirror symmetry. On the other hand, if there were atomic shuffles, the edges of the prismatic planes in the matrix and the twin should be detached on the twin boundary (see Figure 6.9c). In fact, the latter case is exactly what has been observed (see red lines and yellow arrow in Figure 6.9a). The magnitude of lateral detachment of

the red lines at the twin boundary is measured to be ~0.7Å (see Figure 6.9a), corresponding to ~0.8Å magnitude of shuffle along the <1 -1 0 0> direction.

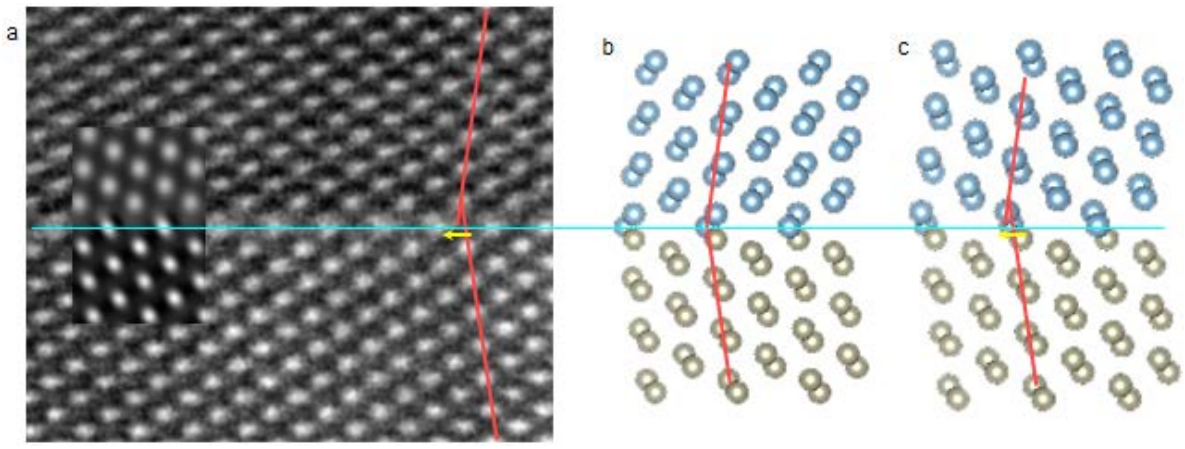

Figure 6.9 Determine the atomic shuffles by using in situ snapshot of the moving {1 1 -2 1} twin boundary. (a) Enlarged lattice image of the {1 1 -2 1} twin boundary (marked by cyan line). Inset shows the simulated HRTEM image of the atomic model in panel (c). (b) <1 1 -2 -3> projection of the atomic model of an {1 1 -2 1} twin boundary with no shuffle. Matrix and twin atoms were colored in cyan and gray, respectively. (c) <1 1 -2 -3> projection of the atomic model of an {1 1 -2 1} twin boundary with atomic shuffles. Red lines mark the edges of prismatic planes. Yellow arrows in (a, c) indicate the projection of the shuffle vector.

Referring to the 4 scenarios of atomic-shuffle mechanisms in topological analysis[111], structure models for each of these scenarios were constructed and used as input for simulating HRTEM images which were then compared with our in situ HRTEM snapshot in Figure 6.9a. Note that the HRTEM simulation employed a multi-slicing method and the parameters used for the simulation were reasonable estimations of the actual state of the experiment. Specifically, TEM accelerating voltage was 300*KeV*, spherical aberration was 20nm, defocus was 25nm and thickness of the structure models were ~12nm (consistent with the estimated sample thickness at

the local region where the TEM snapshot in Figure 6.9a was taken). Through trial and error, best match was found which showed atoms on alternative basal planes shuffling along ~1/6<-1 1 0 0> direction (as schematically shown in Figure 6.10). Incidentally, the magnitude of shuffle in the model of best match is ~0.8Å which is precisely consistent with our measurement in Figure 6.9a.

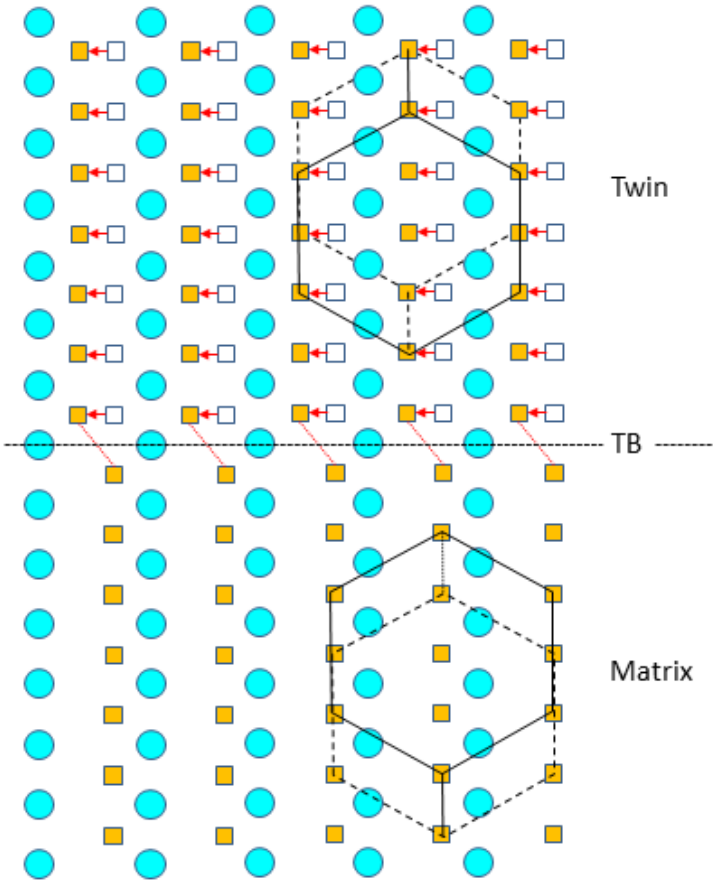

Figure 6.10 Schematic illustration of the atomic shuffles in the best matching model, viewing along the <1 1 -2 -6> direction. Cyan balls and yellow squares represent atoms on adjacent basal planes. Red arrows represent the shuffles of atoms on the yellow basal plane. Projection of HCP unit-cells are drawn in black lines.

It should be noted that simulations on shuffles involving in the {1 1 -2 1} twinning process started decades ago. Various scenarios of shuffles have been proposed through simulations. Crocker *et al.* believed that no shuffle along the <1 -1 0 0> direction was required[167]. Morozumi *et al.* proposed four scenarios and believed that atomic shuffles of $\mp$1/12<1 -1 0 0> on alternative basal planes was the most likely scenario for {1 1 -2 1} twinning[111]. Similar scenario of atomic shuffle was also reflected in the simulations by Pond *et al.*[51]. Yet, according to our experimental observation, the atomic shuffles were only carried by every other basal planes and had a magnitude of ~1/6<1 -1 0 0>. This finding is intriguing in that the shuffle magnitude is not the minimum. The sample surface may be hold accountable. When all basal planes shuffles, e.g. in $\mp$1/12<1 -1 0 0> scenario[111], the prismatic surface facets would be severely bended at the twin boundary. The surface tension on the prismatic surface facets would presumably counteract such bending by reducing the shuffles on surface prismatic facet. Thereafter, the prismatic layer right beneath the surface would have to take a larger share of the shuffle, i.e. ~1/6<1 -1 0 0>; and the rest prismatic planes of the crystal react accordingly. Whatever the exact reason is, when the sample surface could play a role, the sample size would play a role.

6.4 CONCLUSIONS

Through in situ TEM studies, the {1 1 -2 1} twinning process in Re nanocrystals have been successfully captured at high resolution. The results reveal unprecedentedly and unambiguously the shear and atomic shuffles in the twinning process, as well as the dominant twinning

dislocations. The findings provide direct experimental evidences to the classical twinning theories and recent simulations on the {1 1 -2 1} twinning mode.

It was found that the {1 1 -2 1} twinning was a shear-dominated process mediated by twinning dislocations. The twinning shear and all twinning elements revealed by HRTEM observation were fully consistent with the prediction of classical twinning theories. The twinning growth as well as detwinning were primarily mediated by ($\boldsymbol{b}_{1/2}$, $h_{1/2}$) twinning dislocations, rather than ($\boldsymbol{b}_1$, h_1) in classical prediction. Twinning dislocation with much larger step height was also identified, but showed much lower mobility than ($\boldsymbol{b}_{1/2}$, $h_{1/2}$) dislocations. Moreover, direct evidence of atomic shuffles was revealed in the twinning process, as manifested by a lack of mirror symmetry on the twin boundary. The atoms on alternative basal planes shuffled ~1/6<-1 1 0 0> in the {1 1 -2 1} twinning process.

7.0 IN SITU TEM INVESTIGATION OF {1 1 -2 2} TWINNING

7.1 INTRODUCTION

The {1 1 -2 2} twinning is believed to be a contraction twinning that widely exists in HCP metals, e.g. Zr[68], Y[170], and Ti[41,56,69]. Classical twinning theories, based on the assumptions that feasible twinning modes should have small twinning shear and simple atomic shuffles, predict that the K_2 for the {1 1 -2 2} twinning should be the {1 1 -2 -4} plane[19,59] (see Figure 2.3); and the twinning shear is relatively low $2(\gamma^2-2)/3\gamma$ (~0.25 for Re), but the required shuffles are large and complex[19,60]. When the {1 1 -2 -2} plane becomes the K_2 plane, the required shuffles are simpler, but the twinning shear increases to $\gamma-\gamma^{-1}$ (~0.99 for Re)[60]. Recent molecular dynamics simulations on the {1 1 -2 2} twinning reported that the K_2 plane might be the basal plane[60,61,65]. In this case, according to topological analysis, the {1 1 -2 2} twinning would require no atomic shuffle[59]. Yet, the simulation results are deemed "unlikely" due to the attendant extremely large twinning shear of $2/\gamma$ (~1.24 for Re) which confronts the small twinning shear assumption in classical twinning theories[19,59,60]; in addition, the {1 1 -2 2} twinning mode requires tension along <***c***> axis and is expected to be inactive due to its competition with the other easy twinning modes, e.g. {1 1 -2 1} and {1 0 -1 2} twinning[59]. It is further demonstrated that, considering the sense of the twinning shear, the finding that (0 0 0 1) K_2 plane requires tension along <***c***> axis and hence does not confront with the classical {1 1 -2 -4} K_2 plane which requires compression

along <***c***> axis[59]. Even if there is a tension twinning mode on {1 1 -2 2} twinning plane, the K_2 plane may not be basal but {1 1 -2 -6} which will render much lower twinning shear but more complex shuffles. The first target is to investigate whether {1 1 -2 2} twinning is feasible under tension along <***c***> axis and identify the corresponding K_2 plane through in situ TEM.

Second, as a result of the debatable K_2, the magnitude of twinning shear for the {1 1 -2 2} twinning is also debatable. The twinning shear of ~0.2 has been determined experimentally in Zr[68] and Ti[69] under <***c***> axis compression, which is consistent with the expectation of classical twinning theory when the K_2 is {1 1 -2 -4}. When the K_2 is basal plane, the twinning shear should be ~1.2[59,61-63]. Yet, some simulation work also argues that the twinning shear can be significantly reduced when atoms on the twin boundary shuffle along the η_1 direction[60,66]. The second target in this chapter is to measure the actual twinning shear (and hence the atomic shuffles) for the {1 1 -2 2} tension twinning by tracking the atomic motion and the surface facet inclination during twinning.

Third, the dominant twinning dislocation in {1 1 -2 2} twinning remains elusive[62,63]. According to the classical theory, when K_2 is {1 1 -2 -4}, the twinning dislocation should have a step height of three {1 1 -2 2} layers. However, when K_2 is basal plane, the twinning dislocation should be elementary, i.e. have a step height of one {1 1 -2 2} layer. When K_2 is {1 1 -2 -6}, the twinning dislocation should span two {1 1 -2 2} layers. The third target is to capture the dominant twinning dislocations for {1 1 -2 2} twinning.

7.2 PROCEDURE

The basic procedures of the in situ experiment were the same as those described in Chapter 3.3. It was suggested that the {1 1 -2 2} tension twinning mode was inactive due to the competition with {1 0 -1 2} and {1 1 -2 1} twinning under tension loading along <***c***> axis[59]. In order to render a relatively higher Schmid factor for the {1 1 -2 2} twinning mode than those for the basal slip and the competing twinning modes, orientation of the Re nanocrystal in this investigation was tuned to a few degrees (ideally ~13^{o}) off the <***c***> axis about <1 -1 0 0>. To determine the K_2 plane, in situ HRTEM observation was carried out to track the motion of each atom columns and hence establish the correspondence of atomic planes; especially, evolution of the basal surface facet during the {1 1 -2 2} twinning process would be captured to determine whether it was invariant during twinning. Besides, the viewing direction was tuned to <1 -1 0 0> such that the K_2 plane, the twinning plane, and the twinning dislocation were edge-on and easy to identify. The atomic resolution sequential snapshots were taken for tracking the shear movement of each atom columns during the {1 1 -2 2} twinning process; thus, the magnitude of twinning shear can be precisely measured. The strain rate was controlled to be ~10^{-3} s^{-1} in all tests.

7.3 RESULTS AND DISCUSSION

7.3.1 Revealing the K_2 through in situ atomic-resolution TEM

The basal surface facet evolution during the {1 1 -2 2} twinning process in Re nanocrystal was shown in Figure 7.1 (see red lines). The Re nanocrystal was under tensile deformation roughly

along the [1 1 -2 6] direction (roughly <***c***> axis tension); note that the Schmid factor for the (-1 -1 2 2)[-1 -1 2 -3] twinning dislocation was ~0.45 in this case. The deformation was primarily mediated by the {1 1 -2 2} twinning (see the coherent twin boundary in Figure 7.1). Upon reversed loading, the {1 1 -2 2} twin boundary (see green lines) migrated downward. The basal surface facet in the twin transformed into basal surface facet in the matrix, manifesting a correspondence relation between the matrix basal and the twin basal. In other words, the basal plane was the second invariant plane in the {1 1 -2 2} twinning process. By tracking the movement of atom columns in the view, atomic correspondence could be identified wherein the matrix {1 1 -2 -4} plane transformed into the {1 1 -2 -8} plane in the twin (see yellow lines in Figure 7.1b), indicating that the {1 1 -2 -4} plane was not invariant in this twinning process. These observations provided direct evidences that the {1 1 -2 2} tension twinning does exist and its K_2 plane is the basal plane.

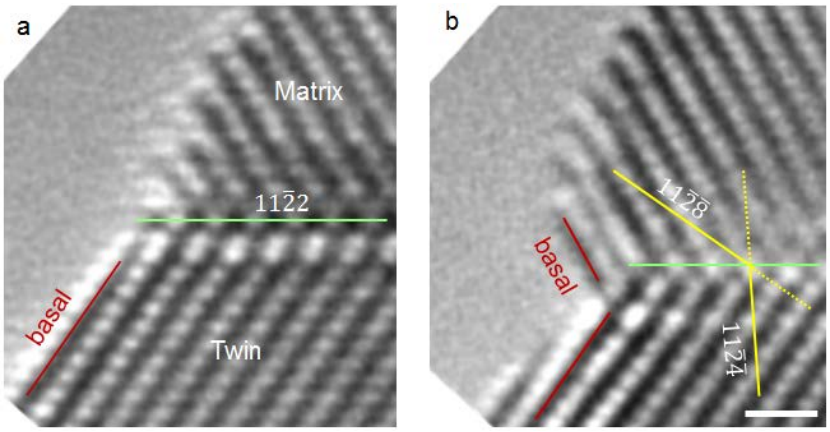

Figure 7.1 Sequential atomic resolution snapshots of a {1 1 -2 2} twin boundary (indicated by green lines) propagation, viewing along the <1 -1 0 0> direction. Red lines indicate the basal surface facets. Yellow lines indicate the correspondence between the matrix {1 1 -2 -4} plane and the twin {1 1 -2 -8} plane. Scale bar, 500 pm.

The choice of basal as the K_2 plane over {1 1 -2 -4} and {1 1 -2 -2} has been attributed to the loading directions[59]. Under tension along <***c***> axis, the available (or competing) choices for K_2 plane are {1 1 -2 -6} and (0 0 0 1). Compared with the case where the K_2 plane is {1 1 -2 -6}, the (0 0 0 1) K_2 results in a much larger theoretical twinning shear (0.1 vs. 1.2) and but much simpler theoretical atomic shuffles. Therefore, the choice of (0 0 0 1) over {1 1 -2 -6} as the K_2 plane implies that simple atomic shuffles may be more important than small twinning shear for twinning in HCP nanocrystals.

7.3.2 Twinning shear for {1 1 -2 2} twinning

A twinning shear of ~1.2 could be estimated based on the inclination of the originally flat basal surface facet Figure 7.1. The magnitude of the twinning shear could also be measured directly from the sequential atomic-resolution TEM snapshots of the {1 1 -2 2} twinning process. As shown in Figure 7.2b&d, the {1 1 -2 2} twin boundary during straining migrated "step-wisely" at one {1 1 -2 2} layer per step, implying the operation of the elementary twinning dislocations. The magnitude of twinning shear carried by such elementary twinning dislocation could be calculated by dividing the movement of the basal planes along the shear direction (1.3~1.4 Å, see the measurements in Figure 7.2b&d) by the *d*-spacing of the {1 1 -2 2} planes (~1.17 Å). Using this method, twinning shear was measured to be ~1.15, roughly consistent with the value obtained from surface inclination as well as the values reported in previous simulations[59,61-63].

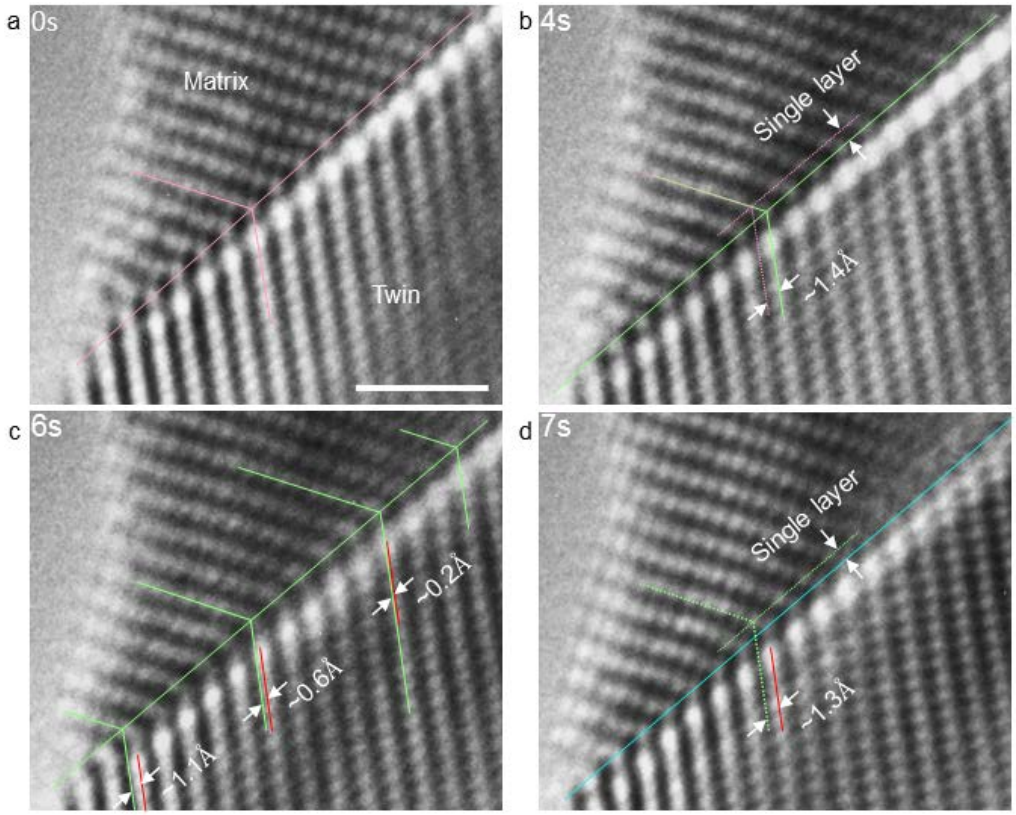

Figure 7.2 Sequential atomic resolution TEM snapshots showing the nucleation and operation of elementary twinning dislocations from surface during the detwinning of a {1 1 -2 2} twin. The twin boundary migrated one {1 1 -2 2} layer every step, implying the operation of elementary twinning dislocations. The positions of individual twin boundaries are marked by color-coded straight lines. Panel (c) shows a state of twinning dislocation nucleation. The symmetrical K_2 and K_2' planes are marked by zigzag lines; the magnitude of shear was indicated by translation of the basal planes along the shear direction. Scale bar in (a), 1 nm.

It should be noted that the process shown in Figure 7.2 is a detwinning process of a {1 1 -2 2} twin. The same twinning shear and type of dominant twinning dislocation were revealed in the twinning growth process (see Figure 7.3).

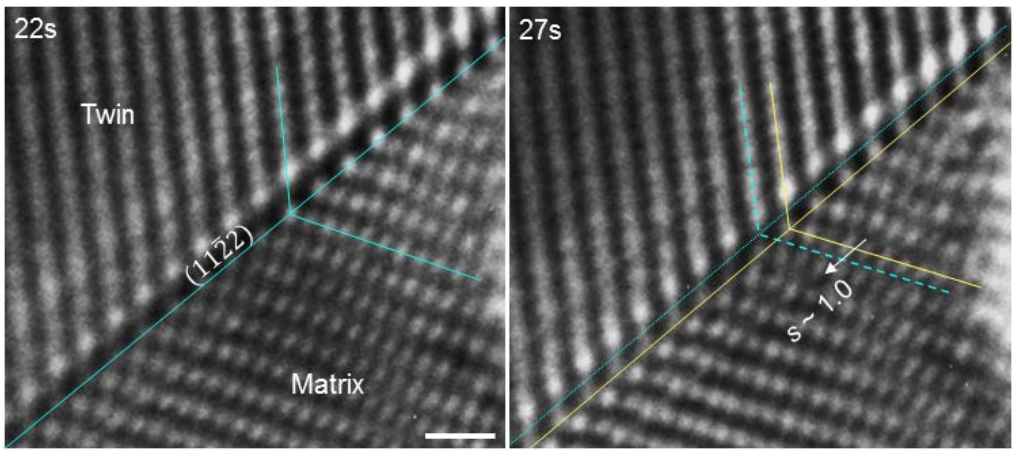

Figure 7.3 Sequential atomic resolution images showing the {1 1 -2 2} twinning growth via elementary twinning dislocations. The twinning shear can be measured by tracking the movement of basal (K_2) planes. Zig-zag lines indicate the symmetrical K_2 and K_2' planes. White arrow indicates the migration of a basal plane as the twin expands one {1 1 -2 2} layer. Scale bar in (a), 500 pm.

It should be noted that the measured twinning shear is slightly lower than the theoretical value (~1.24) for Re, which may be related to the experimental error or the presence of minor atomic shuffles on the twinning plane along the twinning shear direction. Though, based on topological analysis, no atomic shuffle is required in the {1 1 -2 2} twinning process when K_2 is the basal plane. The step height of the dominant twinning dislocation strongly supports the fact that basal plane is K_2, as in any other choices of K_2, {1 1 -2 -4} or {1 1 -2 -6}, the elementary twinning dislocation would not be stable.

It should be noted that such an exceptionally large twinning shear was believe unrealistic[19,66], considering that it would require large strain accommodation in bulk samples. In our case, due to the small sample sizes, no mechanism of strain accommodation for the large twinning shear was needed, because the twin penetrated through the whole cross-section of the nanocrystal since nucleation. This is essentially different from grains embedded inside a

polycrystalline bulk sample wherein the twinning lamella could never reach the sample surface and hence would require significant amount of plastic deformation in front of the twin tip to accommodate the twinning shear[19]. Therefore, the choice of K_2 and attendant large twinning shear should have been prompted by the small sample size. Additionally, previous molecular dynamics simulations revealed that complex atomic shuffles could be unfavorable in the relatively low temperatures[59]. The room temperature in our experiment condition may have prompted the twinning to choose an easy-shuffle way.

7.3.3 Nucleation and mobility of twinning dislocations from surface

A snapshot on the nucleation process of an elementary twinning dislocation was captured in Figure 7.2c. As indicated by the green and red markers, shear distributed inhomogenously on the {1 1 -2 2} twin boundary during the process; the shear was largest on the surface ~0.9, gradually decreased away from the surface and finally diminished at ~3.8nm into the crystal (i.e. ~26 times the $|\boldsymbol{b}_t|$, Burgers vector of the twinning dislocation). These results indicate that the elementary twinning dislocations were highly dissociated during nucleation from the surface.

It was further captured that the twinning dislocations were fairly mobile (see Figure 7.4), consistent with previous simulations[59,61,64]. Note that the speed of the elementary twinning dislocations varied from case to case between ~0.1 nm/s to >1nm/s. Additionally, the twinning dislocation might have a wide core (~1.2 nm or ~8 times of its Burgers vector) which could be accountable for the mobility of the twinning dislocations[63]. Though, it was also possible that the twinning dislocation was just not edge-on.

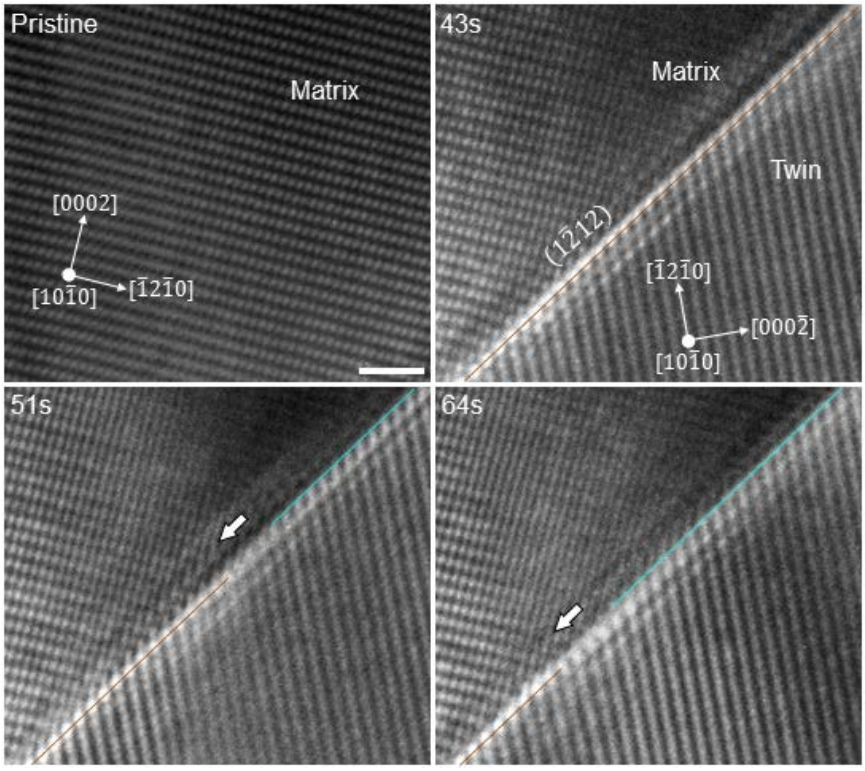

Figure 7.4 Sequential atomic resolution TEM snapshots showing the migration of the {1 1 -2 2} twin boundary via the movement of elementary twinning dislocation (indicated by block arrows). Sections of the twin boundaries were color-coded. Scale bar, 1 nm.

7.3.4 Interaction between the basal slip and the {1 1 -2 2} twinning growth

Figure 7.5 shows the interaction between the basal slip and the {1 1 -2 2} twinning. An <***a***>-type dislocation was emitted from the upper-left corner of the twin at 0s; it glided along the basal plane and intersected the twin boundary (see yellow arrow and markers in the 2s snapshot). The dislocation was temporarily arrested by the twin boundary. A rough measurement on the lattice spacing nearby the intersection showed that the local compressive strain increased before the basal dislocation penetrated the {1 1 -2 2} twin boundary and transited onto the matrix (see 3s

snapshots), implying a strengthening effect of this process. Interestingly, this process incurred the advancement of the twin boundary by one {1 1 -2 2} layer, manifesting that the basal slip assisted the twinning growth.

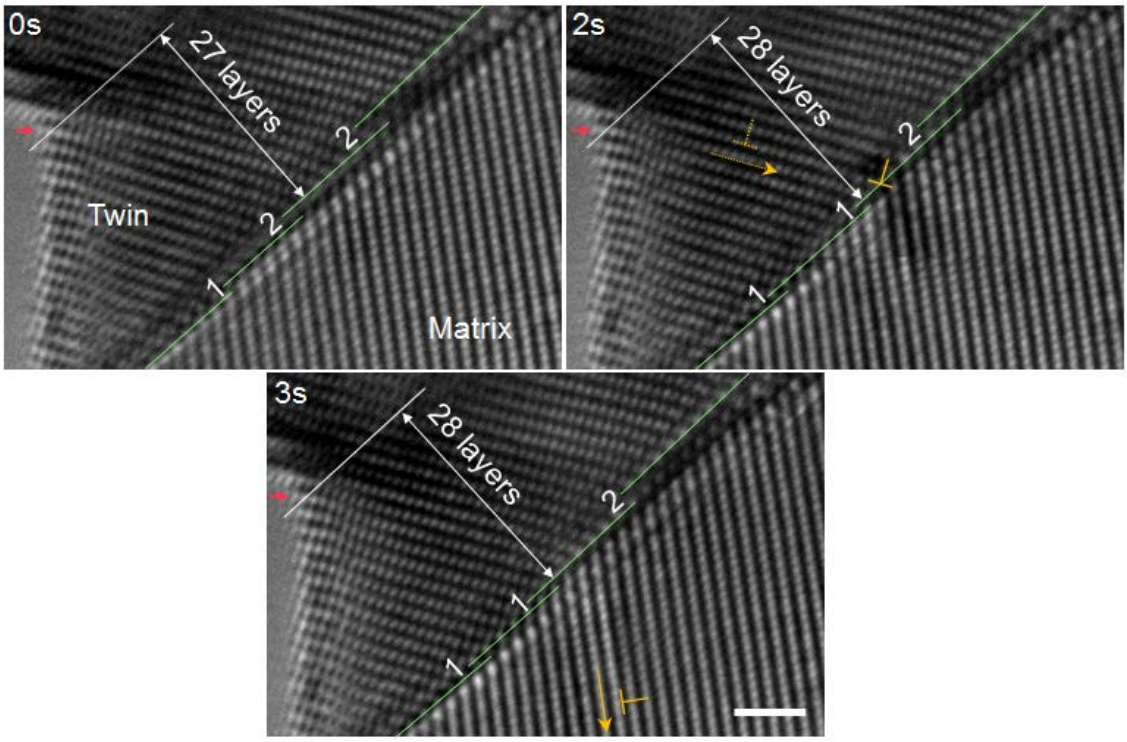

Figure 7.5 Sequential atomic resolution TEM snapshots showing the interaction process of a basal dislocation with a {1 1 -2 2} twin. Red arrows indicate the reference point. Green lines indicate the {1 1 -2 2} twin boundaries. Numbers indicate the step heights of the steps (or twinning dislocations) on the twin boundary. Scale bar, 1 nm.

To understand the dislocation "reactions" associated with the observed process in Figure 7.5, topological analysis was carried out (see Figure 7.6). First of all, the Burgers vectors of the original dislocation in the twin and the on-going dislocation in the matrix were determined. Based on the atomic image of the dislocation (see Figure 7.5 and Figure 7.6d), the Burgers

vector of the on-going dislocation in the matrix should be one of the <***a***>-type that inclined 30^{o} with respect to the viewing direction; thereby, the "apparent" Burgers vector (or edge component) in current view was only 1/2<***a***>. It should be noted that, based on the surface edge generated by the dislocation emission (see 0~2s snapshots in Figure 7.5), the original dislocation in the twin should also be a 30^{o} <***a***> dislocation. As such, it was not a dislocation transmutation process[24] and the dislocation type and magnitude of the Burgers vector remained invariant before and after the penetration.

As shown in the atomic model of the basal plane (Figure 7.6b-c), the Burgers vector of the original dislocation in the twin could dissociate into two Shockley partials according to <$\boldsymbol{a}_1$> = <$\boldsymbol{b}_1$> + <$\boldsymbol{b}_s$>; and the Burgers vector of the on-going dislocation in the matrix could dissociate according to <$\boldsymbol{a}_2$> = <$\boldsymbol{b}_2$> + <$\boldsymbol{b}_s$>; wherein, <$\boldsymbol{b}_1$> and <$\boldsymbol{b}_2$> were partial dislocations containing edge components of the original and on-going dislocations; <$\boldsymbol{b}_s$> was the partial dislocation containing only the screw component which was invariant in the reaction. The transition of the original dislocation into the on-going dislocation was essentially <$\boldsymbol{a}_1$> → <$\boldsymbol{a}_2$>, or <$\boldsymbol{b}_1$> → <$\boldsymbol{b}_2$>. To keep the Burgers vector consistent, an additional dislocation (hereinafter referred to as <$\boldsymbol{b}_3$>) must be generated to satisfy <$\boldsymbol{a}_1$> = <$\boldsymbol{a}_2$> + <$\boldsymbol{b}_3$> or <$\boldsymbol{b}_1$> = <$\boldsymbol{b}_2$> + <$\boldsymbol{b}_3$>. As illustrated in the atomic model of the shear plane (Figure 7.6a), the <$\boldsymbol{b}_3$> was actually the shear component of an elementary ("single-layer") twinning dislocation. In other words, the transition process of the basal dislocation (or, <$\boldsymbol{a}_1$> → <$\boldsymbol{a}_2$>) through the {1 1 -2 2} twin boundary would generate a twinning dislocation (<$\boldsymbol{b}_3$>) on the twin boundary.

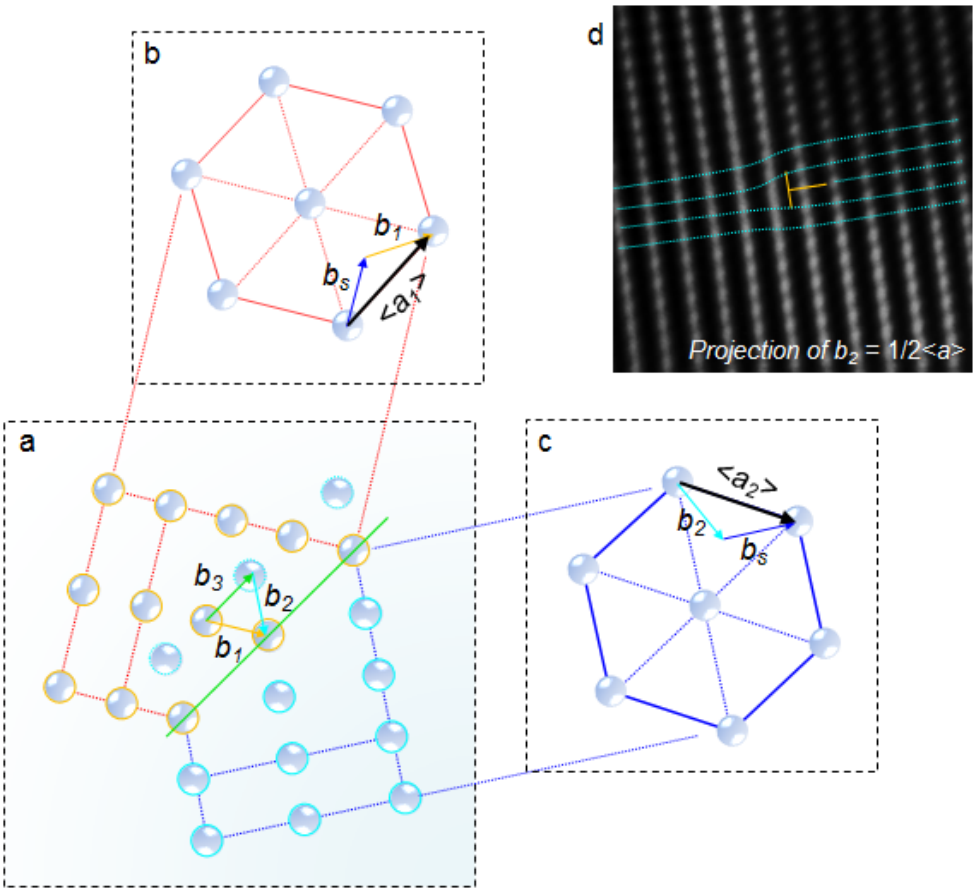

Figure 7.6 Topological analysis of the reaction between an <***a***> dislocation and the {1 1 -2 2} twin boundary. (a) Schematic image of the {1 1 -2 2} twin boundary viewing along <1 0 -1 0>. The twin and matrix were colored red/yellow and blue/cyan, respectively. The green line indicates the {1 1 -2 2} twin boundary. (b-c) Atomic model of basal planes in the twin and matrix. Black arrows indicate the Burgers vectors of the basal dislocations. Blue arrows indicate the screw components of the Burgers vectors. Yellow and cyan arrows indicate the Burgers vectors of the other partial dislocations with edge components. Green arrow in (a) indicate the Burgers vector of the twinning dislocation. (d) Enlarged HRTEM image (filtered) of the <***a***> dislocation viewing along the <1 0 -1 0> direction.

It should be noted that the dislocation reaction equation $<\boldsymbol{a}_1> = <\boldsymbol{a}_2> + <\boldsymbol{b}_3>$ can also be written as $<\boldsymbol{a}_1> + <-\boldsymbol{b}_3> = <\boldsymbol{a}_2>$, meaning that the elementary twinning dislocation with negative shear component (i.e. $<-\boldsymbol{b}_3>$) can assist the penetration process. In fact, this is exactly what has

been observed in experiments (see Figure 7.5). Comparing the 0s and 3s snapshots, the ($\boldsymbol{b}_2$, h_2) twinning dislocation in the vicinity of the intersection transformed into an elementary twinning dislocation after the basal dislocation penetrated through the twin boundary, in the meantime the twin boundary thickened by one {1 1 -2 2} layer.

It has been widely reported in FCC metals that the interaction between dislocations and twin boundaries can "fuel" the twinning dislocations for twinning growth[53]. As for HCP metals, similar mechanism has been developed for twinning growth[80], known as Serra-Bacon mechanism, which however remains a theoretical contention for decades. The in situ observation in Figure 7.5 presents unprecedented direct evidence to this mechanism.

7.3.5 Three-fold twinning on {1 1 -2 2} and {1 1 -2 1}

Due to the fact that both {1 1 -2 1} and {1 1 -2 2} twinning could be formed under tension along <$\boldsymbol{c}$> axis, the {1 1 -2 1} twinning and the {1 1 -2 2} twinning were usually nucleated simultaneously in our observations, forming a unique three-fold twinning (as shown in Figure 7.7). The three-fold twinning showed exceptional plasticity by the cooperative motion of associated twin boundaries. Typically, as shown in the sequential atomic-resolution TEM images in Figure 7.7a, one {1 1 -2 1} twin boundary (on the left) did not move; while the {1 1 -2 2} twin boundary and {1 1 -2 1} twin boundary (on the right) migrated cooperatively. When {1 1 -2 2} twin boundary advanced one layer (corresponding to the passage of an elementary twinning dislocation on the {1 1 -2 2} plane), the {1 1 -2 1} twin boundary advanced three half-layers of {1 1 -2 1} (corresponding to the passage of three ($\boldsymbol{b}_{1/2}$, $h_{1/2}$) twinning dislocations on {1 1 -2 1}). This process was reversible upon reverse loading.

To understand the fundamental reason for the observed cooperative twinning, topological analysis on the migration of the triple-twin-junction was carried out (see Figure 7.7b). The {1 1 -2 1} twin boundary on the left was kept sessile by translating the triple-junction along the <1 1 -2 -6> direction (i.e. along the left {1 1 -2 1} twinning). Obviously, the advancement of each {1 1 -2 2} plane translated to the advancement of three half-layers of the right {1 1 -2 1} plane. In other words, each elementary twinning dislocation on the {1 1 -2 2} twin boundary dissociated into three ($\boldsymbol{b}_{1/2}$, $h_{1/2}$) twinning dislocations on the {1 1 -2 1} twin boundary. This topological analysis is fully consistent with the TEM observations.

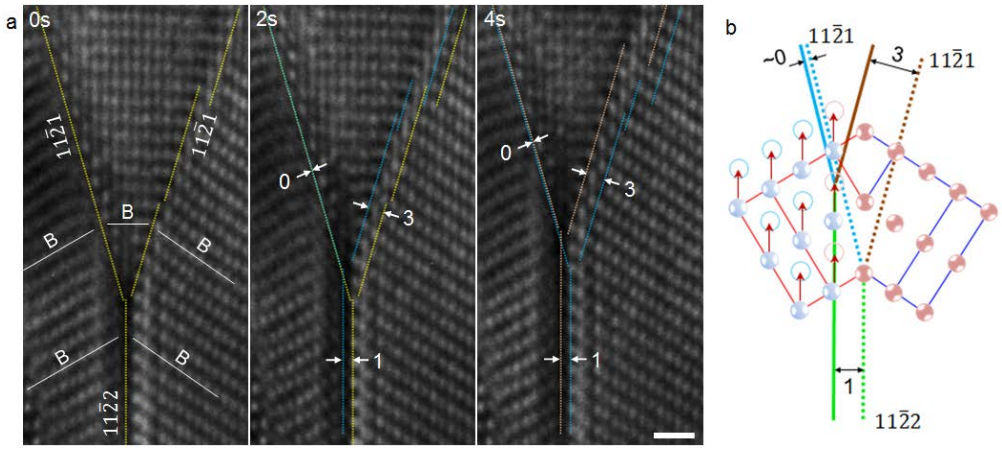

Figure 7.7 Movement mechanism of a {1 1 -2 1}-{1 1 -2 2} 3-fold twinning. (a) Sequential atomic-resolution images showing the migration of the 3-fold twinning junction. The viewing direction was <1 0 -1 0>. Dash lines indicate twin boundaries; the color corresponds to the time of capture. White lines indicate the basal (B) planes. Numbers indicate the number of dominant twinning dislocations required to complete the migration of the twin boundaries. Scale bar, 500 pm. (b) Topological analysis of the process in panel (a). Red arrows indicate the shear during the migration of the {1 1 -2 2} twin boundary.

Multiple-fold twinning have been widely reported in both FCC[171] and HCP metals[23,64], which were believed to contribute to the strength of the materials[23,172]. The in situ observations here provide an detailed picture of the mechanical responses of the three-fold twinning in HCP crystals; the results further supported the conclusion regarding the nature of dominate twinning dislocations in {1 1 -2 1} and {1 1 -2 2} twinning. The cooperative mechanism shown above further supported the exceptionally large twinning shear generate by the {1 1 -2 2} twinning. The total Burgers vector carried by the three ($\boldsymbol{b}_{1/2}$, $h_{1/2}$) twinning dislocations on {1 1 -2 1} had a magnitude of $3a/2\sqrt{(4\gamma^2+1)}$, i.e. ~1.2 Å, which was fairly consistent with that carried by an elementary twinning dislocation on the {1 1 -2 2} plane ($a/\sqrt{(\gamma^2+1)}$, ~1.4 Å, in case K_2 was basal). In contrast, if the K_2 plane for {1 1 -2 2} twinning was {1 1 -2 -4} plane (according to classical prediction[19]), the shear carrying by the single layer twinning dislocation on {1 1 -2 2} would be $a(\gamma^2-2)/\sqrt{(\gamma^2+1)}$, i.e. ~0.29 Å, which was much smaller than that carried by three ($\boldsymbol{b}_{1/2}$, $h_{1/2}$) twinning dislocations on {1 1 -2 1}; and hence the observed mechanism in Figure 7.7 would not be feasible. It should be noted that, though the observation proved the existence of a tension twinning mode with {1 1 -2 2} twinning plane, it does not disapprove the validity of the classical compression twinning mode on {1 1 -2 2} in which the K_2 plane should be {1 1 -2 -4}.

7.4 CONCLUSION

The {1 1 -2 2} twinning in HCP Re nanocrystals has been interrogated by in situ atomic-resolution TEM. Several “surprising” but unambiguous conclusions can be made on the fundamentals of this twinning mode. First, the {1 1 -2 2} twinning can be a tension twin with the basal plane as K_2. This finding stands in contrast to the conventional {1 1 -2 2} contraction

twinning wherein {1 1 -2 -4} plane is the K_2 plane. Second, based on direct measurements on the sequential atomic-resolution snapshots of the twinning process, the twinning shear was determined to be ~1.1. This result provides direct experimental evidence to the molecular dynamics simulations in literatures which are deemed "unlikely" previously. Based on the topological analysis and measured twinning shear, no or trivial shuffle is involved in the observed twinning mode. The choice of basal over {1 1 -2 -6} plane as the K_2 plane implies that "simple shuffles" rather than "small twinning shear" may be the dominate factor for the {1 1 -2 2} twinning at room temperature in nanocrystals. The large twinning shear associated with the observed twinning mode may have been prompted by the nanoscale sample size. Third, the dominant twinning dislocation in the observed twinning mode is elementary twinning dislocation which is fairly mobile and has a Burgers vector of $1/(3\gamma^2+3)$ <1 1 -2 -3>. The twinning dislocation was highly dissociated during nucleation (width > $26\left|\boldsymbol{b}_t\right|$).

In addition, the penetration of an <***a***> dislocation through the {1 1 -2 2} twin boundary was found to incur twinning growth, through the reaction of the basal dislocation with a twinning dislocation. This observation may be an evidence for the dislocation-assisted twinning growth mechanism in HCP metals[80]. The {1 1 -2 2} tension twinning mode and {1 1 -2 1} tension twinning mode can nucleate and operate together, in the form of three-fold twinning structure composing two {1 1 -2 1} and one {1 1 -2 2} twin boundaries. The three-fold twinning is fairly mobile through the cooperation of twinning dislocations.

8.0 SUMMARY AND CONCLUSIONS

In situ TEM has been used to investigate the mechanisms of deformation twinning in HCP metals at atomic-scale. The results reveal unprecedentedly unambiguous mechanisms of {1 0 -1 2} twinning, {1 1 -2 1} twinning, {1 1 -2 2} twinning, and HCP↔FCC phase transformations in HCP metals. Summary and conclusions are as follows,

{1 0 -1 2} twinning nucleation and growth in HCP nanocrystals were dominated by P→B and B→P transformations which, though did not generate the mirror symmetry of an ideal {1 0 -1 2} twin, established the same lattice correspondence as that of an ideal {1 0 -1 2} twin. As a result of the unique mechanism, the twinning nucleation was dominated by normal strains on the prismatic plane (or basal plane) rather than shear strain on the twinning plane, giving rise to the non-Schmid effect. For example, the twinning nucleation could be prompted by the compressive strain of an <$\boldsymbol{a}$> dislocation on the basal plane. Additionally, the incipient twinning was primarily bonded by the P│B and B│P interfaces which had no mirror symmetry. The twin boundaries retreated to coherent twin boundaries upon unloading thereafter, and further detwinning and instant reloading were mediated by ($\boldsymbol{b}_2$, h_2) twinning dislocations. This observation unambiguously proves that the classical twinning dislocation mechanism is indeed operative in {1 0 -1 2} twinning. Though, the twinning dislocation mechanism was apparently not dominant in the twinning formation of HCP nanocrystals. These in situ observations demonstrate that the co-existing CTB and B│P-type interfaces in extensive ex situ observations

may well be a detwinned structure. Due to the fact that the twinning can proceed in a "shuffle-dominated" manner, it has weak interaction with matrix dislocations and contaminant dislocations in front of the twin tip.

Two new HCP→FCC transformation mechanisms were revealed. The FCC structure formed from a HCP lattice by $(1\ 0\ \text{-}1\ 0)_{hcp}\rightarrow(1\ 1\ 1)_{fcc}$ transformation or $(1\ 0\ \text{-}1\ 1)_{hcp}\rightarrow(1\ 1\ 1)_{fcc}$ transformation. The in situ observation on transformation via HCP (1 0 -1 0) to FCC (1 1 1) presents a direct evidence for interfacial defect-mediated martensitic transformation. Subsequent transformation from $(1\ 1\ 1)_{fcc}\rightarrow(0\ 0\ 0\ 1)_{hcp}$ demonstrates that the FCC phase is capable of mediating grain rotation (including the {1 0 -1 2} twinning). These findings reveal a multifunctional role of the FCC phase in the deformation of HCP metals, and particularly, demonstrate a novel twinning mechanism. In addition, these new mechanisms and the previously reported HCP→FCC transformation mechanisms were subsumed under the analysis of lattice correspondence. The combined investigation of lattice correspondence analysis and in situ TEM demonstrates a new paradigm for exploring the non-diffusional transformation mechanisms in materials.

Twinning elements, twinning shear, and dominant twinning dislocations in the {1 1 -2 1} twinning process were unprecedentedly revealed here. Consistent with the predictions of the classical twinning theories, the in situ results indicated that the conjugate twinning plane was basal plane, the twinning shear was ~0.65, the twinning growth and detwinning were shear-dominated processes mediated by twinning dislocations on the twinning plane. However, the dominant twinning dislocations were not ($\boldsymbol{b}_1$, h_1) twinning dislocations (as predicted by the classical twinning theories) but ($\boldsymbol{b}_{1/2}$, $h_{1/2}$) twinning dislocations. Twinning dislocations with much larger step heights were also observed occasionally, but showed much lower overall

mobility comparing with ($\boldsymbol{b}_{1/2}$, $h_{1/2}$). Moreover, direct evidence for atomic shuffles involving in the twinning process was discovered, indicating that alternative basal planes shuffled ~1/6<-1 1 0 0> during the twinning and {1 1 -2 1} twin boundary had no mirror symmetry. These findings uncovered an unambiguous atomic-scale picture of the {1 1 -2 1} twinning process and provided direct experimental evidences to the classical twinning theories and recent simulations.

{1 1 -2 2} tension twinning in HCP crystals was unprecedentedly discovered by using in situ TEM. The results unambiguously showed that, dramatically different from the conventional idea, the {1 1 -2 2} twinning could be a tension twinning with (0 0 0 1) K_2 plane. Thereby, the twinning showed extremely large twinning shear (~1.1) and was dominated by elementary twinning dislocations. The choice of the basal plane rather than the {1 1 -2 -6} plane as the K_2 implied that "simple shuffles" rather than "small twinning shear" may be the dominate factor for twinning in HCP nanocrystals. In this new twinning mode, the basal <$\boldsymbol{a}$> dislocation could penetrate the {1 1 -2 2} twin boundary, slip on the basal plane in the twin, and meanwhile assist the twinning growth. Additionally, the tension twin nature of the observed {1 1 -2 2} twinning enabled a synergy of {1 1 -2 1} twinning and {1 1 -2 2} twinning, forming a unique three-fold twinning structure which was mobile via a cooperative motion of twinning dislocations on the {1 1 -2 1} and {1 1 -2 2} twinning planes.

Finally, it should be noted that, in early days, the study on deformation twinning was limited by insufficient clear microscopic evidences; and hence assumptions had to be made to stringently describe and interpret these transformations. With the advancement of high resolution microscopy, more and more clear evidences were obtained that confront the classical expectations. To unravel the controversies between classical twinning theories and ex situ experimental observations, it is highly desired to think outside of the box and rigorously verify

the new models or mechanisms. Here, by using state-of-the-art atomic-resolution in situ TEM, the transformation mechanisms associated with various twinning modes were unprecedentedly revealed. The results unambiguously established atomic mechanisms of various twinning modes, provided much-needed results that resolved long-standing confusions and controversies in the twinning behaviors of HCP metals, and most importantly, demonstrated a paradigm-shifting view that mechanisms of twinning were essentially interfacial processes conforming to the lattice correspondence and were not necessarily confined to a single twinning plane.

9.0 OUTLOOK

9.1 ON THE APPLCATIONS OF THE FINDINGS

First, the atomic mechanisms in this dissertation can provide physics-based strategic guidance to the twinning/phase-transformation-based alloy design and processing. Following examples demonstrate the possible applications of the findings along this line. Since {1 0 -1 2} twinning can grow extensively at low stress-state and mediate early stage of deformation in HCP metals[92,98], it is necessary to suppress the {1 0 -1 2} twinning nucleation and growth in order to increase the strength of HCP metals. Referring to the mechanisms of {1 0 -1 2} twinning nucleation and growth, an effective way is increasing the energy (or decreasing the stability) of B│P-type interfaces by e.g. alloying; thereby, the twin boundary energy of the twin (and embryo) will increase, providing a higher barrier for twinning nucleation as well as a higher thermodynamic driving force for the B│P-type interfaces converting to CTB; and hence classical twinning dislocation mechanism has to work and interact with traditional hardening elements (e.g. precipitates and matrix dislocations). Another way to suppress the {1 0 -1 2} twinning can be pinning the CTB by sequential alloying, pre-deformation and annealing. According to our findings, through pre-deformation and unloading, the B│P-type twin boundary will firstly be activated and then convert to CTB; subsequent annealing will allow the alloying elements to diffuse and segregate on the composite CTB and at the core of twinning dislocations on the CTB;

in principle, the segregation of alloying elements on the CTB can increase the kinetic barrier for further twinning growth. Thereafter, further deformation will have to rely on nucleation of new {1 0 -1 2} twins which require higher stress since the easy nucleation sites have been consumed in the pre-deformation. Impressively, this strategy has been validated by a recent study[13], though the fundamental reason was not fully understood or elaborated in that paper. As shown in Chapter 5, FCC phase can assist the deformation of HCP metal in several ways, e.g. assisting reversible deformation, {1 0 -1 2} twinning, and grain rotation. In addition, the FCC regions themselves can supply profuse dislocation modes; especially, in the newly discovered transformation mechanisms, the hard HCP-<***c***> direction on prismatic plane is transformed to the soft FCC-<1 1 -2> direction on {1 1 1} plane, or the hard HCP-<1 2 -3 1> direction on {-1 1 0 1} plane to FCC-<1 1 -2> direction on {1 1 1} plane, meaning that the these HCP→FCC transformation mechanisms can facilitate deformation along hard directions of the original HCP grain and hence increase its ductility. In addition, the FCC│HCP interface can be a barrier for dislocations and hence contribute to hardening of the material. As such, prompting the HCP→FCC transformations and achieving a "dynamic dual phase structure" may lead to a combined increase of strength and ductility, as hinted by a recent study on dual-phase high-entropy alloys starting from FCC[7].

Secondly, the findings point to interesting and promising directions for future researches, e.g., exploring new mechanisms of HCP→FCC phase transformation, shear-shuffle competition and shuffle-dominated mechanisms in low-shear twinning modes in other double-lattice or multiple-lattice crystal structures, effect of surface doping/adsorbent on twinning nucleation, and sample size-effect on twinning elements. In addition, the atomic-resolution findings can be

directly compared with computer simulations, to validate the simulations methods for better computational study on issues that currently beyond the capability of in situ TEM.

It should be noted that the results in this dissertation were obtained from nanosized samples; and hence the validity of the conclusions can be questioned when extending them to bulk HCP metals. Yet, considering the great answerability of the findings to previous ex situ and macroscopic findings, it is fairly reasonable to expect the same mechanistic pictures in bulk HCP metals. In classical theories of twinning and martensitic transformation, the minimum shear strain is favorable in that the strain accommodations required for the deformation in confined volume is kept to the minimum. By contrast, in nanosized samples, the volume confinement is considerably released by the free surface and hence the "minimum shear assumption" may become unnecessarily stringent when it conflicts with the requirement of "simple atomic shuffles". As such, the "size effect" on the twinning elements may warrant further study. On the other hand, the nanosized samples are very suitable for the in situ TEM study on transformation mechanisms in materials. The nanosized dimension makes the sample transparent to the electron beam in TEM and enables the study to be carried out at atomic resolution. In addition, nanosized sample can be easily made defect-free, offering a clean system for the study without the complication from other defects. Moreover, the high strain tolerance and defect-scarce state of nanosized samples make it possible to obtain high stress state in nanocrystals[31,33,35,161]; and hence interfacial processes, which required high activation stresses and were hardly achievable in bulk samples, could be activated in nanocrystals[26,28,173]. Thereby, nanocrystal shows more flexible transformation pathways than its bulk counterpart, and hence is a better choice for the study of transformation mechanisms. To reveal more evidences to the shear and shuffle competition (see

Chapter 4 and 7), similar in situ TEM studies on other double-lattice and multiple-lattice crystal structures using nanosized samples are highly desired.

9.2 ON THE FUTURE OF IN SITU TEM FOR MECHANICAL BEHAVIORS OF MATERIALS

So far, researches on mechanical behaviors of materials using in situ TEM, including this study, are limited by several drawbacks. First, the test environments (e.g. high vacuum, room temperature, single stimulus) are more or less different from the practical working conditions of the materials. As a result, there are always concerns regarding the validity of the findings to materials in real application. Future in situ TEM technologies for mechanical studies should be able to mimic the real working condition of the materials, by heating/cooling/biasing the sample and establishing desired gas environment for the in situ mechanical experiments. These can be realized by modifying the TEM holder or the TEM; and thanks to the development of environmental TEM (ETEM) technology, some achievements have been made[174,175].

Second, the temporal resolution of the TEM is still low, making it hard to capture fast transformations such as nucleation process of the martensite. In addition, the electron beam sometimes has significant impact on the experiment, e.g. by heating, sputtering and decomposing the sample. The dynamic TEM is not readily applicable in mechanical studies[176,177]. The high speed cameras seems to be the best solution so far to capture the fast transformations and to reduce the beam effects by enabling low does imaging[178].

Third, it has been difficult to carry out atomic-resolution operando study whilst accurately recording the stress-strain curve; and hence the stress-strain responses cannot be

unambiguously linked to the atomic-scale microstructural changes. The problem mainly lies in the mechanical stability of the mechanisms used for detecting the stress and strain.

Fourth, advanced sample preparation and crystal manipulation techniques are always needed for high resolution in situ investigation, especially in studying the dynamic interactions between two crystals surfaces (e.g. friction and wear process[179]) wherein mutual orientation of the two crystals must be controlled. Our recent publication[174] demonstrated advanced crystal manipulation techniques on the basis of ETEM-AFM setup that unprecedentedly realized controlled contact between two crystal surfaces (including orientations of both crystals and mutual orientation) and enabled study on the dependence of interaction forces on mutual orientations and the water vapor pressure in the environment. Automatic apparatus for enabling similar crystal manipulations are under development in several institutions.

In sum, the challenges in in situ TEM study on mechanical behaviors of materials have been listed. Possible solutions and future research directions are discussed.

BIBLIOGRAPHY

1 Wu, Z. & Curtin, W. A. The origins of high hardening and low ductility in magnesium. *Nature* **526**, 62-67 (2015).

2 Curtin, W. A., Sandlobes, S., Yin, B., Ahmad, R. & Wu, Z. Mechanistic origin and prediction of enhanced ductility in magnesium alloys. *Science* **359**, 447-452 (2018).

3 Zhou, N., Zhang, Z., Jin, L., Dong, J., Chen, B. & Ding, W. Ductility improvement by twinning and twin–slip interaction in a Mg-Y alloy. *Mater. Des.* **56**, 966-974 (2014).

4 Valiev, R. Z., Alexandrov, I. V., Zhu, Y. T. & Lowe, T. C. Paradox of strength and ductility in metals processed by severe plastic deformation. *J. Mater. Res.* **17**, 5-8 (2011).

5 Lu, L., Chen, X., Huang, X. & Lu, K. Revealing the maximum strength in nanotwinned copper. *Science* **323**, 607-610 (2009).

6 Wang, L., Lu, Y., Kong, D., Xiao, L., Sha, X., Sun, J., Zhang, Z. & Han, X. Dynamic and atomic-scale understanding of the twin thickness effect on dislocation nucleation and propagation activities by in situ bending of Ni nanowires. *Acta Mater.* **90**, 194-203 (2015).

7 Li, Z., Pradeep, K. G., Deng, Y., Raabe, D. & Tasan, C. C. Metastable high-entropy dual-phase alloys overcome the strength-ductility trade-off. *Nature* **534**, 227-230 (2016).

8 Wang, Y., Chen, M., Zhou, F. & Ma, E. High tensile ductility in a nanostructured metal. *Nature* **419**, 912-915 (2002).

9 Wei, Y., Li, Y., Zhu, L., Liu, Y., Lei, X., Wang, G., Wu, Y., Mi, Z., Liu, J., Wang, H. & Gao, H. Evading the strength-ductility trade-off dilemma in steel through gradient hierarchical nanotwins. *Nat. Commun.* **5**, 3580 (2014).

10 Fu, H., Ge, B., Xin, Y., Wu, R., Fernandez, C., Huang, J. & Peng, Q. Achieving high strength and ductility in magnesium alloys via densely hierarchical double contraction nanotwins. *Nano Lett.* **17**, 6117-6124 (2017).

11 Zhao, Y. H., Zhu, Y. T., Liao, X. Z., Horita, Z. & Langdon, T. G. Tailoring stacking fault energy for high ductility and high strength in ultrafine grained Cu and its alloy. *Appl. Phys. Lett.* **89**, 121906 (2006).

12 Zhang, Z., Sheng, H., Wang, Z., Gludovatz, B., George, E. P., Yu, Q., Mao, S. X. & Ritchie, R. O. Dislocation mechanisms and 3D twin architectures generate exceptional strength-ductility-toughness combination in CrCoNi medium-entropy alloy. *Nat. Commun.* **8**, 14390 (2017).

13 Nie, J. F., Zhu, Y. M., Liu, J. Z. & Fang, X. Y. Periodic segregation of solute atoms in fully coherent twin boundaries. *Science* **340**, 957-960 (2013).

14 Jang, D., Li, X., Gao, H. & Greer, J. R. Deformation mechanisms in nanotwinned metal nanopillars. *Nat. Nanotechnol.* **7**, 594-601 (2012).

15 Zepeda-Ruiz, L. A., Stukowski, A., Oppelstrup, T. & Bulatov, V. V. Probing the limits of metal plasticity with molecular dynamics simulations. *Nature* **550**, 492-495 (2017).

16 Chen, M., Ma, E., Hemker, K. J., Sheng, H., Wang, Y. & Cheng, X. Deformation twinning in nanocrystalline aluminum. *Science* **300**, 1275-1277 (2003).

17 Pan, Q., Zhou, H., Lu, Q., Gao, H. & Lu, L. History-independent cyclic response of nanotwinned metals. *Nature* **551**, 214-217 (2017).

18 Bilby, B. A. & Crocker, A. G. The theory of the crystallography of deformation twinning. *Proc. Royal Soc. A* **288**, 240-255 (1965).

19 Christian, J. W. & Mahajan, S. Deformation Twinning. *Prog. Mater. Sci.* **39**, 1-157 (1995).

20 El Kadiri, H. & Oppedal, A. L. A crystal plasticity theory for latent hardening by glide twinning through dislocation transmutation and twin accommodation effects. *J. Mech. Phys. Solids* **58**, 613-624 (2010).

21 Agnew, S. R. & Duygulu, Ö. Plastic anisotropy and the role of non-basal slip in magnesium alloy AZ31B. *Inter. J. Plasticity* **21**, 1161-1193 (2005).

22 Lentz, M., Risse, M., Schaefer, N., Reimers, W. & Beyerlein, I. J. Strength and ductility with {1011} - {1012} double twinning in a magnesium alloy. *Nat. Commun.* **7**, 11068 (2016).

23 Oppedal, A. L., El Kadiri, H., Tomé, C. N., Kaschner, G. C., Vogel, S. C., Baird, J. C. & Horstemeyer, M. F. Effect of dislocation transmutation on modeling hardening mechanisms by twinning in magnesium. *Inter. J. Plasticity* **30-31**, 41-61 (2012).

24 Wang, F. & Agnew, S. R. Dislocation transmutation by tension twinning in magnesium alloy AZ31. *Inter. J. Plasticity* **81**, 63-86 (2016).

25 Clapp, P. C. Rain dances, microstructure and transformations. *J. Phys. IV France* **04**, C3-3-C3-11 (1994).

26 Wang, J., Zeng, Z., Weinberger, C. R., Zhang, Z., Zhu, T. & Mao, S. X. In situ atomic-scale observation of twinning-dominated deformation in nanoscale body-centred cubic tungsten. *Nat. Mater.* **14**, 594-600 (2015).

27 He, Y., Zhong, L., Fan, F., Wang, C., Zhu, T. & Mao, S. X. In situ observation of shear-driven amorphization in silicon crystals. *Nat. Nanotechnol.* **11**, 866-871 (2016).

28 Zheng, H., Cao, A., Weinberger, C. R., Huang, J., Du, K., Wang, J., Ma, Y., Xia, Y. & Mao, S. X. Discrete plasticity in sub-10-nm-sized gold crystals. *Nat. Commun.* **1**, 144 (2010).

29 Zhong, L., Sansoz, F., He, Y., Wang, C., Zhang, Z. & Mao, S. X. Slip-activated surface creep with room-temperature super-elongation in metallic nanocrystals. *Nat. Mater.* **16**, 439-445 (2017).

30 Wang, S. J., Wang, H., Du, K., Zhang, W., Sui, M. L. & Mao, S. X. Deformation-induced structural transition in body-centred cubic molybdenum. *Nat. Commun.* **5**, 3433 (2014).

31 Shan, Z. W., Mishra, R. K., Syed Asif, S. A., Warren, O. L. & Minor, A. M. Mechanical annealing and source-limited deformation in submicrometre-diameter Ni crystals. *Nat. Mater.* **7**, 115-119 (2008).

32 Chisholm, C., Bei, H., Lowry, M. B., Oh, J., Syed Asif, S. A., Warren, O. L., Shan, Z. W., George, E. P. & Minor, A. M. Dislocation starvation and exhaustion hardening in Mo alloy nanofibers. *Acta Mater.* **60**, 2258-2264 (2012).

33 Uchic, M. D., Dimiduk, D. M., Florando, J. N. & Nix, W. D. Sample dimensions influence strength and crystal plasticity. *Science* **305**, 986-989 (2004).

34 Suresh, S. & Ju, L. Deformation of the ultra-strong. *Nature* **456**, 716-717 (2008).

35 Wang, L., Liu, P., Guan, P., Yang, M., Sun, J., Cheng, Y., Hirata, A., Zhang, Z., Ma, E., Chen, M. & Han, X. In situ atomic-scale observation of continuous and reversible lattice deformation beyond the elastic limit. *Nat. Commun.* **4**, 2413 (2013).

36 Yu, Q., Qi, L., Mishra, R. K., Li, J. & Minor, A. M. Reducing deformation anisotropy to achieve ultrahigh strength and ductility in Mg at the nanoscale. *PNAS* **110**, 13289-13293 (2013).

37 Shan, Z., Stach, E. A., Wiezorek, J. M. K., Knapp, J. A., Follstaedt, D. M. & Mao, S. X. Grian boundary-mediated plasticity in nanocrystalline nickel. *Science* **305**, 654-658 (2004).

38 Minor, A. M., Lilleodden, E. T., Jin, M., Stach, E. A., Chrzan, D. C. & Morris, J. W. Room temperature dislocation plasticity in silicon. *Philo. Mag.* **85**, 323-330 (2005).

39 Sun, J., He, L., Lo, Y. C., Xu, T., Bi, H., Sun, L., Zhang, Z., Mao, S. X. & Li, J. Liquid-like pseudoelasticity of sub-10-nm crystalline silver particles. *Nat. Mater.* **13**, 1007-1012 (2014).

40 Wang, L., Han, X., Liu, P., Yue, Y., Zhang, Z. & Ma, E. In situ observation of dislocation behavior in nanometer grains. *Phys. Rev. Lett.* **105**, 135501 (2010).

41 Yu, Q., Shan, Z. W., Li, J., Huang, X., Xiao, L., Sun, J. & Ma, E. Strong crystal size effect on deformation twinning. *Nature* **463**, 335-338 (2010).

42 Yu, Q., Mishra, R. K. & Minor, A. M. The effect of size on the deformation twinning behavior in hexagonal close-packed Ti and Mg. *JOM* **64**, 1235-1240 (2012).

43 Liu, B. Y., Wang, J., Li, B., Lu, L., Zhang, X. Y., Shan, Z. W., Li, J., Jia, C. L., Sun, J. & Ma, E. Twinning-like lattice reorientation without a crystallographic twinning plane. *Nat. Commun.* **5**, 3297 (2014).

44 Liu, B.-Y., Wan, L., Wang, J., Ma, E. & Shan, Z.-W. Terrace-like morphology of the boundary created through basal-prismatic transformation in magnesium. *Scripta Mater.* **100**, 86-89 (2015).

45 Yu, Q., Qi, L., Tsuru, T., Traylor, R., Rugg, D., Morris, J. W., Asta, M., Chrzan, D. C. & Minor, A. M. Origin of dramatic oxygen solute strengthening effect in titanium. *Science* **347**, 635-639 (2015).

46 Yu, Q., Qi, L., Chen, K., Mishra, R. K., Li, J. & Minor, A. M. The nanostructured origin of deformation twinning. *Nano Lett.* **12**, 887-892 (2012).

47 Morrow, B. M., Cerreta, E. K., McCabe, R. J. & Tomé, C. N. Transmission electron microscope in situ straining technique to directly observe defects and interfaces during deformation in magnesium. *JOM* **67**, 1721-1728 (2015).

48 Jungjohann, K. & Carter, C. B. in *Transmission Electron Microscopy: Diffraction, Imaging, and Spectroscopy* (eds C. B. Carter & D.B. Williams) Ch. 2, 17-80 (Springer, 2016).

49 Bevis, M. & Crocker, A. G. Twinning shears in lattices. *Proc. Royal Soc. A: Mathematical and Physical Science* **304**, 123-134 (1968).

50 Hirth, J. P., Wang, J. & Tomé, C. N. Disconnections and other defects associated with twin interfaces. *Prog. Mater. Sci.* **83**, 417-471 (2016).

51 Khater, H. A., Serra, A. & Pond, R. C. Atomic shearing and shuffling accompanying the motion of twinning disconnections in zirconium. *Philos. Mag.* **93**, 1279-1298 (2013).

52 Beyerlein, I. J., Zhang, X. & Misra, A. Growth twins and deformation twins in metals. *Annu. Rev. Mater. Res.* **44**, 329-363 (2014).

53 Zhu, Y. T., Liao, X. Z. & Wu, X. L. Deformation twinning in nanocrystalline materials. *Prog. Mater. Sci.* **57**, 1-62 (2012).

54 Liao, X., Wang, J., Nie, J., Jiang, Y. & Wu, P. Deformation twinning in hexagonal materials. *MRS Bulletin* **41**, 314-319 (2016).

55 Wang, Y. B., Sui, M. L. & Ma, E. In situobservation of twin boundary migration in copper with nanoscale twins during tensile deformation. *Philos. Mag. Lett.* **87**, 935-942 (2007).

56 Yoo, M. H. Slip, twinning, and fracture in hexagonal close-packed metals. *Met. Trans. A* **12A**, 409-418 (1981).

57 Xu, F., Zhang, X. Y., Ni, H. & Liu, Q. {11-24} deformation twinning in pure Ti during dynamic plastic deformation. *Mater. Sci. Eng. A* **541**, 190-195 (2012).

58 El Kadiri, H., Barrett, C. D., Wang, J. & Tomé, C. N. Why are {10-12} twins profuse in magnesium? *Acta Mater.* **85**, 354-361 (2015).

59 Serra, A., Bacon, D. J. & Pond, R. C. A comment on B. Li, H. El Kadiri and M.F. Horstemeyer 'Extended zonal dislocations mediating twinning in titanium'. *Philos. Mag.* **93**, 3495-3503 (2013).

60 Li, B. Shear and shuffle in {11-22}<11-2-3> twinning in titanium. *J. Mater. Res.* **30**, 3795-3802 (2015).

61 El Kadiri, H. & Barrett, C. D. Comments on "extended zonal dislocations mediating twinning in titanium". *Philos. Mag.* **93**, 3491-3494 (2013).

62 Serra, A., Bacon, D. J. & Pond, R. C. The crystallography and core structure of twinning dislocations in H.C.P. metals. *Acta Metall.* **36**, 3183-3203 (1988).

63 Serra, A., Pond, R. C. & Bacon, D. J. Computer simulation of the structure and mobility of twinning disclocations in H.C.P. Metals. *Acta Metall. Mater.* **39**, 1469-1480 (1991).

64 Serra, A. & Bacon, D. J. Modelling the motion of {1 1 -2 2} twinning dislocations in the HCP metals. *Mater. Sci. Eng. A* **400-401**, 496-498 (2005).

65 Li, B., El Kadiri, H. & Horstemeyer, M. F. Extended zonal dislocations mediating twinning in titanium. *Philos. Mag.* **92**, 1006-1022 (2012).

66 Li, B. Reply to the two Comments, by A. Serra, D. J. Bacon and R. C. Pond, and by H. El Kadiri and C. Barrett on B. Li, H. El Kadiri and M.F. Horstemeyer "Extended zonal dislocations mediating twinning in titanium". *Philo. Mag.* **93**, 3504-3510 (2013).

67 Serra, A., Bacon, D. J. & Pond, R. C. Rejoinder to the response by B. Li on our Comment on the paper B. Li, H. El Kadiri and M.F. Horstemeyer 'Extended zonal dislocations mediating twinning in titanium'. *Philos. Mag.* **93**, 3511-3514 (2013).

68 Rapperport, E. J. Room temperature deformation process in zirconium. *Acta Mater.* **7**, 254-260 (1959).

69 Backofen, W. A. & Paton, N. E. Plastic deformation of titanium at elevated temperatures. *Metall. Trans. A* **1**, 2839-2847 (1970).

70 Pond, R. C., Hirth, J. P., Serra, A. & Bacon, D. J. Atomic displacements accompanying deformation twinning: shears and shuffles. *Mater. Res. Lett.* **4**, 185-190 (2016).

71 Kronberg, M. L. Atomic movements and dislocation structures for plastic slip in single crystals of b-uranium. *J. Nucl. Mater.* **1**, 85-95 (1959).

72 Westlake, D. G. Twinning in zirconium. *Acta Metall.* **9**, 327-331 (1961).

73 Christian, J. W. & Crocker, A. G. *Dislocations in Solids*. Vol. 3 (North-Holland Publ. Co., 1980).

74 Hirth, J. P. & Pond, R. C. Steps, dislocations and disconnections as interface defects relating to structure and phase transformations. *Acta Mater.* **44**, 4749-4763 (1996).

75 Kim, I., Kim, J., Shin, D. H., Liao, X. Z. & Zhu, Y. T. Deformation twins in pure titanium processed by equal channel angular pressing. *Scripta Mater.* **48**, 813-817 (2003).

76 Pond, R. C., Bacon, D. J. & Serra, A. Interfacial structure of {10-11} twins and twinning dislocations in titanium. *Philos. Mag. Lett.* **71**, 275-284 (1995).

77 Braisaz, T., Ruterana, P., Nouet, G. & Pond, R. C. Investigation of {1012} twins in Zn using high-resolution electron microscopy: Interfacial defects and interactions. *Philos. Mag. A* **75**, 1075-1095 (1997).

78 Braisaz, T., Puterana, P., Nouet, G., Serra, A., Komninou, P., Kehagias, T. & Karakostas, T. High-resolution electron microscopy study of the (1012) twin and defects analysis in deformed polycrystalline alpha titanium. *Philos. Mag. Lett.* **74**, 331-338 (1996).

79 Ghazisaeidi, M. & Curtin, W. A. Analysis of dissociation of <c> and <c+a> dislocations to nucleate (10-12) twins in Mg. *Modell. Simul. Mater. Sci. Eng.* **21**, 055007 (2013).

80 Serra, A. & Bacon, D. J. A new model for {10-12} twin growth in hcp metals. *Philos. Mag. A* **73**, 333-343 (1996).

81 Serra, A., Bacon, D. J. & Pond, R. C. Dislocations in Interfaces in the H.C.P. Metal- I. Defects Formed by Absorption of Crystal Dislocations. *Acta Mater.* **47**, 1425-1439 (1999).

82 Pond, R. C. & Celotto, S. Interfacial deformation mechanisms in hexagonal-close-packed metals. *Metall. Mater. Trans. A* **33**, 801-807 (2002).

83 Ostapovets, A. & Gröger, R. Twinning disconnections and basal–prismatic twin boundary in magnesium. *Modell. Simul. Mater. Sci. Eng.* **22**, 025015 (2014).

84 Wang, J., Liu, L., Tomé, C. N., Mao, S. X. & Gong, S. K. Twinning and de-twinning via glide and climb of twinning dislocations along serrated coherent twin boundaries in hexagonal-close-packed metals. *Mater. Res. Lett.* **1**, 81-88 (2013).

85 Barrett, C. D. & El Kadiri, H. The roles of grain boundary dislocations and disclinations in the nucleation of {10-12} twinning. *Acta Mater.* **63**, 1-15 (2014).

86 Tu, J., Zhang, X. Y., Lou, C. & Liu, Q. HREM investigation of twin boundary and interface defects in deformed polycrystalline cobalt. *Philos. Mag. Lett.* **93**, 292-298 (2013).

87 Godet, S., Jiang, L., Luo, A. A. & Jonas, J. J. Use of schmid factors to select extension twin variants in extruded magnesium alloy tubes. *Scripta Mater.* **55**, 1055-1058 (2006).

88 Tu, J. & Zhang, S. On the {10-12} twinning growth mechanism in hexagonal close-packed metals. *Mater. Des.* **96**, 143-149 (2016).

89 Zhang, X. Y., Li, B., Tu, J., Sun, Q. & Liu, Q. Non-classical twinning behavior in dynamically deformed cobalt. *Mater. Res. Lett.* **3**, 142-148 (2015).

90 Capolungo, L., Marshall, P. E., McCabe, R. J., Beyerlein, I. J. & Tomé, C. N. Nucleation and growth of twins in Zr: A statistical study. *Acta Mater.* **57**, 6047-6056 (2009).

91 Beyerlein, I. J., Capolungo, L., Marshall, P. E., McCabe, R. J. & Tomé, C. N. Statistical analyses of deformation twinning in magnesium. *Philos. Mag.* **90**, 2161-2190 (2010).

92 Barrett, C. D., El Kadiri, H. & Tschopp, M. A. Breakdown of the Schmid law in homogeneous and heterogeneous nucleation events of slip and twinning in magnesium. *J. Mech. Phys. Solids* **60**, 2084-2099 (2012).

93 Braisaz, T., Ruterana, P. & Nouet, G. Twin tip defects related to the nucleation and growth mechanisms of the twin (1012) in zinc characterized by high-resolution electron microscopy. *Philos. Mag. A* **76**, 63-84 (1997).

94 Barnett, M. R., Keshavarz, Z., Beer, A. G. & Ma, X. Non-Schmid behaviour during secondary twinning in a polycrystalline magnesium alloy. *Acta Mater.* **56**, 5-15 (2008).

95 Lainé, S. J. & Knowles, K. M. {11-24} deformation twinning in commercial purity titanium at room temperature. *Philos. Mag.* **95**, 2153-2166 (2015).

96 Tu, J., Zhang, X. Y., Ren, Y., Sun, Q. & Liu, Q. Structural characterization of {10-12} irregular-shaped twinning boundary in hexagonal close-packed metals. *Mater. Charact.* **106**, 240-244 (2015).

97 Yu, Q., Jiang, Y. & Wang, J. Cyclic deformation and fatigue damage in single-crystal magnesium under fully reversed strain-controlled tension–compression in the [10-10] direction. *Scripta Mater.* **96**, 41-44 (2015).

98 Yu, Q., Zhang, J. & Jiang, Y. Direct observation of twinning–detwinning–retwinning on magnesium single crystal subjected to strain-controlled cyclic tension–compression in [0001] direction. *Philos. Mag. Lett.* **91**, 757-765 (2011).

99 Ostapovets, A. & Serra, A. Characterization of the matrix twin interface of a (10-12) twin during growth. *Philos. Mag.* **94**, 2827-2839 (2014).

100 Wang, J., Yadav, S. K., Hirth, J. P., Tomé, C. N. & Beyerlein, I. J. Pure-shuffle nucleation of deformation twins in hexagonal-close-packed metals. *Mater. Res. Lett.* **1**, 126-132 (2013).

101 Li, B. & Ma, E. Atomic shuffling dominated mechanism for deformation twinning in magnesium. *Phys. Rev. Lett.* **103**, 035503 (2009).

102 Serra, A., Bacon, D. J. & Pond, R. C. Comment on "Atomic Shuffling Dominated Mechanism For Deformation Twinning In Magnesium". *Phys. Rev. Lett.* **104**, 029603 (2010).

103 Barrett, C. D. & El Kadiri, H. Impact of deformation faceting on {10-12}, {10-11} and {10-13} embryonic twin nucleation in hexagonal close-packed metals. *Acta Mater.* **70**, 137-161 (2014).

104 Li, B. & Ma, E. Li and Ma Reply. *Phys. Rev. Lett.* **104**, 029604 (2010).

105 Christian, J. W. *The theory of transformations in metals and alloys*. (Pergamon, 2002).

106 Le Lann, A. & Dubertret, A. A develpment of kronberg's model for {10-12} twins in H.C.P. metals and extension to {11-22} twins. *Phys. Stat. Sol. (a)* **51**, 497-507 (1979).

107 Niewczas, M. Lattice correspondence during twinning in hexagonal close-packed crystals. *Acta Mater.* **58**, 5848-5857 (2010).

108 Ostapovets, A. & Molnár, P. On the relationship between the "shuffling-dominated" and "shear-dominated" mechanisms for twinning in magnesium. *Scripta Mater.* **69**, 287-290 (2013).

109 Li, B. & Zhang, X. Y. Twinning with zero twinning shear. *Scripta Mater.* **125**, 73-79 (2016).

110 Sun, Q., Zhang, X. Y., Tu, J., Ren, Y., Qin, H. & Liu, Q. Characterization of basal-prismatic interface of twin in deformed titanium by high-resolution transmission electron microscopy. *Philos. Mag. Lett.* **95**, 145-151 (2015).

111 Minonishi, Y., Ishioka, S., Koiwa, M. & Morozumi, S. The structure of {11-21} twin boundaries in H.C.P. Crystals. *Phys. Stat. Sol. (a)* **71**, 253-258 (1982).

112 Thompson, N. & Millard, D. J. Twin formation in cadmium. *Philos. Mag.* **43**, 422-440 (1952).

113 Mendelson, S. Dislocation dissociations in hcp metals. *J. Appl. Phys.* **41**, 1893-1910 (1970).

114 Wang, J., Hirth, J. P. & Tomé, C. N. (10-12) Twinning nucleation mechanisms in hexagonal-close-packed crystals. *Acta Mater.* **57**, 5521-5530 (2009).

115 Luque, A., Ghazisaeidi, M. & Curtin, W. A. Deformation modes in magnesium (0001) and (01-11) single crystals: simulations versus experiments. *Modell. Simul. Mater. Sci. Eng.* **21**, 045010 (2013).

116 Wu, L., Jain, A., Brown, D. W., Stoica, G. M., Agnew, S. R., Clausen, B., Fielden, D. E. & Liaw, P. K. Twinning–detwinning behavior during the strain-controlled low-cycle fatigue testing of a wrought magnesium alloy, ZK60A. *Acta Mater.* **56**, 688-695 (2008).

117 Cáceres, C. H., Sumitomo, T. & Veidt, M. Pseudoelastic behaviour of cast magnesium AZ91 alloy under cyclic loading–unloading. *Acta Mater.* **51**, 6211-6218 (2003).

118 Wu, L., Agnew, S. R., Brown, D. W., Stoica, G. M., Clausen, B., Jain, A., Fielden, D. E. & Liaw, P. K. Internal stress relaxation and load redistribution during the twinning–detwinning-dominated cyclic deformation of a wrought magnesium alloy, ZK60A. *Acta Mater.* **56**, 3699-3707 (2008).

119 Egerton, R. F., Li, P. & Malac, M. Radiation damage in the TEM and SEM. *Micron* **35**, 399-409 (2004).

120 Mompiou, F., Legros, M. & Lartigue-Korinek, S. Deformation mechanisms in submicron Be wires. *J. Mater. Res.* **32**, 4616-4625 (2017).

121 Bei, H., Shim, S., Miller, M. K., Pharr, G. M. & George, E. P. Effect of focused ion beam milling on the nanomechanical behavior of a molybdenum-alloy single crystal. *Appl. Phys. Lett.* **91**, 111915 (2007).

122 Greer, J. R., Espinosa, H., Ramesh, K. T. & Nadgorny, E. Comment on "Effects of focused ion beam milling on the nanomechanical behavior of a molybdenum-alloy single crystal" Appl. Phys. Lett. 91, 111915 (2007). *Appl. Phys. Lett.* **92**, 096101 (2008).

123 Kacher, J. & Minor, A. M. Twin boundary interactions with grain boundaries investigated in pure rhenium. *Acta Mater.* **81**, 1-8 (2014).

124 Jeffery, R. A. & Smith, E. Work-hardening and ductility of rhenium and their relation to the behaviours of other metals having a hexagonal structure. *Nature* **187**, 52-53 (1960).

125 de Jong, M., Kacher, J., Sluiter, M. H., Qi, L., Olmsted, D. L., van de Walle, A., Morris, J. W., Minor, A. M. & Asta, M. Electronic Origins of Anomalous Twin Boundary Energies in Hexagonal Close Packed Transition Metals. *Phys. Rev. Lett.* **115**, 065501 (2015).

126 Steinle-Neumann, G., Stixrude, L. & Cohen, R. E. First-principle elastic constants for the hcp transition metals Fe, Co, and Re at high pressure. *Phys. Rev. B* **60**, 791-800 (1999).

127 Carlen, J. C. & Bryskin, B. D. Rhenium - A unique rare metal. *Mater. Manuf. Processes* **9**, 1087-1104 (1994).

128 Sherman, A. J., Fortini, A. J., Williams, B. E. & Tuffias, R. in *International Symposium on Rhenium and Rhenium Alloys* (ed B.D. Bryskin) (TMS, 1997).

129 Sims, C. T., Craighead, C. M. & Jaffee, R. I. Physical and mechanical properties of rhenium. *JOM* **7**, 168-179 (1955).

130 Jeffery, R. A. & Smith, E. Deformation twinning in rhenium single crystals. *Philos. Mag.* **13**, 1163-1168 (1966).

131 He, Y., Gu, M., Xiao, h., Luo, L., Shao, Y., Gao, F., Du, Y., Mao, S. X. & Wang, C. Atomistic conversion reaction mechanism of WO_3 in secondary ion batteries of Li, Na and Ca. *Angew. Chem. Int. Ed.* **55**, 6244-6247 (2016).

132 Nelson, C. T., Gao, P., Jokisaari, J. R., Heikes, C., Adamo, C., Melville, A., Baek, S. H., Folkman, C. M., Winchester, B., Gu, Y., Liu, Y., Zhang, K., Wang, E., Li, J., Chen, L. Q., Eom, C. B., Schlom, D. G. & Pan, X. Domain dynamics during ferroelectric switching. *Science* **334**, 968-971 (2011).

133 Oh, S. H., Chisholm, M. F., Kauffmann, Y. & Kaplan, W. D. Oscillatory mass transport in vapor-liquid-solid growth of sapphire nanowires. *Science* **330**, 489-493 (2010).

134 Yoshida, H., Kuwauchi, Y., Jinschek, J. R., Sun, K., Tanaka, S., Kohyama, M., Shimada, S., Haruta, M. & Takeda, S. Visualizing gas molecules interacting with supported nanoparticlate catalysts at reaction conditions. *Science* **335**, 317-319 (2012).

135 Williams, D. B. & Carter, C. B. *Transmission electron microscopy--A textbook for materials science*. (Springer, 2009).

136 Zhong, L., Sansoz, F., He, Y., Wang, C. M., Zhang, Z. & Mao, S. Slip-activated surface creep with room-temperature super-elongation in metallic nanocrystals. *Nat. Mater.* **16**, 439-445 (2016).

137 Wang, J. W., Narayanan, S., Huang, J. Y., Zhang, Z., Zhu, T. & Mao, S. X. Atomic-scale dynamic process of deformation-induced stacking fault tetrahedra in gold nanocrystals. *Nat. Commun.* **4**, 2340 (2013).

138 Zhong, L., Wang, J., Sheng, H., Zhang, Z. & Mao, S. X. Formation of monatomic metallic glasses through ultrafast liquid quenching. *Nature* **512**, 177-180 (2014).

139 Wang, L., Barabash, R., Bieler, T., Liu, W. & Eisenlohr, P. Study of {11-21} twinning in α-Ti by EBSD and laue microdiffraction. *Metall. Mater. Trans. A* **44**, 3664-3674 (2013).

140 Morrow, B. M., McCabe, R. J., Cerreta, E. K. & Tomé, C. N. Observations of the atomic structure of tensile and compressive twin boundaries and twin–twin interactions in zirconium. *Metall. Mater. Trans. A* **45**, 5891-5897 (2014).

141 Tu, J., Zhang, X., Wang, J., Sun, Q., Liu, Q. & Tomé, C. N. Structural characterization of {10-12} twin boundaries in cobalt. *Appl. Phys. Lett.* **103**, 051903 (2013).

142 Ishii, A., Li, J. & Ogata, S. Shuffling-controlled versus strain-controlled deformation twinning: The case for HCP Mg twin nucleation. *Inter. J. Plasticity* **82**, 32-43 (2016).

143 Hytch, M. J., Snoeck, E. & Kilaas, R. Quantitative measurement of displacement and strain fields from HRTEM micrographs. *Ultramicroscopy* **74**, 131-146 (1998).

144 Hytch, M. J. & Minor, A. M. Observing and measuring strain in nanostructures and devices with transmission electron microscopy. *MRS Bulletin* **39**, 138-146 (2014).

145 Xu, B., Capolungo, L. & Rodney, D. On the importance of prismatic/basal interfaces in the growth of twins in hexagonal close packed crystals. *Scripta Mater.* **68**, 901-904 (2013).

146 Hirth, J. P. Dislocations, steps and disconnections at interfaces. *J. Phys. Chem. Solids* **55**, 985-989 (1994).

147 Chen, L. Y., He, M., Shin, J., Richter, G. & Gianola, D. S. Measuring surface dislocation nucleation in defect-scarce nanostructures. *Nat. Mater.* **14**, 707-713 (2015).

148 Chrobak, D., Tymiak, N., Beaber, A., Ugurlu, O., Gerberich, W. W. & Nowak, R. Deconfinement leads to changes in the nanoscale plasticity of silicon. *Nat. Nanotechnol.* **6**, 480-484 (2011).

149 Li, B. & Zhang, X. Y. Global strain generated by shuffling-dominated {10-12}<10-1-1> twinning. *Scripta Mater.* **71**, 45-48 (2014).

150 Beyerlein, I. J. & Tome, C. N. A probabilistic twin nucleation model for HCP polycrystalline metals. *Proc. R. Soc. A* **466**, 2517-2544 (2010).

151 Wu, W., Liaw, P. K. & An, K. Unraveling cyclic deformation mechanisms of a rolled magnesium alloy using in situ neutron diffraction. *Acta Mater.* **85**, 343-353 (2015).

152 Christian, J. W. Lattice correspondence, atomic site correspondence and shape change in "diffusional-displacive" phase transformations. *Prog. Mater. Sci.* **42**, 101-108 (1997).

153 Clapp, P. C. How would we recognize a martensitic transformation if it bumped into us on a dark & austy night? *J. Phys. IV France* **05**, C8-11-C18-19 (1995).

154 Wu, S. Q., Ping, D. H., Yamabe-Mitarai, Y., Xiao, W. L., Yang, Y., Hu, Q. M., Li, G. P. & Yang, R. {112}<111> twinning during ω to body-centered cubic transition. *Acta Mater.* **62**, 122-128 (2014).

155 Wu, H. C., Kumar, A., Wang, J., Bi, X. F., Tome, C. N., Zhang, Z. & Mao, S. X. Rolling-induced face centered cubic titanium in hexagonal close packed titanium at room temperature. *Sci. Rep.* **6**, 24370 (2016).

156 Waitz, T. & Karnthaler, H. P. The fcc to hcp martensitic phase transformation in CoNi studied by TEM and AFM methods. *Acta Mater.* **45**, 837-842 (1997).

157 Zhao, H., Song, M., Ni, S., Shao, S., Wang, J. & Liao, X. Atomic-scale understanding of stress-induced phase transformation in cold-rolled Hf. *Acta Mater.* **131**, 271-279 (2017).

158 Hong, D. H., Lee, T. W., Lim, S. H., Kim, W. Y. & Hwang, S. K. Stress-induced hexagonal close-packed to face-centered cubic phase transformation in commercial-purity titanium under cryogenic plane-strain compression. *Scripta Mater.* **69**, 405-408 (2013).

159 Yang, H. & Liu, Y. Factors influencing the stress-induced fcc↔hcp martensitic transformation in Co–32Ni single crystal. *Acta Mater.* **54**, 4895-4904 (2006).

160 Liu, Y., Yang, H., Liu, Y., Jiang, B., Ding, J. & Woodward, R. Thermally induced fcc↔hcp martensitic transformation in Co–Ni. *Acta Mater.* **53**, 3625-3634 (2005).

161 Zhu, T. & Li, J. Ultra-strength materials. *Prog. Mater. Sci.* **55**, 710-757 (2010).

162 Christian, J. W. A theory of the transformation in pure cobalt. *Proc. R. Soc. A* **206**, 51-64 (1951).

163 Wan, J., Chen, S. & Hsu, T. Y. The stability of transition phases in Fe-Mn-Si based alloys. *Calphad* **25**, 355-362 (2001).

164 Pond, R. C. & Hirth, J. P. Defects at surfaces and interfaces. *Solid Stat. Phys.* **47**, 287-365 (1994).

165 Vaidya, S. & Mahajan, S. Accommondation and formation of {11-21} twins in Co single crystals. *Acta Metall.* **28**, 1123-1131 (1980).

166 Crocker, A. G. {11-21} twinning. *Philos. Mag.* **8**, 1077-1081 (1963).

167 Crocker, A. G. & Bevis, M. in *The science, technology and application of titanium* (eds R. I. Jaffee & N. E. Promisel) 453 (Pergamon press, 1970).

168 Serra, A. & Bacon, D. J. Computer simulation of twin boundaries in the h.c.p. metals. *Philos. Mag. A* **54**, 793-804 (1986).

169 Uranagase, M. & Matsumoto, R. Effects of normal stresses on the homogeneous nucleation of a basal dislocation in magnesium. *Comp. Mater. Sci.* **113**, 143-147 (2016).

170 Rapperport, E. J. & Hartley, C. S. Deformation modes of Yttrium at room temperature. *T. Metall. Soc. AIME* **215**, 1071-1072 (1959).

171 Zhu, Y. T., Liao, X. Z. & Valiev, R. Z. Formation mechanism of fivefold deformation twins in nanocrystalline face-centered-cubic metals. *Appl. Phys. Lett.* **86**, 103112 (2005).

172 Narayanan, S., Cheng, G., Zeng, Z., Zhu, Y. & Zhu, T. Strain hardening and size effect in five-fold twinned Ag nanowires. *Nano letters* **15**, 4037-4044 (2015).

173 Chen, M. W., Ma, E., Hemker, K. J., Sheng, H. W., Wang, Y. M. & Cheng, X. M. Deformation twinning in nanocrystalline aluminum. *Science* **300**, 1275-1277 (2003).

174 Zhang, X., He, Y., Sushko, M. L., Liu, J., Luo, L. L., De Yoreo, J. J., Mao, S. X., Wang, C. M. & Rosso, K. M. Direction-specific van der Waals attraction between rutile TiO_2 nanocrystals. *Science* **356**, 434-437 (2017).

175 Xie, D., Li, S., Li, M., Wang, Z., Gumbsch, P., Sun, J., Ma, E., Li, J. & Shan, Z. Hydrogenated vacancies lock dislocations in aluminium. *Nat. Commun.* **7**, 13341 (2016).

176 Browning, N. D., Bonds, M. A., Campbell, G. H., Evans, J. E., LaGrange, T., Jungjohann, K. L., Masiel, D. J., McKeown, J., Mehraeen, S., Reed, B. W. & Santala, M. Recent developments in dynamic transmission electron microscopy. *Curr. Opin. Solid State Mater. Sci.* **16**, 23-30 (2012).

177 Kim, J. S., Lagrange, T., Reed, B. W., Taheri, M. L., Armstrong, M. R., King, W. E., Browning, N. D. & Campbell, G. H. Imaging of transient structures using nanosecond in situ TEM. *Science* **321**, 1472-1475 (2008).

178 Zhu, Y., Ciston, J., Zheng, B., Miao, X., Czarnik, C., Pan, Y., Sougrat, R., Lai, Z., Hsiung, C. E., Yao, K., Pinnau, I., Pan, M. & Han, Y. Unravelling surface and interfacial structures of a metal-organic framework by transmission electron microscopy. *Nat. Mater.* **16**, 532-536 (2017).

179 Jacobs, T. D. B. & Carpick, R. W. Nanoscale wear as a stress-assisted chemical reaction. *Nat. Nanotechnol.* **8**, 108-112 (2013).